TECHNISCHE UNIVERSITÄT WIEN

Detection of aortic hemodynamics in Electrical Impedance Tomography using functional regions of interest: investigation of in-vivo, in-silico and phantom measurements.

DIPLOMARBEIT

zur Erlangung des akademischen Grades

Diplom-Ingenieur

im Rahmen des Studiums

Biomedical Engineering

eingereicht von

Martin Elenkov
Matrikelnummer 00953605

an der

Fakultät für Elektrotechnik und Informationstechnik
der Technischen Universität Wien

Betreuer:

Projektass. Dipl.-Ing. Florian Thürk

Ao.Univ.Prof. Dipl.Ing. Dr.techn. Eugenijus Kaniusas

To Alexander

"Nobody ever figures out what life is all about, and it doesn't matter. Explore the world. Nearly everything is really interesting if you go into it deeply enough."

— Richard Feynman

Abstract

Cardiovascular failure occurs in more than 20% of intensive care unit patients, which increases the risk of death by 12 fold by itself. Central hemodynamic parameters like stroke volume and blood pressure (BP), have been shown to be the best predictors for various cardiovascular diseases, but are challenging to monitor non-invasively. The current practice for their measurement requires catheterization which is associated with health complications and elevated mortality rate in patients. Other methods, although non-invasive try to approximate central hemodynamics trough peripheral measurements and are associated with additional shortcomings. Oscillometric methods measure BP at discrete time instances, while tonometry, for example, is an obtrusive and very sensitive to movement artefacts.

Electrical Impedance Tomography (EIT) is an imaging modality that has the potential to overcome these challenges, by assessing the health of the cardiovascular system continuously and non-invasively. The reconstruction of EIT images however, is a complicated process that involves a lot of input parameters, where different combinations of these parameters produce different images and consequently different physiological parameters. While there are efforts to address these issues, reconstruction parameters and analysis methods for the purpose of hemodynamics monitoring with EIT are still not standardized.

In this work a comprehensive analysis of the EIT imaging process for hemodynamic measurements was made in a series of experiments from in-silico to in-vivo measurements. The best performing reconstruction parameters and settings for hemodynamics EIT were selected in simulations and then used for image reconstruction. When using EIT, an accurate detection of the aorta is important for calculation of hemodynamic parameters. A novel algorithm for the detection of aortic pixels in EIT images is presented. The accuracy of the algorithm was validated on animal data with intermodal (computed tomography, F1-score 0.25) and intramodal (injection of contrast solution, F-1 score 0.8125) ground truth. In a next step, EIT signal was measured on 5 healthy volunteers and the location of the aorta was successfully detected with the algorithm. By exploiting ECG triggered ensemble averaging a representative aortic BP waveform was acquired which allowed for detection of BP pulse arrival time (PAT). As expected, a strong negative linear correlation was observed between the mean arterial BP and PAT detected with EIT (r=-0.8593).

The results of this work are quite promising and suggest that EIT assessment of hemodynamic parameters might be a viable alternative for current methods. The EIT technology is however still in its development phase and the various reconstruction algorithms available with their reconstruction settings have to be further tested on a larger scale followed by methodological in-vivo trials in order to pave its way to clinical use. A conference papers based on the results of this thesis was accepted for presentation at the 19th Electrical Impedance Tomography conference.

Kurzfassung

Herz-Kreislaufversagen tritt bei mehr als 20% der Intensivpatienten auf, was das Todesrisiko um das 12-fache erhöht. Zentrale hämodynamische Parameter wie Schlaganfallvolumen und Blutdruck (BP) haben sich als die besten Prädiktoren für verschiedene Herz-Kreislauf-Erkrankungen erwiesen, sind aber herausfordernd nicht invasiv zu überwachen. Die derzeitige Praxis für ihre Messung erfordert eine Katheterisierung, die mit gesundheitlichen Komplikationen und einer erhöhten Sterblichkeitsrate bei Patienten verbunden ist. Andere Methoden, obwohl nicht invasiv, versuchen, die zentrale Hämodynamik durch periphere Messungen zu approximieren und sind mit zusätzlichen Mängeln verbunden. Oszillometrische Methoden messen BP zu diskreten Zeitpunkten, während die Tonometrie zum Beispiel aufdringlich und sehr empfindlich auf Bewegungsartefakte reagiert.

Die elektrische Impedanztomographie (EIT) ist eine bildgebende Methode, die das Potenzial hat, diese Herausforderungen zu bewältigen, indem sie die Gesundheit des Herz-Kreislauf-Systems kontinuierlich und nicht-invasiv bewertet. Die Rekonstruktion von EIT-Bildern ist jedoch ein komplizierter Prozess, der eine Vielzahl von Eingabeparametern beinhaltet, wobei verschiedene Kombinationen dieser Parameter unterschiedliche Bilder und damit unterschiedliche physiologische Parameter erzeugen. Während es Bemühungen gibt, diese Probleme anzugehen, sind Rekonstruktionsparameter und Analysemethoden für das hämodynamische Monitoring mit EIT noch nicht standardisiert.

In dieser Arbeit wurde eine umfassende Analyse des EIT-Bildgebungsverfahrens für hämodynamische Messungen in einer Reihe von Experimenten von In-silico- bis In-vivo-Messungen durchgeführt. Die besten Rekonstruktionsparameter und Einstellungen für das hämodynamische EIT wurden in Simulationen ausgewählt und für die Bildrekonstruktion verwendet. Bei der Verwendung von EIT ist eine genaue Erkennung der Aorta für die Berechnung der hämodynamischen Parameter wichtig. Ein neuartiger Algorithmus zur Erkennung von Aortenpixeln in EIT-Bildern wird vorgestellt. Die Genauigkeit des Algorithmus wurde an Tierdaten mit intermodaler (Computertomographie, F1-Score 0,25) und intramodaler (Injektion von Kontrastmittel, F-1-Score 0,8125) Bodenwahrheit validiert. In einem nächsten Schritt wurde das EIT-Signal an 5 gesunden Probanden gemessen und der Ort der Aorta mit dem Algorithmus erfolgreich bestimmt. Durch die Ausnutzung des EKG-gesteuerten Ensembles wurde eine repräsentative Aorten-BP-Wellenform erfasst, die eine Detektion der BP-Impulsankunftszeit (PAT) ermöglichte. Wie erwartet, es wurde eine starke negative lineare Korrelation zwischen dem mittleren arteriellen Blutdruck und dem mit EIT nachgewiesenen PAT beobachtet (r=-0,8593).

Die Ergebnisse dieser Arbeit sind vielversprechend und deuten darauf hin, dass die EIT-Bewertung hämodynamischer Parameter eine brauchbare Alternative zu den derzeitigen Methoden sein könnte.

Die EIT-Technologie befindet sich jedoch noch in der Entwicklungsphase und die verschiedenen verfügbaren Rekonstruktionsalgorithmen mit ihren Rekonstruktionseinstellungen müssen in größerem Umfang weiter erprobt werden, gefolgt von methodischen In-vivo-Studien, um den Weg in die klinische Anwendung zu ebnen. Eine auf den Ergebnissen dieser Arbeit basierende Tagungsarbeit wurde zur Präsentation auf der 19 Elektrische Impedanz-Tomographie-Konferenz angenommen.

Acknowledgments

This thesis would have been impossible without the help of my supervisor and colleague DI. Florian Thürk. I want to express my deepest gratitude to him for introducing me to the real world of science and engineering and for pushing me ever so hard to strive for excellence, which led to my love for the subject of this thesis. His guidance in the process of planning and development of this work was invaluable.

Furthermore, I want to thank prof. Eugenijus Kaniusas for his wise advises when needed and at the same time granting me the freedom to explore this interesting subject as thoroughly as I desired.

I thank my companion and favorite person in this world Tsveta for her support and encouragement. I wish to also thank my family for the love and care they provided me with.

I want to thank my fellow biomedical engineering students Klaus Zeiner, Hoang Le and Tsvetan Yorov for participating in my experiments and for showing interest and support in my work. My gratitude goes to Ivan Kalev and Nikola Ezhkov who also volunteered for the in-vivo measurements.

I also want to thank all members of the Biomedical Sensing group at TU of Vienna and my colleagues at the Institute for Electrodynamics, Microwave, and Circuit Engineering.

Last but not least, I want to thank the members of the UKE, Hamburg for providing me with the animal measurements and for their friendly cooperation.

Table of Content

List of Abbreviations

A – Sensitivity matrix, Area

A^* - Matrix conjugate transpose

A^+ - Moore – Penrose pseudo inverse

A^{T} – Matrix transpose

AR – Amplitude Response

BP – Blood Pressure

C – Compliance

c – Molar concentration

CT – Computed Tomography

D – Desired image matrix

$\vec{D}$ – Electric flux density

E – Elastic modulus

$\vec{E}$ – Electric field density

E_s – Power spectral density

FEM – Finite Element Model

FOM – Figures Of Merit

f - Frequency

f_c – Cardiac Frequency

fEIT – Function EIT

GREIT – Graz consensus Reconstruction algorithm for Electrical Impedance Tomography

ECG - Electrocardiogram

EIT – Electrical Impedance Tomography

H_σ – Transfer function, Drichlet-to-Neumann map

h - Thickness of the vessel wall, height

I – Identity matrix

i – Imaginary number

$\vec{J}$ – Current density

$\boldsymbol{j}$ – Surface boundary current density

L – Number of electrodes

l – Length

M – Molar mass

MAP – Mean Arterial Pressure

MDBP – Mean Diastolic Blood Pressure

MSBP – Mean Systolic Blood Pressure

N – Number of samples, Number of pulses

NF – Noise Figure

$\vec{n}$ – Direction normal to a surface boundary

nf – Noise Figure

P – Pressure

ΔP – Pressure difference

PAT - Pulse Arrival Time

PE – Position Error

PEP – Pre Ejection Period

PTT – Pulse Transit Time

PWV – Pulse Wave Velocity

Q – Flow

R – Vascular impedance, Electrical resistance, Reconstruction matrix

r – Radius, Pearson's correlation coefficient

RES – Resolution

RNG – Ringing

SD – Shape Deformation

SNR – Signal to Noise Ratio

T – Sampling period, Period

TV – Tidal Volume

t – Time

ts – Target size

Δt – Time difference

V – Volume

v – Surface voltage

v_{h} –Homogenous voltage vector/ baseline voltage vector

wr – Weighting radius

x – Reconstructed EIT image

Δx – Distance

α – Regularization parameter

γ – Complex admittivity

ε - Permittivity

ϕ – Scalar electric potential

Λ_o – Molar conductivity

λ – Wavelength

ω – Angular frequency

ρ – Volumetric mass density

Σ_{t}^{*} - Target covariance matrix

Σ_{n} – Noise covariance matrix

σ – Electrical conductivity, standard deviation

$\vec{\nabla}$ - Nabla-operator

I. Introduction

Cardiovascular diseases are the number one death cause worldwide as reported by the World Health Organization [1]. They were the reason for more than 17 million deaths in 2015 compared to almost 13 million in 1990 [2]. Consequently, cardiovascular diseases are part of the cause of the ever-increasing healthcare costs worldwide. Hemodynamic parameters like a blood pressure and pulse arrival have shown to be great predictors for various pathologies related to cardiovascular diseases [3], [4]. Currently, ausculatory blood pressure measurement is the gold standard in a clinical setting or in the doctor's office [5], but it has serious drawbacks. For once, the use of inflating cuffs does not allow for continuous monitoring of beat to beat hemodynamic parameters. Moreover, the inflation of the cuff itself and the stress it imposes on the subject might influence the measurement, especially during sleep. Other options mostly used in critical care, although allowing for accurate and continuous measurement, require the insertion of a catheter, which is a highly invasive intervention and it is not certain if it improves overall patient outcome [6], [7]. Cardiovascular failure occurs in more than 20% of intensive care unit patients, which increases the risk of death by 12 fold by itself [8]. Therefore developing a non-invasive, non-obtrusive, cheap and continuous methodology for monitoring the hemodynamic parameters is essential for better diagnostics, improving patient's outcome and reducing the ever-increasing costs of hospitalization.

Electrical impedance tomography is a non-invasive imaging modality that injects non-sensational electric currents into the human body and reconstructs tomographic images by measurements of surface voltages. Usually, a belt of electrodes is attached to the skin over the area of interest and the output of the system represents a 2D conductivity maps that carry information about phenomena of interest. In contrast to catheterization, another continuous methodology for the monitoring of central hemodynamics, EIT is non-invasive and is not associated with health complications. Other non-invasive methods, like oscillometric, volume-clamp or tonometry blood pressure measurement have the disadvantage of approximating the central BP by measuring at distal sites – brachium, finger or wrist respectively [9].

The goal of this master thesis was to further build on the previous work on functional regions of interest detection and more precisely to develop a reliable methodology for detection of the aortic region in reconstructed Electrical Impedance Tomography (EIT) images.

First, the cardiovascular system and its physiology are discussed, followed by a closer look at the compliance and impedance of the circulatory system. Next, the important hemodynamic parameters blood pressure and pulse wave velocity (PWV) are reviewed and compared and their importance in the monitoring of cardiovascular diseases is highlighted. The subchapter concludes with an overview of the state of the art methodology for PWV measurement.

At the end of this chapter, the concepts behind EIT are introduced. First, a brief overview of the history of the technology is made, followed some existing EIT devices and their general structure. The chapter also includes the EIT working principles and the basic physical equations of EIT and a mathematical representation of the image reconstruction problem. The most important non-linear and linearized reconstruction strategies are discussed with a focus on the GREIT reconstruction algorithm and also the figures of merit that define the desired behavior of an EIT reconstruction algorithm are introduced. The section concludes with the physiological origins of the EIT signal.

In Chapter II, a systematic evaluation of some important parameters that might influence the reconstruction of EIT images is made. An important parameter called the noise figure, which controls the noise performance of the reconstruction is thoroughly analyzed in the context of aortic detection and monitoring of hemodynamics with EIT. A statistical evaluation of the figures of merit is made as influenced by the noise figure in simulations and the reconstructed structures in EIT images are validated from animal data versus a ground truth acquired by computed tomography. Additionally, the influence of the surface area of stimulating and measuring electrodes and their stimulation patterns on the reconstructed images is measured in a simulation by evaluating the performance of the figures of merit.

In Chapter III, EIT is tested as a non-invasive blood pressure monitoring device. An algorithm designed to detect the aorta in reconstructed EIT images is described and its performance evaluated. Physiological data from human subjects is measured and induced changes in the blood pressure are detected by measuring the pulse arrival time of the cardiac EIT signal.

In Chapter IV, a 3D EIT measurement strategy is investigated. Data from phantom objects is reconstructed with different inverse models and the quality of the image is evaluated. Additionally, the physiological experiments from the previous chapter are repeated in three dimensions in order to assess the advantages and drawbacks of this method by creating function EIT images. A 2D focused EIT method is employed that aims to overcome some of the traditional disadvantages of EIT reconstruction and the results are compared with the results from conventional 2D EIT strategies.

The work ends with conclusions of the findings, summary of the most important observations and outlook for future plans and projects.

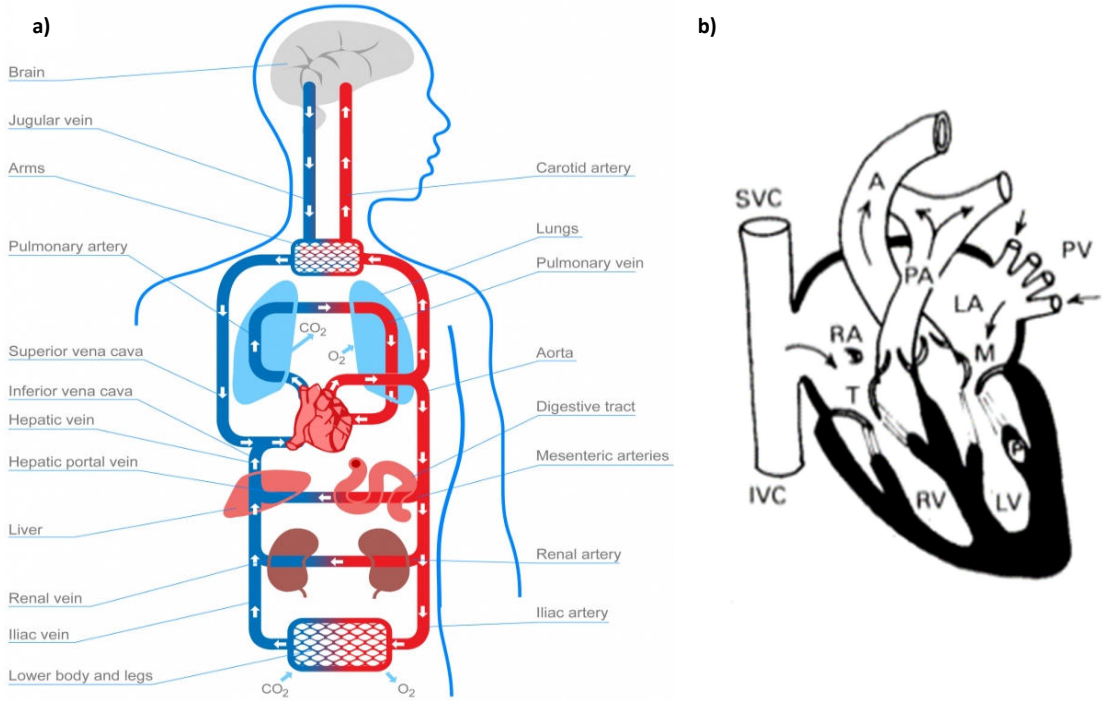

Figure 1. a) Schematic drawing of the cardiovascular system. Red paths show the routes of oxygenated blood, while blue paths show the routes of deoxygenated blood. Adopted from [102] b) Section through the heart showing the four chambers and the great vessels. Adopted from [4]

1. The cardiovascular system

This chapter provides a short overview of the cardiovascular system and some vital hemodynamics parameters.

1.1. Overview of the cardiovascular system

The cardiovascular system consists of the heart, the blood vessels, and the blood and together with the lymphatic system builds the circulatory system (Figure 1a). The cardiovascular system can be subdivided into the systemic and pulmonary circulations. The role of the former is to supply the organs and tissues with oxygenated, nutrient-rich blood from the left ventricle of the heart through the arteries to the capillaries and to drain deoxygenated blood, rich in metabolites[1] and transport it from the capillaries back to the right heart where it enters the pulmonary circulation through the right ventricle and pulmonary artery. There the blood is oxygenated again in the lungs and goes back to the left heart to be pumped into the systemic circulation and the circle closes. The cardiovascular system also has a

[1] On its way to the heart right heart, metabolite rich blood passes through the kidneys and liver in order to extract and then secrete the metabolites.

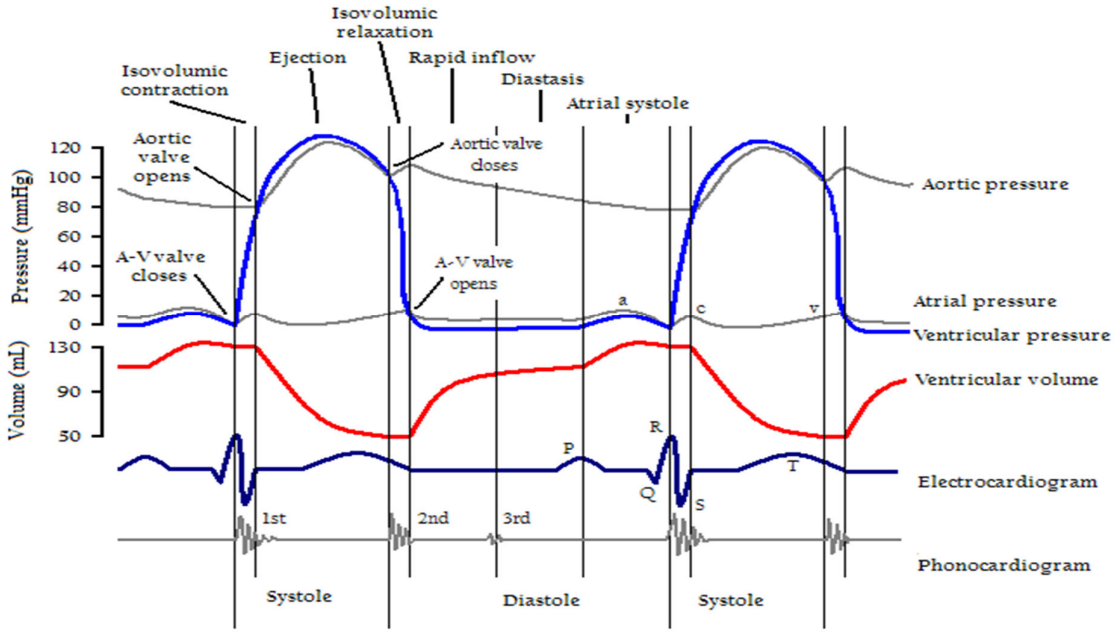

Figure 2. The Cardiac cycle**.** Two whole cardiac cycles with important cardiac events noted and the most important cardiovascular bio signals plotted. Adopted from [103]

important role in distributing hormones that control certain processes among which is the control of the blood pressure. Part of the kinetic energy of the blood traveling through the vessels is transformed to heat through friction and that heat is also distributed by the cardiovascular system to various parts of the body [10].

The heart is a muscular organ that works as a pulsatile pump in order to promote blood flow (Figure1 b). It has four chambers – two ventricles and two atria – and four unidirectional valves. The ventricles and the atria are comprised of two separate muscles that are electrically isolated from each other and innervated by a sophisticated system of nerve fibers [11].

The cardiac cycle (Figure 2) begins with the filling of the ventricles – beginning of the diastole. That is the longest part of the cycle accounting for around 66% of the total period [10]. First, both atria are passively filled from the major veins of the circulatory system – the superior and inferior vena cava and the pulmonary vein and some of that blood also enter both ventricles through the atrioventricular valves. This phase ends with a contraction of the atria that forces additional blood to enter the ventricles. The cardiac cycle continues with an isovolumetric contraction – the beginning of systole. In this brief phase, the pressure in the ventricles becomes higher than the pressure in the atria due to contraction of the ventricular muscles, which closes the atrioventricular valves. When the ventricular pressure becomes higher than the arterial pressure, the valves of the ventricles open and the blood is ejected into the arteries. Then the muscles relax and the whole process can start again.

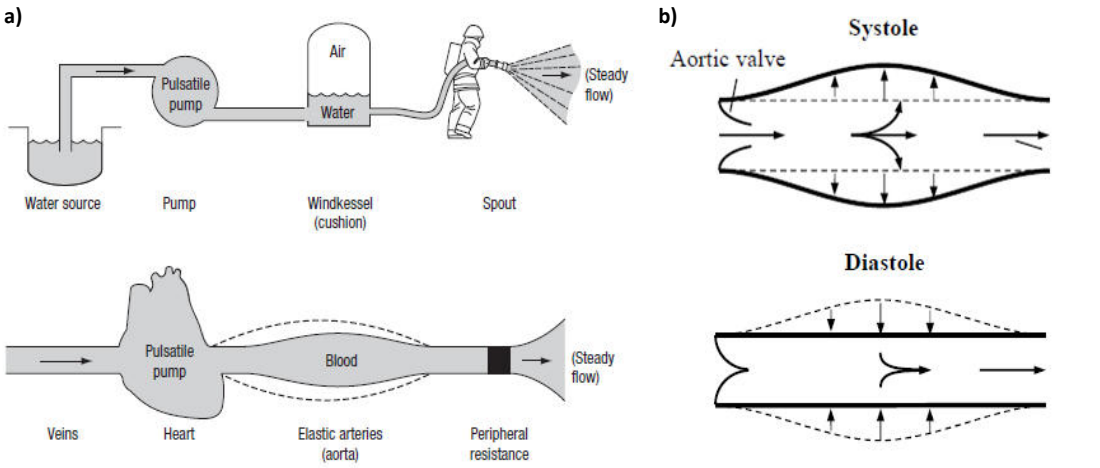

Figure 3. a) The windkessel analogy. The cardiovascular system is compared to a watering system with a pulsatile pump and a buffering reservoir that ensures a steady flow. Adopted from [10] b) The aorta distends during systole in order to accommodate the blood pumped by the heart and stores its energy in form of elastic energy. During diastole the aorta contracts and ensures semi constant flow Adopted from [8]

The mechanical energy produced by the heart is buffered by the compliant aorta in form of a potential energy in order to promote a semi-steady flow through high the pressure part of the systemic circulation. On the other hand, the low-pressure part of the systemic circulation serves as a reservoir for the heart. In that sense, the cardiovascular system can be compared to a windkessel – a pulsatile pump with a reservoir and an air chamber that provides cushioning and continuous flow [11] (Figure 3).

Compliance is a property of the blood vessels and describes the change in the blood volume of a vessel due to a change of the pressure of the vessel.

$$C = \frac{\Delta V}{\Delta P} \tag{1}$$

If the vessels were perfectly stiff, then the pressure during systole would be very high and then drop to zero during diastole. Therefore the blood flow would also stop during diastole because of the relation between a flow of a fluid and the pressure gradient.

$$\Delta P = QR \tag{2}$$

Where Q is the blood flow and the proportionality factor R is the vascular impedance. Fortunately, the human body has evolved to have compliant vessels to synergize with the pulsatile nature of the heart. All blood vessels except for the capillaries have similar three layer structure with varying thickness and function (Figure 4) [10]. These layers comprise of:

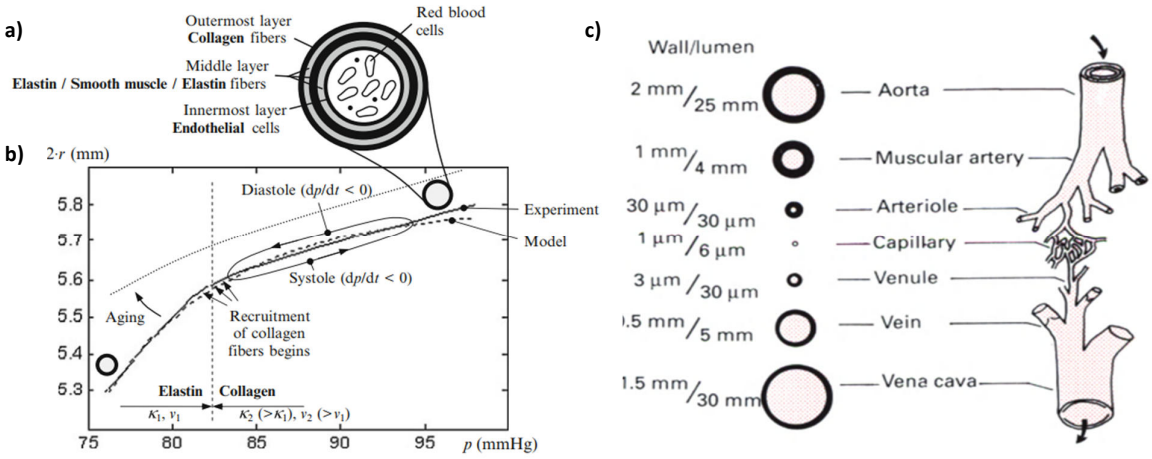

Figure 4. a) Shows general structure of the wall of a blood vessel. b) The relationship of pressure and radius of a blood vessel. The relationship is nonlinear and reflects the recruitment of the various layers with increase in pressure. The vessels become less and less compliant with an increase in blood pressure .Adopted from [11]. c) Wall thickness of vessels along the cardiovascular tree. Adopted from [10]

- the innermost layer – tunica intima, consists of a thin layer of endothelial cells and is mechanically weak
- the middle layer – tunica media, consists of elastin fibers that are responsible for the compliance of the vessels and smooth muscles that play a role in vasoconstriction and vasodilatation
- the outer most layer – tunica adventitia, consists of collagen fibers that give the blood vessels a sturdy structure and help to attach to nearby organs and tissue.

In addition to transporting blood, most blood vessels also have a further function which is reflected in the composition of their layers. The Aorta, for instance, has a middle layer very rich in elastin, which helps it distend and receive the stroke volume of the heart followed by a recoil until the next heart cycle, thereby ensuring a semi-constant blood flow (Figure 3b). Other large arteries – like the radial and coronary artery – have a middle layer rich in smooth muscle allowing them to contract and cease the blood flow to a part of the body as needed. The arterioles have the highest ratio of wall thickness to vessel radius among all blood vessels and they contribute the most to the total impedance to blood flow (Figure 4b). There is a non-linear dependence of the radius of the blood vessels and the blood pressure which is depicted in Figure 4a and reflects the composition of the vessel wall [11].

1.2. *Blood pressure*

The blood pressure in the arteries is not constant over the cardiac phases and oscillates between a systolic and diastolic value. When the heart starts ejecting blood during the systole the blood pressure starts to rise from its diastolic value because the inflow of blood in the vessels is more than the outflow through the periphery due to the peripheral resistance. When entering the aorta, the newly ejected blood

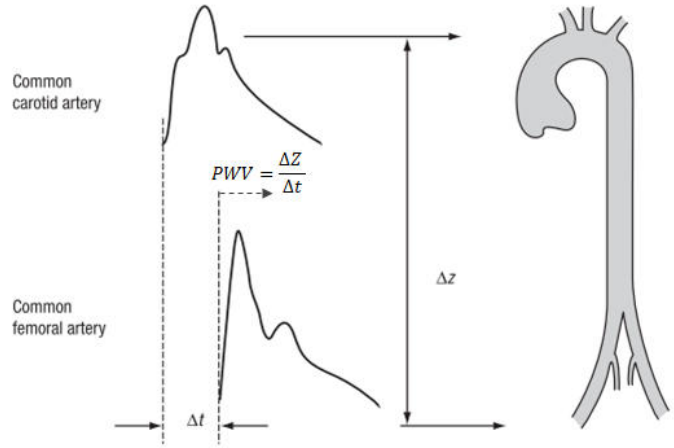

Figure 5. The pressure wave form changes with distance from the heart due to the change in structure of the blood vessels along which it travels. The femoral artery is stiffer than the aorta, therefore the pressure wave is also steeper there. The PWV is equal to the ratio of distance travelled to time $\frac{\Delta Z}{\Delta t}$ .Adopted from [101]

pushes against the walls of the aorta and also tries to displace blood that previously occupied this space thus creating flow (Figure 3). The blood pressure reaches its maximum when the inflow of blood equals the outflow and then starts decreasing until it reaches its minimum in late diastole. Due to the compliant nature of the vessels, the pressure does not rise instantaneously along the arterial tree, but in fact, the pressure wave travels with a finite velocity, for example in the aorta between 4-10 m/s. The velocity of the pressure wave should not be confused with the velocity of the flow, which is about an order of magnitude less in the aorta and has normal values of around 0.2 m/s (0.7 m/s peak velocity) [10].

1.2.1. Factors affecting the blood pressure

There are several regulatory systems that control the blood pressure. The two branches of the autonomous nervous system – the sympathetic and parasympathetic – respectively increase and decrease the cardiac frequency and thus blood pressure. The sympathetic activation is also independently related to increased arterial stiffness [12]. The kidneys also play a vital role, by producing a hormone called angiotensin, whose role is to send a signal to the blood vessels to constrict, thus raising blood pressure [13]. The endothelium itself – a part of the vessel wall, also has a functional role in the regulation of the compliance of the vessels, by releasing the vasodilator nitric oxide and the vasoconstrictor endothelin [14]. Various pathologies in the aforementioned systems can lead to deviations of the blood pressure from its norm.

The form of the pressure wave is different along the arterial tree, because of the different stiffness of the vessels along which it travels. The stiffer the vessels become with the distance from the heart, the steeper the pressure wave becomes, because there is less 'cushioning' (Figure 5). With increasing age, the constant distention of the elastic vessels will break the elastin fibers and they will be replaced by collagen, thus increasing arterial stiffness and deforming the pressure wave [15]. The incident pressure

wave will also be reflected at bifurcations and will superimpose on itself. The sum of the incident and the reflected wave results in the blood pressure wave [16]. With increasing arterial stiffness, both the incident and the reflected wave will travel faster along the arterial tree. As a result, the reflected wave then might reach the heart during systole instead of diastole, increasing systolic pressure and decreasing diastolic pressure and thus also increasing the pulsatile part of the pressure wave. Organs like the brain and the kidneys are especially susceptible to such widenings in the blood pressure wave because they are perfused at a high volume of blood during both diastole and systole. Moreover, their vascular resistance is low and thus they are directly exposed to the pulsations of pressure and flow and often suffer injuries of their vasculature [17],[18],[19].

The ideal blood pressure is thought to be 120/80 mmHg [20], but there are various external and internal factors that can affect the blood pressure and force it to deviate temporary or long-term from this norm. With age, the arteries become increasingly stiffer and that leads to a permanent increase in systolic blood pressure and therefore higher amplitude of the waveform. Blood pressure also varies temporary during sleep and exercise. During exercise, the blood vessels become stiffer and also the cardiac output increases, because of the higher demand for blood flow thus increasing blood pressure, while during sleep the blood pressure drops immensely. Stress can also induce an increase in the blood pressure [10].

1.2.2. Pulse wave velocity

The Pulse Wave Velocity (PWV) is a parameter that reflects the speed with which the blood pressure wave travels along the arterial tree. It relates the distance between two measuring sites Δx and the time delay Δt of the wave to the distal measuring site with respect to the proximal (Figure 5) [21].

$$PWV = \frac{\Delta x}{\Delta t} \tag{3}$$

The Moens-Korteweg equation shows that the PWV is proportional to the square root of the elastic modulus of the artery along which it travels [22].

$$PWV = \sqrt{\frac{Eh}{2r\rho}} \sim \sqrt{E} \tag{4}$$

Where E the elastic modulus of the wall of the vessel is, h is the wall thickness of the vessel, r is the inner radius and ρ the blood density. For large arteries like the aorta, the wall thickness to vessel diameter radius $(\frac{h}{r})$ is almost invariant, so PWV can be assumed to be directly proportional to the elastic index of the vessel. PWV is a characteristic parameter for the stiffness of the vessels and is a good predictor for a variety of pathological conditions [3], [4].

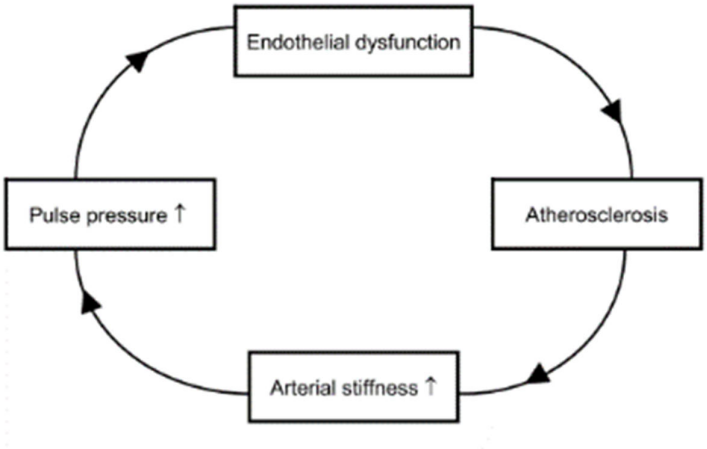

Figure 6. The vicious circle of events – Endothelial dysfunction leads to Atherosclerosis leads to increased arterial stiffness leads to higher blood pressure and the circle continues. Adopted from [6]

As shown in Figure 4 a) the relationship between blood vessel radius and blood pressure is non-linear. The blood vessels become stiffer with increasing blood pressure, which in turn yields higher PWV and consequently earlier return of the reflected pressure wave and thus increase in blood pressure. In other words, an increase in blood pressure results in a feedback augmentation and even higher blood pressure. In pathological cases, this sequence of events is sometimes called the vicious circle and it starts with endothelial dysfunction and Atherosclerosis that leads to loss of elasticity of the vessels and increased blood pressure (Figure 6).

1.2.3. State of the art in PWV measurement

Equation 1.3 serves as the basis of PWV measurement for most state of the art devices available. As a first step Δt has to be determined, also called Pulse Transit Time (PTT), by measuring the time delay of the arrival of the pressure wave, generally at one distal and one proximal point along the arterial tree. Next, the distance between the two measurement sites has to be determined, which is a task that each manufacturer has a different recommendation regarding its derivation, but it usually involves a tape measurement between specific superficial anatomical locations [23].

One group of devices measures the arrival of the pressure pulse at two major arterial sites, one as close to the aorta as possible and one distal [4]. The proximal measurement site is often at the carotid arteries while the distal site is at the common femoral arteries, thus the segment of the arterial tree between those is considered a representative of the aorta, i.e. aortic PWV is derived.

As already discussed, the incident blood pressure wave is reflected at major arterial bifurcations and at the arterioles [24], thus the superposition of incident and reflected wave results in the complete blood pressure wave. The time of the arrival of the reflected wave would affect the shape and morphology of the whole wave and this is the phenomena that the second group of devices tries to exploit for PWV

measurement. Commonly, the arrival of the reflected wave at the iliac bifurcation is of interest and the time it takes of the pressure wave to travel from the heart to the iliac bifurcation and then back to its origin is measured, while Δx from eq. 1.3 is equal to two times the length of the aortic segment along which the pressure wave travels.

Another approach that is often employed for PWV measurement is the use of ECG gating to assess PTT [21]. The R-peak in ECG is assumed to coincide with the genesis of the pressure wave and the arrival of the wave is measured at a distal site. However, this assumption ignores the existence of the Pre-Ejection Period (PEP). During the R-peak, the muscular tissue of the ventricles is electrically innervated and starts to contract, but it isn't before the ventricular pressure exceeds the aortic pressure when the aortic valve opens and generates the pressure wave. On the other hand, if one is interested not in absolute values of PWV, but the temporal changes thereof are of interest, the PEP can be ignored and the R-peak can be used as a physiological landmark for the genesis of the blood pressure wave.

2. Electrical Impedance Tomography

Electrical Impedance Tomography is an imaging modality that reconstructs the impedance distribution within an object by injecting electrical current and measuring surface voltages. Usually, a pair of electrodes is used for injection of current while all other are measuring potential differences. By taking a number of such measurements it is possible to estimate the impedance distribution within a system [25]. EIT is most commonly used to reconstruct 2D slices of an object corresponding to the plane in which the electrodes are attached, but lately, there have been efforts to reconstruct images from systems with more electrode planes and even 3D images [26], [27]. EIT has the advantages over traditional clinical imaging modalities of being noninvasive, affordable and portable. It also has a very high temporal resolution, which makes it a perfect candidate for real-time monitoring of changing physiological signals, however, it suffers from low spatial resolution compared to other tomographic modalities, like computed tomography (CT).

Typically, the technique is practiced in the medical research of lung pathologies, since breathing strongly modulates the conductivity of the lungs tissue and thus can be easily visualized [28],[29],[30],[31]. Lately, the ability of EIT to assess various cardiovascular parameters has been intensively researched [30],[32],[33],[34], due to its potential strengths compared to state of the art methods. Other common applications are in the field of geophysics. A similar technique to medical EIT is used to probe deep underground structures and is capable of detecting various ores, monitor mixtures of conductive fluids [35] or test agricultural soils [36].

The technology has several strategies for image reconstruction the most important and widely used for medical purposes being time-difference EIT (tdEIT). In tdEIT images of the change in conductivity

compared to a reference frame are reconstructed. First, the forward problem is solved in order to find the sensitivity function of the system and then its approximate inverse, which will serve as a reconstruction matrix. This mode is the most robust to noise and easiest to linearize and also takes advantage of the fact that most physiological phenomena of interest are periodical [37]. Respiration as a periodic phenomenon and images of the lungs being a good example for tdEIT.

It is also possible to reconstruct absolute images of the conductivity with absolute EIT (aEIT), but the solution is very sensitive to movement artifacts and to the knowledge of the electrode position. The aEIT reconstruction algorithm is non-linear and takes much more computation time compared to tdEIT, but the advantage is that by reconstructing absolute images, a different type of information is acquired. A good example of aEIT in medicine is tumor detection and in the industry, it is used for detection of ores.

The third type of reconstruction strategies takes advantage of the different behavior of tissues at different frequencies. In frequency-difference EIT (fdEIT) the systems would be electrically stimulated with two different frequencies and a difference image would be acquired. Tissues that exhibit dispersion would be visible with fdEIT. A medical example where fdEIT is used is the detection of brain tumors.

2.1. Historical development

The development of EIT can be traced back to the Schlumberger brothers who showed that by injecting current into the earth the surface voltage measurements [38] can be used to detect ores that lie deep underground. They discovered that by varying the spacing between electrodes, they would get information about the resistance of different depths. The first medical impedance images are attributed to Henderson and Webster [39]. In 1978 they designed and built and impedance camera that consisted of 100 electrodes on one side of the chest and one big electrode on the other. They were able to produce images of the underlying tissues, where regions with low conductivity were qualified as lungs. The work concluded that in the future a visualization of respiration and localized perfusion should be possible. Almost 10 years later in 1987, the first clinical EIT system came to life. At that time the technology was called applied potential tomography and was developed by Brian Brown and David Barber in the Department of Medical Physics at Sheffield University. The system used 16 electrodes placed around the thorax of the patient and it is still in use to this date [40]. Since then EIT has been researched intensively as a medical instrument for lung imaging [30], [31],brain imaging [41],[42], breast imaging, [43][44], bladder imaging [45], [46] and cardiovascular imaging [33], [34], [47].

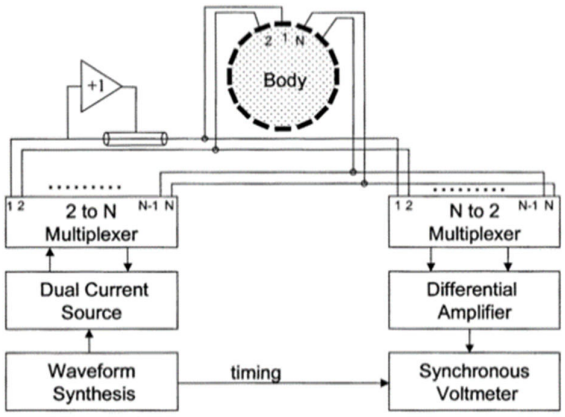

Figure 7. General structure of an EIT system. The waveform synthesis block creates a sine wave and also synchronizes the measurement and stimulation. The sinewave is turned into an alternating current by the current source and passed to a multiplexer that routes the current between pairs of electrodes in turn. Another multiplexer is responsible for connecting the measuring electrodes to a differential amplifier and a voltmeter. Adopted from [40]

2.2. EIT devices

It has been estimated that over 50 different EIT devices have been developed since its invention over 30 years ago [31]. Table 1 shows some of the most popularly used EIT devices and some of their characteristics.

As it can be seen from table 1 different systems use a different number of electrodes, different stimulation patterns, and different reconstruction algorithms. Some systems use individual electrodes, while others use electrode belts, which enables easier application and more accurate spacing. The Swisstom AG system also offers adjustable skip of injecting electrodes, which is a very useful feature in research applications.

A general EIT system includes several important blocks illustrated in Figure 7. It all starts at the waveform synthesis block which synthesizes a waveform, usually a sine wave, which is then passed to the current source block, which produces two signals equal in amplitude but with an opposite sign. The multiplexer then uses those signals to stimulate the system between each pair of electrodes in turn, according to the stimulation pattern. The current then travels to the body under investigation through often shielded cables in order to reduce interference and capacitive effects, in addition, some systems have also developed active electrodes which pre-amplify the signal. On the other side, another multiplexer connects a voltage amplifier with each set of measuring electrodes in turn. The amplified signal is then passed to a voltmeter that is controlled by synchronization trigger from the waveform synthesis block. There are various alterations that can be made to this general model. For example, systems exist that have multiple current sources [48]. This enables a better distinguishability of the system and increases the signal to noise ratio (SNR) which in turn reduces the amount of regularization

Table 1. EIT devices manufacturers and their respective EIT system with number of electrodes and a short list of characteristics. Adopted from [31]

Manufacturer	EIT system	Electrodes (number, configuration)	Characteristics
CareFusion	Goe-MF II	16, individual electrodes	Pair drive (adjacent), serial measurement. Algorithm: Sheffield back-projection
Dräger Medical	PulmoVista 500	16, electrode belt	Pair drive (adjacent), serial measurement. Algorithm: FEM-based Newton-Raphson method
Maltron Inc	Mark 1 Mark 3.5	16, individual electrodes 8, individual electrodes	Pair drive (adjacent), serial measurement. Algorithm: Sheffield back-projection
Swisstom AG	BB^2	32, electrode belt	Pair drive (adjustable skip), serial measurement. Algorithm: GREIT
Timpel SA	Enlight	32, electrode stripes	Pair drive (3-electrode skip), parallel measurement. Algorithm: FEM-based Newton-Raphson method

that has to be made during reconstruction [49]. It is far more important that the current source is precise instead of being accurate, especially for time-difference EIT and especially for multiple current source systems. Other systems might use multiple voltmeters instead of a multiplexer to increase the data collection speed and hence the frame rate of the device [50].

The quality of the EIT data is highly reliant on the precise positioning of the electrodes, precision of the applied stimulation current and of course the precision of the measured voltages. Errors in any of those mentioned factors will lead to a deterioration of the data. The resolution of EIT is additionally determined by the number of electrodes and the measurement precision. However, it is impossible to reconstruct more than $\frac{L*(L-1)}{2}$ conductivities with L electrodes [40], because $L * (L-1)$ is the number of transfer admittances that can be measured with L electrodes and only halve of the admittances are unique because of reciprocity of measurements [51].

2.3. EIT working principle

The goal of Electrical Impedance Tomography is to reconstruct a 2D (or 3D) map of the conductivity distribution of a volume from surface voltage measurements. The EIT reconstruction problem is defined mathematically as a non-linear ill-posed inverse problem [40]. Several factors contribute to that. First, the diffusive nature of the current flow leads to a higher sensitivity of the system to certain regions – meaning the relationship between conductivity as a function of position and surface voltage is not linear. Furthermore, the measured voltages are always influenced by measurement uncertainty and different

sources of noise [52]. The third of Jacques Hadamard`s conditions for a well-posed problem (existence, uniqueness, and stability) does not hold, namely, the final solution for the conductivity distribution is very sensitive to changes in the measured voltages. In other words, the matrix that represents the linearized transformation of voltages to conductivities has a high conditioning number – is ill-conditioned. This means that the solution will tend to over-fit to the measurement data. One solution to this problem is to assume some prior information – for example smoothness of the solution. This technique is called regularization and is of utmost importance in EIT. Prior knowledge about the underlying properties of the system in question can further make the ill-conditioning less severe. Such information might include, the shape of the boundary of the system in question, expected shape of inner structures and their conductivity ranges, correlation between conductivities, expected noise of the measurement system and induced error due to linearization. All of this information is summarized by the additional terms that are added to the inverse solution.

2.3.1. Theoretical background

Two equations from the theory of electromagnetism govern the physics of EIT assuming negligible magnetic effects – the Kirchhoff's law and Ohm's law. Kirchoff's law, also current conservation law, states that the current entering a closed surface $\partial\Omega$ is equal to the current leaving the surface given there are no current sources enclosed by the surface. This can also be re-phrased in mathematical sense as the divergence of the current density $\vec{J}$ at a closed surface being zero (eq. 6). Ohm's law states that the current that flows through a resistive load is proportional to the voltage drop across the load. The generalized version of Ohm's law (eq.7) was formed by Kirchoff, where the electric field $\vec{E}$ and the current density $\vec{J}$ at each point in space are proportional and σ is the conductivity of the material.

$$\vec{\nabla} \cdot \vec{J} = 0 \tag{6}$$

$$\vec{J} = \sigma \vec{E} \tag{7}$$

The electric field can be expressed as the gradient of the scalar potential ϕ (3).

$$\vec{E} = -\vec{\nabla}\phi \tag{8}$$

Substituting (8) in (7) and then in (6) results in:

$$\vec{\nabla} \cdot \sigma \vec{\nabla}\phi = 0 \tag{9}$$

Knowing the potential ϕ at the boundary and the conductivity distribution σ within the volume Ω allows for a unique solution of (9) for ϕ.

$$\boldsymbol{j} = -\vec{J} \cdot \vec{\boldsymbol{n}} = \sigma \vec{\nabla}\phi \cdot \vec{n} \tag{10}$$

Similarly, knowledge of the current density at the surface boundary $\boldsymbol{j}$ is sufficient to determine a unique solution for ϕ up to an additive constant. From (eq. 6) follows that the sum of all $\boldsymbol{j}$ has to be equal to 0. Therefore, by applying current $\vec{J}$ in a direction $\vec{\boldsymbol{n}}$ perpendicular to the boundary the system responds with a potential ϕ. The function $H_\sigma : \boldsymbol{j} \rightarrow \phi$ is the transfer function of the system that uniquely maps the applied currents to surface potentials and carries the information of the underlying conductivity distribution of the system. H_σ is also often called the *Dirichlet-to-Neumann map* because it relates current normal to the boundary – Neumann boundary conditions – with the potential at the boundary – Dirichlet boundary condition. Kohn and Vogelius [53] have shown that the knowledge of ϕ and j at every point across the boundary surface will be sufficient to determine the underlying conductivity distribution.

Modern EIT systems use kHz frequency alternating electric current for stimulation. Consequently, the conductivity σ can be extended to the complex admittivity of the system (eq. 11), which is the reciprocal of impedance, hence the name Electrical Impedance Tomography.

$$\gamma = \sigma + i\omega\varepsilon \tag{11}$$

As it can be seen from (eq. 11), the complex admittivity γ has a term that is frequency dependent, where ε is the permittivity of the system. Tissues will have different admittivity at different frequencies, which becomes useful in frequency-difference EIT.

The permittivity is an intrinsic property of any material and relates the electric field $\vec{E}$ with the electric displacement field $\vec{D}$.

$$\vec{D} = \varepsilon\vec{E} \tag{12}$$

Any material that is under the influence of an electric field will try to align its free charged particle with the applied electric field. When talking of biological tissues, the first polarization mechanism[2] is cell membrane polarization, where the charged particles that swim in the intracellular fluid, will try to move towards the membrane and align themselves with the electric field.[54] After the frequency of the electric field becomes high enough, so that the big charged proteins and other charged macromolecules cannot follow, this effect will become negligible (Figure 8). This is called β-dispersion and occurs at frequencies up to 100MHz [55]. For frequencies up to 30GHz, the smaller polar molecules (e.g. water) in the biological tissues affected by the electric field will try to rotate and align themselves with it. This polarization mechanism is called dipole polarization and is related to γ-dispersion. Finally, for frequencies up to 100THz ,the electron cloud that surrounds the nucleus shifts itself under the effects of an alternating electric field. This polarization mechanism called displacement polarization cannot

[2] Alpha dispersion strictly speaking is the first known polarization mechanism, but its cause are not well known and its frequency range – in the hertz range – is not relevant for EIT

occur

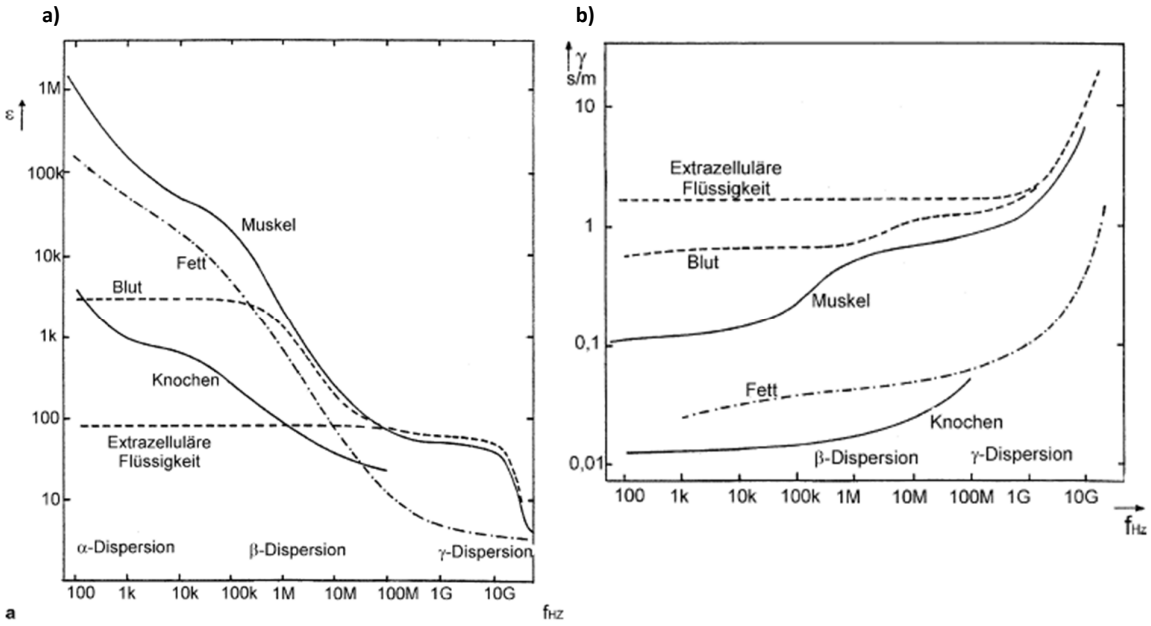

Figure 8. Dispersion curve from 50Hz to 100GHz for a) the permittivity and b) the admitivity of diverse biological tissues. Adopted form [49]

for frequencies above 100THz. Those so called dispersion mechanisms, affect the ability of a material to be polarized under the effect of an external electric field. Actually, the permittivity of the material ε is affected and from eq. (11) follows that also its admittivity and therefore also the EIT signal changes.

The effect a conductivity inhomogeneity may have on the current density distribution and electric field within a body are discussed next. For simplicity, it is assumed that the body in question and the inhomogeneity both have a circular geometry. Figure 9 shows the situation for homogenously distributed conductivity. The equipotential lines will be perpendicular to the current density lines (red arrows). When an inhomogeneity is added to the geometry, in this case, a circular body with lower conductivity than the surrounding medium, (Figure 9) the equipotential lines will be "drawn" towards the body. From eq. (7) follow that a less conductive body will have a larger voltage drop across it, in other words, there will be more equipotential lines within a region when the conductivity of the region decreases and less equipotential lines when its conductivity increases. This effect is clearly seen in Figure 9. Figure 9c shows the situation with a little more complex geometry that resembles the human thorax. It can be seen how the less conductive lungs have numerous potential lines going through them compared to the heart, which in this case is shown to be at the same potential. For the simulation, the conductivity of the lungs was set to 0.2S/m, heart – 1.5S/m, background – 1S/m, stimulation current – 5mA [37]. The bottom image in figure 9c shows even more accurate situation, because the contours of the thorax, the lungs, and the heart were segmented from a CT-image of a real human thorax. Again it can be seen, how the potential lines are less dense in the heart region and denser in the lungs. Therefore,

in principle, one should be able to reconstruct the conductivity distribution of a body from surface voltage measurements, especially if there is a sufficient number of measurements.

Another interesting characteristic of the behavior of the system can be seen from these experiments. The lower the spatial frequency[3] of the stimulation current the higher the sensitivity of the system is too deep regions [56]. That can be seen by simply counting the potential lines that go through the circular inhomogeneity. In the adjacent stimulation case, only 2 potential lines go through the object, while in the opposite stimulation case 6 potential lines are going through the object. That means that the voltage drop across it will be higher, hence higher sensitivity.

2.3.2. Mathematical representation and regularization

The goal of EIT image reconstruction is to retrieve σ from H_σ. Mathematically speaking, this is a non-linear ill-posed inverse problem. If, the conductivity and current were known and the problem was to determine the voltage at the surface boundary it would be equivalent to solving the forward problem. The forward problem is usually well-posed and easy to solve with numerical methods, e.g. finite element method. According to Jacques Hadamard, there are three criteria that a well-posed problem should fulfill [57]:

1. A solution should exist.
2. The solution should be unique.
3. The solution should change continuously with the initial conditions.

In the previous chapter, it was mentioned that the uniqueness has been shown under various assumptions, at least for the continuous case, where the current density normal to the boundary and the electric potential at the boundary is known for every point. This is not the case in the real world because it is possible to measure the potential at an only finite number of places, or in the case of commercial EIT system only 32 places[4]. The continuity of the solution, however, is what causes problems. Due to the diffuse way the electrical current propagates the EIT system is more sensitive to superficial regions compared to deep regions. It can be shown that at a certain precision there always will be an inhomogeneity of a certain size that cannot be detected no matter how high its contrast is [56]. This fact illustrates the violation of the third of Hadamard's condition for well-posedness.

Mathematically the problem can be expressed as:

$$Ax = v \tag{13}$$

[3] The spatial frequency describes how often the system is stimulated in the space domain. An adjacent stimulation pattern would have much higher spatial frequency compared to opposite stimulation pattern.
[4] In reality, depending on the system settings, the injecting electrodes, their first and/or second neighbors and depending on the stimulation patterns, also the electrodes in between might not be measuring voltages.

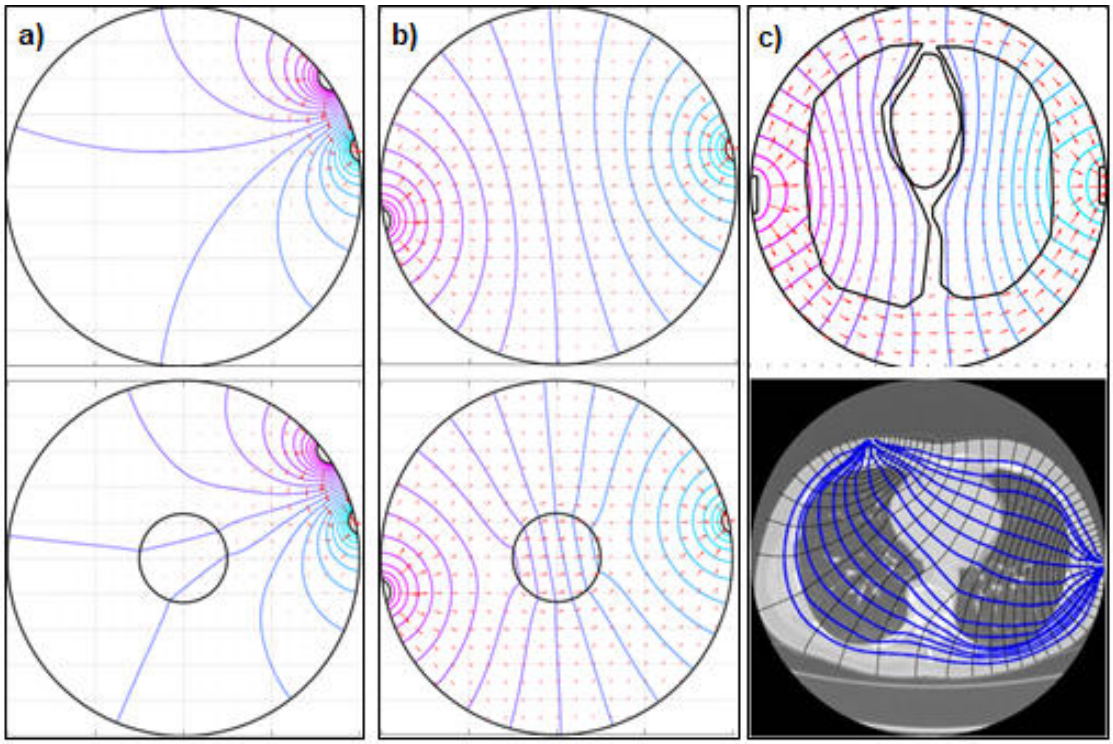

Figure 9. Equipotential lines in EIT a) Top - homogeneous circular geometry with adjacent stimulation and with a circular inhomogeneity bottom b) Top - homogeneous circular geometry with opposite stimulation and with a circular inhomogeneity bottom c) Top - Illustration of the possible potential field lines and current density lines distribution in the human thorax. Bottom - Potential lines and current density lines distribution with a model of a real human thorax. Adopted from: [104]

In the case of linearized EIT reconstruction, the matrix A represents the Jacobian matrix of the system that gives the sensitivity of the voltage of each electrode $v_l^k$to the respective finite element x_n in the finite element mesh and the respective stimulation pattern (1…K).

$$A = \begin{bmatrix} \frac{\partial v_1^1(x)}{\partial x_1} & \cdots & \frac{\partial v_1^1(x)}{\partial x_N} \\ \vdots & \ddots & \vdots \\ \frac{\partial v_L^K(x)}{\partial x_1} & \cdots & \frac{\partial v_L^K(x)}{\partial x_N} \end{bmatrix} \tag{14}$$

The solution for x can be determined given A and v by:

$$x = A^+ v = (A^* A)^{-1} A^* v \tag{15}$$

Here A^+ is the Moore-Penrose pseudo inverse and A^* is the complex conjugate of matrix A. The problem is that as shown previously the matrix A is ill-conditioned that is, its conditioning number is high. This means that the solution will tend to over-fit to the measurement data. Therefore, regularization can be used and solve:

$$x_\alpha = (A^* A - \alpha^2 I)^{-1} A^* v \tag{16}$$

With the correct choice of the hyperparameter α the matrix in the brackets is not ill-conditioned and the equation can be solved for x_α. A tradeoff has been made between finding the real answer and finding a reliable answer. This technique is called Tikhonov regularization and the parameter α is the regularization parameter. There are various techniques for choosing α which will be discussed in more detail in Chapter II. In eq. (16) the identity matrix can be substituted with a regularization matrix that holds all sorts of prior information available about the conductivity distribution of the system including smoothness of the solution, boundary shape (segmented from CT images or measured with bend sensors[58]), expected shape of inner structures and their conductivity ranges , correlation between conductivities and induced error due to linearization [25].

2.3.3. Reconstruction Algorithms

The first available medical EIT device used back-projection algorithm to reconstruct tomographic images. The back-projection algorithm is a linear algorithm developed by Barber and Brown [59] that uses a transformation, similar to the radon transform used in CT. However, in EIT the projection of conductivities happens on equipotential lines in contrast to its CT counterpart where the projection happens on a straight line, due to differences in propagation of electrical current and x-rays. A circular geometry with homogenously distributed conductivity produces the potential line distribution from Figure 9a top. Any introduced inhomogeneity will cause an increase in the electrode voltage readings behind it (from the viewpoint of injecting electrodes), which can be seen in the reduced distance between equipotential lines in Figure 9a bottom. By doing a full circle of injection between pairs of adjacent electrodes and measurement with others, the superposition of the voltage profiles after filtering will result in the conductivity distribution within the body. However, the back projection algorithm is limited to only circular geometries, adjacent stimulation and has no way to suppress corrupt data [60].

Other reconstruction algorithms use a so-called sensitivity matrix (eq. 14). By creating a finite element model of the system and simulating the effects of conductivity changes on the measured surface voltages, the sensitivity matrix of a system can be acquired. The advantages of this method over the equipotential lines back projection is that the FEM can be defined with any geometry and stimulation patterns. It is generally a 3D model compared to the 2D model in back projection, thus reflects more accurately the voltages measured further away from the stimulation, because the sensitivity decreases faster with distance in 3D. Further assumptions about the model, like conductivity distribution of the background, simulation of electrode movement (important for in-vivo imaging) and noise modeling can further improve the accuracy of the sensitivity matrix. The Gauss-Newton algorithm is a least square iterative solver for non-linear problems that is used to reconstruct EIT images. It seeks to find the best solution similar to Newton's method for finding a minimum of a function, but it neglects terms involving second derivatives, which reduces computation times [40]. Equation 16 can be re-written for the Gauss-Newton algorithm:

$$x_{n+1} = x_n + (A_n^* A_n - \alpha^2 I)^{-1} A_n{}^* v_n \quad (17)$$

Where, A_n is the sensitivity matrix calculated at the nth iteration, v_n is the difference voltage vector minus the simulated voltages at nth iteration. Ideally, the algorithm should converge to a v_n that is equal to zero, meaning the approximated conductivity distribution within the body produces the same voltage signal as the measured one.

Between 2007 and 2009 a group of EIT experts developed the consensus reconstruction algorithm GREIT [61]. The algorithm is based on an approach, where a reconstruction matrix is optimized such as to satisfy a set of criteria called figures of merit (FOM). The process of optimization is very similar to regularized image reconstruction process of the Gauss-Newton algorithm [37], however, the reconstruction matrix is the subject of the optimization function rather than the reconstructed image.

GREIT solves the forward problem in order to obtain some values for the sensitivity matrix (Eq. (14)). First, the FEM of the system is created and the stimulation and measurement patterns are defined. The FEM represents the geometry of the system, size, position and contact impedance of the electrodes and the conductivity distribution of the system around which the solution will be linearized. In addition to the forward model, GREIT defines also a noise model, which models measurement and electrode movement noise. The measurement noise is generally modeled as Gaussian white noise, however, that is not necessarily true for all measurement setups and for best performance of the algorithm the measurement noise can be calibrated at the start of the measurement.

Then, GREIT starts placing targets with a known radius and conductivity within the FEM and simulates currents and measures voltages. The targets that are placed by the reconstruction algorithm are equally distributed within the measurement plane in order to assess the influence of each element on the surface voltages. To this end, when a single target is placed, each pair of electrodes takes a turn to stimulate the system while each pair of voltages is measured. The result is a column in the sensitivity matrix from Eq. (14). Then a new target is placed in a different position and another column is acquired. Additionally, each pixel value in the reconstruction matrix is assigned with a weight such as to best satisfy the desired behavior of the FOM, which is the central point of GREIT.

The figures of merit are a set of criteria that were proposed by the Graz EIT consensus to characterize the performance of an EIT reconstruction algorithm. Each of these FOM has some desired behavior and sometimes there is a tradeoff between them. In other words, optimizing one desired criteria

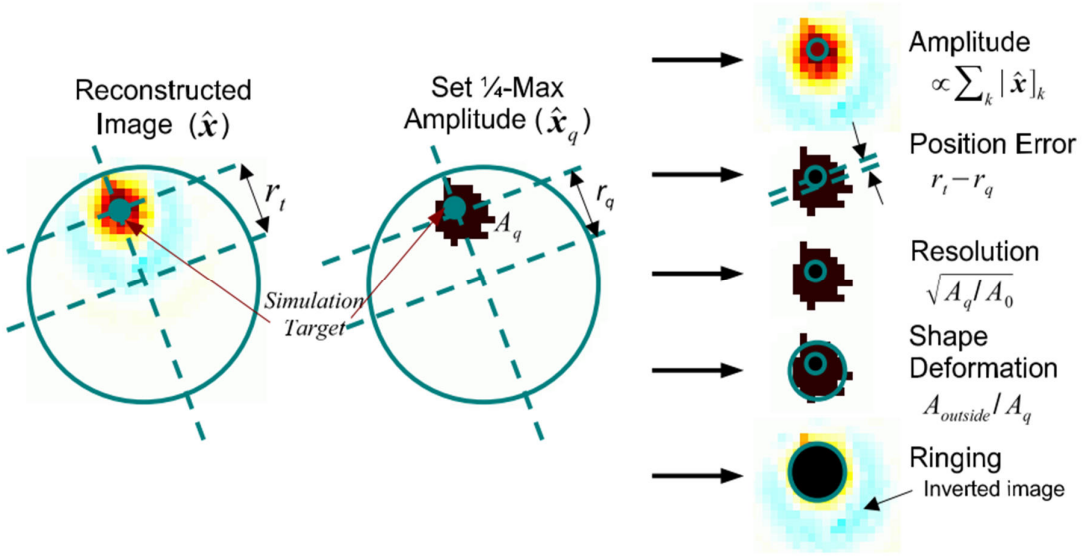

Figure 10. Figures of merit designed to evaluate the performance of a reconstruction algorithm for EIT. From the reconstructed image (right), a set of pixels with amplitude larger than ¼ of the maximal reconstructed amplitude is selected. Figures of merit are ordered by importance – top to bottom. Adopted from [61]

can lead to worse behavior of another. Therefore, the FOM are categorized by importance by taking into account the implications of them performing undesirably [61].

The most important criterion for the performance of an EIT reconstruction algorithm is to have a uniform amplitude response (AR). The amplitude response is defined as the sum of the amplitudes of all pixels of the reconstructed image divided by the conductivity of the target multiplied by its volume. Uniformity of AR is best reflected in the standard deviation of the FOM as a function of position. This is, of course, important because if the amplitude response is not uniform, the same amount of conductivity change due to a physiological function (or dysfunction) will be differently reconstructed depending on the location of the phenomena and that would make the EIT images very difficult for interpretation.

The second most important FOM is the position error (PE). PE is defined as the distance between the center of gravity of the reconstructed image of the training target and the set of pixels representing amplitudes higher than 1/4th of the maximal amplitude of the reconstructed images. It is desired that the PE is small and shows low variance. The source of a physiological phenomenon would be impossible to identify if the reconstruction algorithm shows large PE and the situation would become even more difficult if the PE is a function of position, which is reflected in the variability of the PE.

A good EIT reconstruction algorithm should also have uniformly distributed and small resolution [61]. Resolution (RES) is important because it allows distinguishability of small structures. RES as a FOM is defined as the area of the set of pixels representing amplitudes higher than 1/4th of the maximal amplitude of the reconstructed target image divided by the area of the whole image.

The fourth place of importance goes to shape deformation (SD). SD is defined as the fraction of the pixels representing amplitudes higher than 1/4th of the maximal amplitude of the reconstructed target image that does not fit in a circle with the same area. Large SD may result in an incorrect interpretation of structures within the reconstructed images. The desired behavior of this FOM again is to have low value and variability.

Ringing (RNG) reflects the tendency of some algorithms to project a ring-shaped region with opposite sign of impedance change around a target. RNG is the sum of all pixels with a sign opposite to the sign of the reconstructed target. For example, when the lungs decrease their conductivity during inspiration the ringing with opposite sign of conductivity change – increased conductivity, can be misinterpreted as the heart. This is also known as overshoot and it is best if this effect is low and uniform.

After all those considerations, the reconstruction matrix of GREIT is:

$$R = D\Sigma_{\mathrm{t}}^{*}A^{T}(A\Sigma_{\mathrm{t}}^{*}A^{T} + \alpha\Sigma_{\mathrm{n}})^{-1} \tag{18}$$

Where, D stands for desired image matrix, with weights assigned for each pixel in order to best fulfill the desired performance of the FOM, Σ_{t}^{*} is the target covariance matrix, which adjusts for training bias, A is the Jacobian of the system holding sensitivity values for each electrode to each finite element and stimulation pattern, α is the regularization parameter, also called hyperparameter, which controls the noise performance of the system and Σ_{n} is the noise covariance matrix that models the measurement and movement noise of the system.

Difference images can thus be produced by simple matrix multiplication:

$$x_{\mathrm{n}} = R(v_{\mathrm{h}} - v_{\mathrm{n}}) \tag{19}$$

Where, x_n stands for the nth image frame, v_n is the nth surface voltage measurement and v_{h} is the baseline voltage vector used for difference EIT imaging.

2.4. Origin of the voltage changes in the EIT signal

Electrical Impedance Tomography measures the voltage drop between a set of electrodes as a result of high frequency injected current. As seen in chapter 2.2.1. all possible combinations of current to voltage relations are summarized in the transfer admittance matrix H_σ. The conductivity σ is a local material characteristic and is related to the total resistance by:

$$R = \frac{l}{\sigma * A} \tag{20}$$

The EIT signal has a variety of different origins. For example, one of the most popular medical EIT signals is the one coming from the lungs during respiration. Here, the alveoli (Figure 11a) fill with air and expand during inspiration, making the path of the current that can travel through the blood vessels

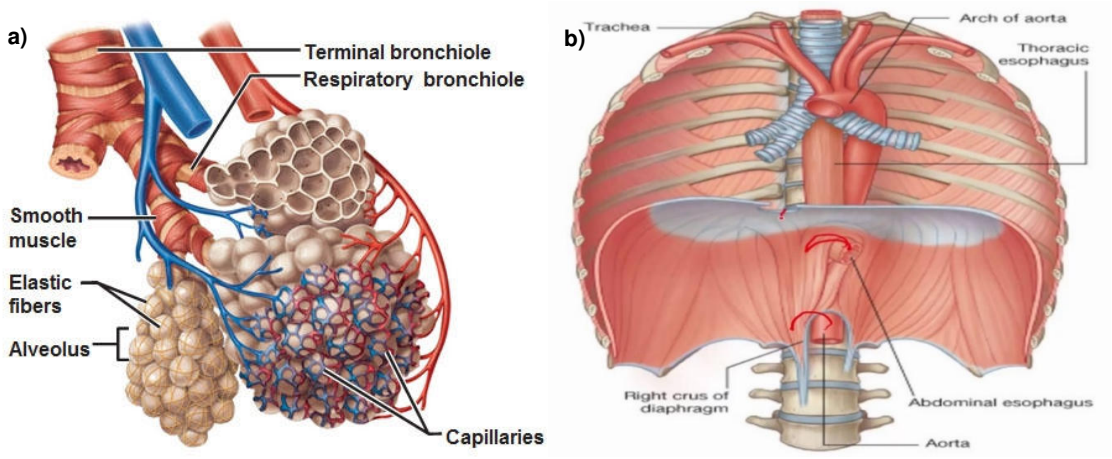

Figure 11. a) The alveoli are surrounded by blood vessels which are preferred path for the current due to the high conductivity of blood. Adopted from [105] b) The diaphragm is a muscle that contracts in expiration and relaxes in respiration and has a hole in it through which the descending aorta enters the abdominal cavity. Adopted from [106]

surrounding the alveoli longer [31],[55]. This, in turn, raises the total resistance that the current 'sees' (eq. (11)). Therefore, in this case, the global material property R changes, not the local property σ.

Another important EIT signal is the signal that comes from a beating heart. There are two major guiding phenomena that produce the EIT signal. First, during systole the heart that is filled with blood contracts and empties its contents into the aorta and pulmonary artery. This results in a decrease of local conductivity σ and volume of the chambers of the heart, because the blood, which is usually more conductive than other tissue, has been ejected. During diastole, the opposite happens. An increase in the conductivity and volume of the chambers is observed, because the blood from the large veins is filling out the emptied heart [62]. The second source of the cardiac EIT signal are the so called cardioballistic effects. During systole, when the heart ejects blood in the arteries, the whole organ contracts and also moves as a result of the rapidly ejected blood [62], [33]. The effect on the EIT signal is that a tissue with high conductivity (heart muscle/blood) will enter an area previously occupied by less conductive tissue (lungs) and that will modify the equipotential lines and the measured surface voltage (Figure 9c).

A signal that is of the most interest for this work is the aortic EIT signal. Unfortunately, its origins are still not well understood, but it is assumed that its source is the pressure wave that travels through the aorta. Due to the distensibility of the aorta, the pressure that builds up after ventricular ejection will travel along the aortic tree and will expand the walls of the aorta. Again, an area previously occupied by a less conductive tissue will be replaced by the blood-filled aorta and that would change the local conductivity and result in a decrease of the voltage measured. The space in the thoracic and abdominal

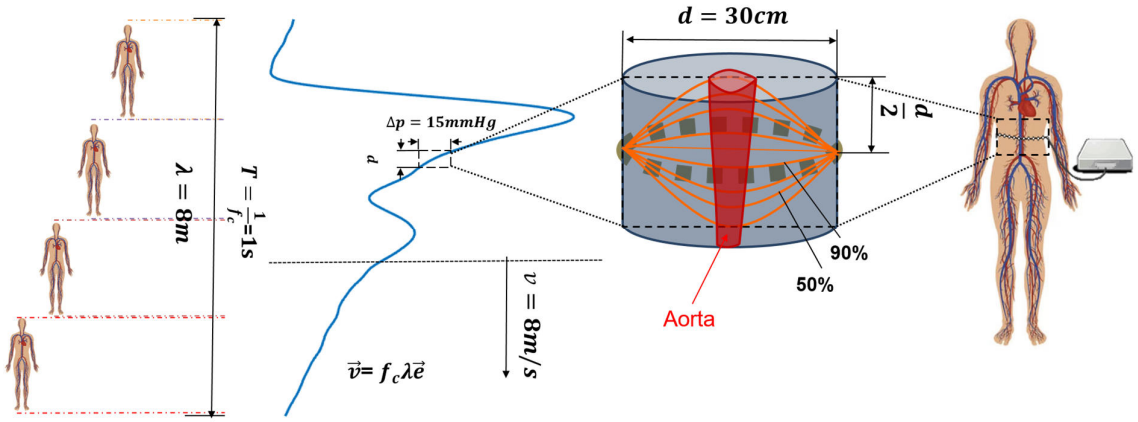

Figure 12. The wavelength of the blood pressure wave could be four times longer than the whole human body. The sensitivity of EIT is not confined to a single plane, but the system is sensitive to a lens shaped region (orange lines) spanning ½ of the diameter of the body above and below the measuring plane. Anatomical image taken from: [107]

cavity is very efficiently used. Movement of some organs – heart, lungs, and diaphragm – will also displace others – e.g. aorta. This means that for example, during respiration the position of the aorta in the abdominal cavity will be modulated by the diaphragm (Figure 11b) and should result in visible conductivity changes in the EIT signal.

Figure 12 depicts the situation of blood pressure measurement with EIT and gives some perspective on the scales of the structures and phenomena involved. It was shown earlier how the blood pressure wave arises as a result of the pumping action of the heart and travels with a finite velocity along the elastic arteries. The velocity of the pressure wave v can be expressed as a ratio of its wavelength λ and its period T.

$$v = \frac{\lambda}{T} = \lambda f_c \tag{21}$$

As seen in Chapter 1.3. the velocity of the pressure wave is usually in the range of 4-10 m/s. If a heart rate of $f_c = 60$ beats per minute is assumed (1Hz) and a pressure wave velocity of 8m/s and substituted in eq. (21), the resulting wave would have a wavelength of 8m. Consequently, at a single time instance, the whole human body of a relatively tall person (2m height) would be subjected to a segment of the pressure wave of length ¼ of its wavelength (Fig. 12 left). Due to the diffusive nature of current propagation, EIT is sensitive to a lens-shaped region that spans up to ½ the diameter of the body below and above the plane of the electrodes with decreasing sensitivity in the axial direction. Therefore, the EIT measurement, in this case, can be seen as a weighted sum operation. The radial distension of the aorta varies in axial direction within the sensitivity region, caused by different local pressure would result in different resistivity for the current traveling from one electrode to the other, but would then all be attributed (reconstructed) on a projection region on the transverse electrode plane

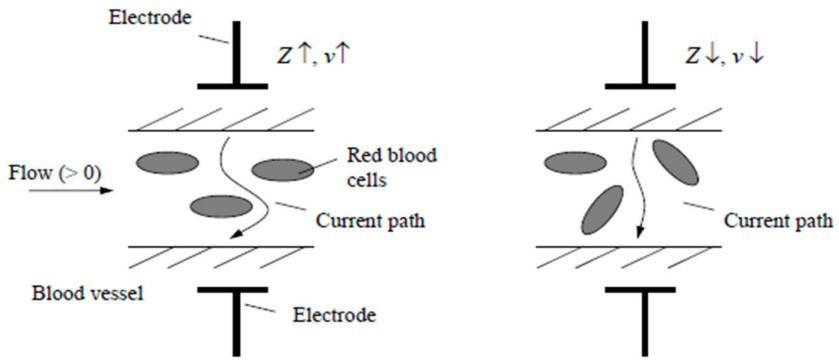

Figure 13. Blood flow and conductivity realtionship. With an increase of the blood flow, the red blood cells become more ordered and force the electric current to take a longer path while traveling in a perpendicular to axial direction, thus increasing impedance. Adopted from slides of the lecture Biomedical Sensors and Signals by E. Kaniusas

- mathematically this is a summation. Moreover, the current density decreases with axial distance from the electrode plane, therefore the conductivity changes there would yield lower voltage change compared to regions close to the electrode plane – mathematically this is weighting. In the worst case scenario - during the anacrotic limb of the pressure wave – the EIT sensitivity region will be exposed to a pressure difference of about 15mmHg given a body diameter of 30cm and blood pressure of 120/80mmHg. Additionally, a single point of the pressure wave would pass through the sensitivity region in $t = \frac{s}{v} = \frac{0.3}{10} = 0.03s$. With a sampling frequency of 50Hz each point will be on average $n = \frac{t}{T_{\text{sampling}}} = \frac{0.03}{0.02} = 1.5$ times weighted summand of an EIT frame.

2.5. Factors affecting blood conductivity

The blood is a conductive tissue thanks to dissolved charged molecules and ions that float freely in it. Electrolytes like Sodium and Chloride and various charged proteins facilitate the current conduction. The content of carbon dioxide also influences the electrical properties of the blood. It acts as a buffer and the following reaction governs the pH of the blood:

$$CO_2 + H_20 \rightleftharpoons H_2CO_3 \rightleftharpoons HCO_3^- + H^+ \tag{22}$$

The red blood cells that are also constituents of the blood have an enzyme – carbonic anhydrase that increases the reaction rate, producing more charged species HCO_3^- and H^+ [63]. Obviously increasing the ion content also increases the conductivity of blood, therefore the lower the pH value and also the higher the CO_2 content, the higher the conductivity of blood. This founding implies that deoxygenated venous blood should be more conductive than oxygenated aortic blood.

Hematocrit is defined as the volume concentration of red blood cells in the blood. It has been shown that the enzyme that the red blood cells contain indirectly modifies the electrical conductivity of the

blood, but the hematocrit itself also has an influence on the electrical properties of the blood. Red blood cells are not conductive themselves and an increase in hematocrit leads to an increase in blood viscosity and a decrease in conductivity because the current has to take a path around the red blood cells. With an increase in blood flow, also the conductivity decreases in a direction perpendicular to the axial direction of a blood vessel (Figure 13.)[64][65]. Finally, the perceived conductivity of a material is a function of the stimulation frequency as described in chapter 2.3.1, due to dispersion effects.

II. Evaluation of image reconstruction

1. Motivation

Until recently little work was done in the direction of EIT as a tool for hemodynamics parameter monitoring, but lately more research is emerging in the scientific literature [34],[66],[32],[67]. Consequently, the proper reconstruction parameters that ought to be used are still unknown. Due to the ill-posed nature of the EIT reconstruction problem, the use of different algorithm parameters results in vastly different reconstructed images [37]. Those facts and the fact that the interpretation of the EIT images requires expert knowledge are the reason why EIT, a technology with great potential is still not used in clinical setting and were also the inspiration for the subject of this chapter.

In this chapter, the influence of the choice of the regularization hyperparameter on the quality of the reconstructed image was investigated with the help of the figures of merit defined by Adler et al. [68]. Furthermore, the ability of an algorithm designed for the aortic search to correctly identify the aorta depending on the hyperparameter was tested and the best performing hyperparameters found. The results are compared with the popular heuristic approach of determining the hyperparameter - the L-curve [69]. Furthermore, the influence of the electrode size on the quality of the reconstructed image for ten different electrode sizes and different stimulation patterns was tested.

2. Methods

2.1. Study protocol

The EIT data was measured in anesthetized piglets during mechanical ventilation as a part of a larger study [70]. The datasets would usually start with a few breathing cycles followed by an apnea period (Figure 15). The EIT measurement plane was at the level of thoracic vertebra 9 and 10. Parallel to the EIT data acquisition also ECG data, aortic flow, aortic blood pressure and other physiological signals were recorded, but unfortunately, they were not always synchronized, so their validating power is limited. Nevertheless, computed tomography scans of the pigs were also provided, which were used to extract useful anatomical information. Segmentations of the thorax, right and left lung and aorta at the level of the EIT measurement plane were manually taken with the help of the CT image tool ITK-Snap [71]. The corresponding contours were then used to create individual finite element models (FEM) (Figure 14) with the help of MATLAB (The MathWorks Inc., Natick, MA, USA), NETGEN [72] and the EIDORS framework [73]. More details on the study protocol and ethics approval are provided in the next chapter.

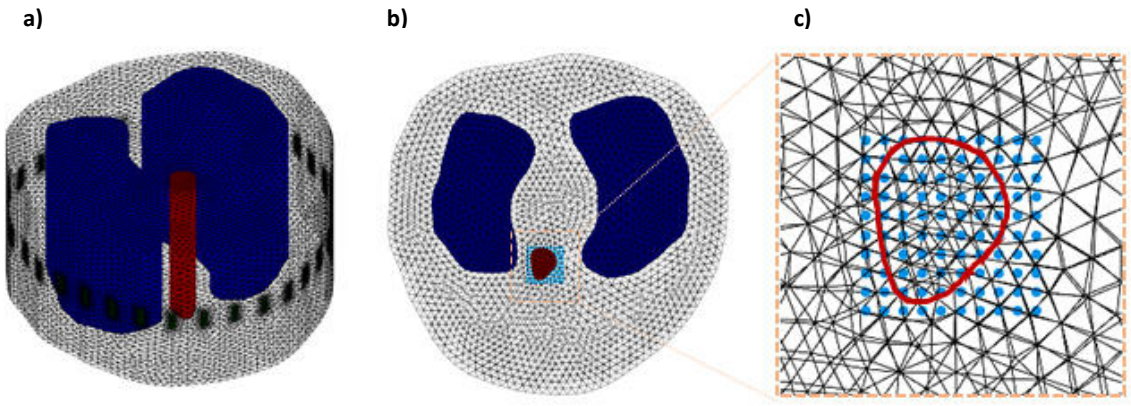

Figure 14. a) Finite element model of the Pig b) FEM top view with simulation targets. c) close up of the simulation targets. Lungs are colored in dark blue, the aorta is in red and simulation targets in light blue

2.2. Noise figure tests

The Noise figure approach is a state of the art approach of selecting the appropriate value for the regularization hyperparameter for a certain measurement setup [74]. It relates the signal to noise ratio (SNR) of the raw voltage signal SNR_v to the SNR in the reconstructed images SNR_{x}.

$$NF = \frac{SNR_{\mathrm{v}}}{SNR_{\mathrm{x}}} \tag{23}$$

A single pig was then chosen and 20 inverse models with GREIT and a noise figure NF ranging from 0.5 to 2.4 were created. One hundred targets were then placed in the region where the aorta is in a rectangular grid (Figure 14bc). The radius of the targets was chosen to be around 2% of the diameter of the thorax, which was 200mm. The forward problem was then solved, to simulate the effect the targets would have on the measured surface voltages for each model. The performance of all 20 reconstruction models was then compared with the help of the mean values and standard deviation of figures of merit proposed by the Graz EIT consensus [68]. As discussed in Chapter I section 2.3.3. both absolute value and spatial consistency (standard deviation) of the figures merit are relevant for the performance of an algorithm.

Additionally, each reconstruction model was used to reconstruct abdominal images of pigs from the physiological data, which were used for aorta detection with a basic implementation of a search algorithm. The quality of the reconstruction was assessed based on the ability of the algorithm to detect the aorta.

2.3. Aortic search algorithm

As a first step of the algorithm, the part of the signal that contains the breathing cycles is located. With the help of that signal, a tidal volume image - TV is produced (Figure 15). To this end, the average of the difference of all inspiration and expiration images is calculated – Eq. (24). $x_{\mathrm{insp_i}}, x_{\mathrm{exp_i}}$ are the reconstructed images at full inspiration and expiration respectively and N is the number of breathing cycles.

$$TV = \frac{1}{N}\sum_i^N x_{\mathrm{insp}_i} - x_{\mathrm{exp}_i} \tag{24}$$

$$x_{\mathrm{insp}_i}, x_{\mathrm{exp}_i}, TV \in \mathbb{R}^{64\times 64} \tag{25}$$

The lung region of interest (ROI) is then defined by applying a threshold criterion and excluding all pixels below this threshold th (Eq. (26), where TV_{lk} represents a pixel of the tidal volume image).

$$ROI_{\mathrm{Lung}} = \begin{cases} 0, & for\ TV_{\mathrm{lk}} < 0.1 \cdot \max TV \\ 1, & otherwise \end{cases} \tag{26}$$

The two biggest connected regions of connected pixels are chosen to represent the lung ROI.

The heart rate is then identified by applying a fast Fourier transformation (FFT) to the mean EIT signal and selecting the highest frequency component. The mean EIT signal is defined in Eq. (27), where x_{lki} is the pixel at position lk at time instance i.

$$EIT_{mean_i} = \frac{1}{64*64}\sum_{l,k}^{64} x_{\mathrm{lki}} \tag{27}$$

The heart rate is then used to produce a power spectral density map of the EIT dataset. To this end, the FFT of each individual pixel is computed and the magnitude of the spectrum at heart frequency represents the value of this pixel in the PSD map.

$$PSD(f_{Heart})_{lk} = \sum FFT(x_{lk})_{f=f_{\mathrm{Heart}}} \tag{28}$$

Afterwards, regions with high activity at the heart frequency are identified by applying a threshold criterion (*th*=0.05) and excluding all pixels below some threshold in PSD map.

$$ROI_{\mathrm{Heart\ activity}} = \begin{cases} 0, & for\ PSD_{\mathrm{lk}} < 0.05 * \max PSD \\ 1, & otherwise \end{cases} \tag{29}$$

The biggest region is identified as the heart and the second biggest region is identified as the aorta.

The locations of the identified structures with the help of the above-mentioned algorithm are validated by comparing them with the segmentation from the CT images and computing distance and F1-score. The F1-score is a measure of the accuracy of a binary classification that takes into account both the

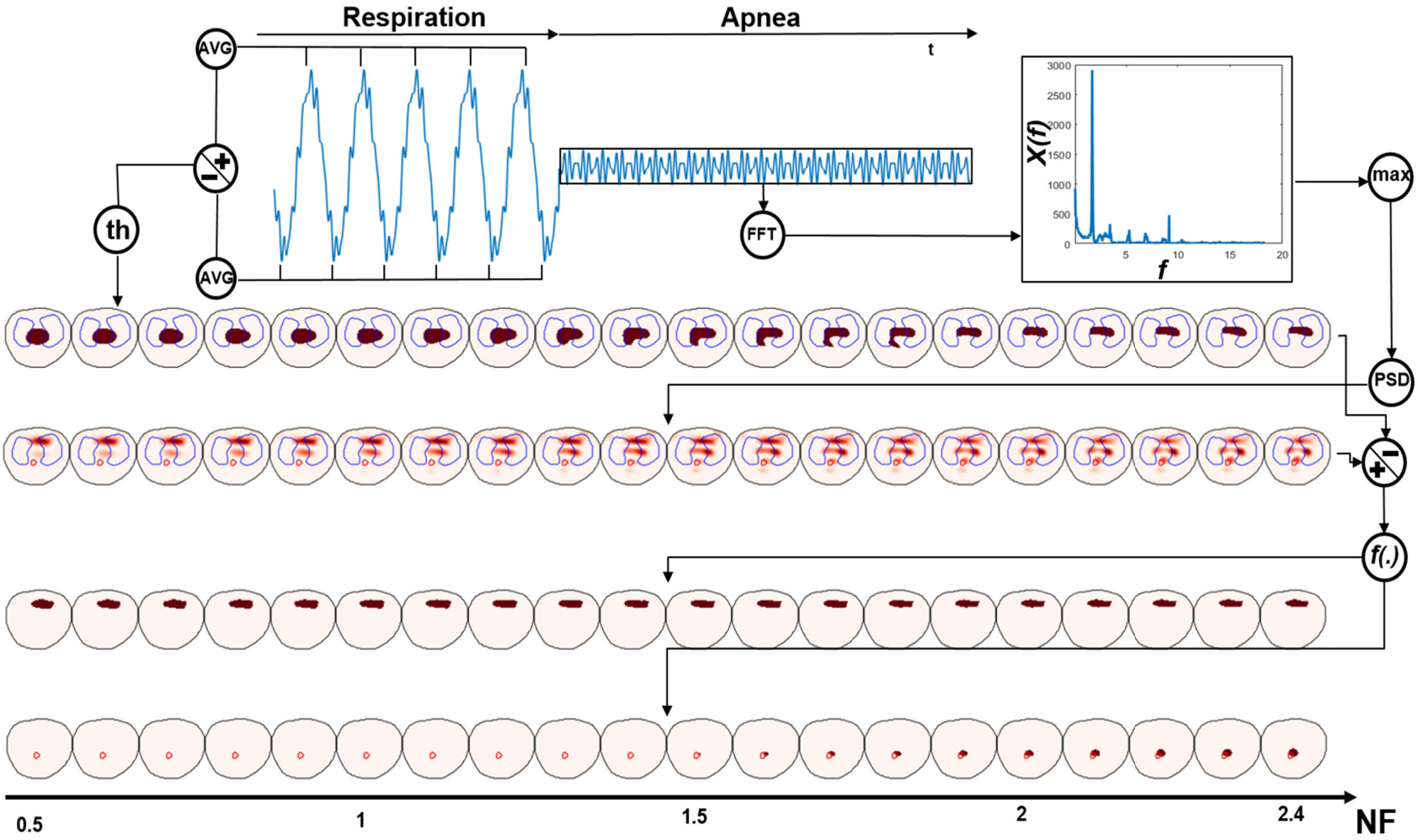

Figure 15. Schematic representation of the aortic search algorithm. First the lung ROI is detected through setting a threshold on a tidal volume image. Then the apnea period is detected and the cardiac frequency is found, by transforming the signal in the frequency domain and detecting the strongest oscillation frequency. The power spectral density at cardiac frequency is computed in order to isolate regions that exhibit cardiac activity. Finally, the lung mask is subtracted from the power spectral density map and the second biggest connected region is labeled as the aorta. The detected aorta is validated versus aortic segmentation from CT and F1-score and distance are calculated.

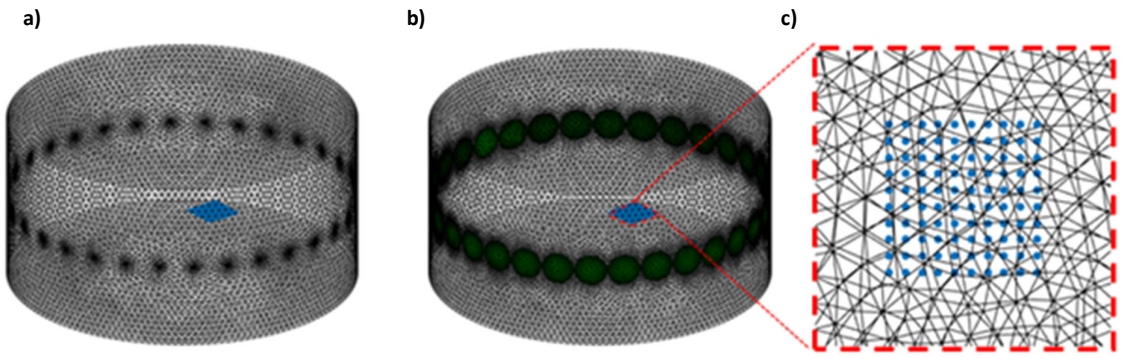

Figure 16. a) FEM with smallest electrode size *r* =0.005m b) FEM with largest electrode size r=0.05m c) location of the targets

precision and the recall of the classifier. Additionally, the results of the aortic search algorithm were evaluated, based on a distance of the center of the detected region with EIT to the center of the segmented aorta from the CT images.

2.4. Influence of the electrode size

For the electrode size investigation, all results were simulated. First, ten FEM`s were created each with different electrode size (Figure 16 ab). The selected FEM geometry was cylindrical with a radius of 0.52m, a height of 0.5m and had a single plane of 32 electrodes with varying size of the radius from 0.005m to 0.05m with 0.005m step. Then 100 targets with a radius of 0.01m were placed in a grid where the abdominal descending aorta ought to be (Figure 16c) and three different stimulation patterns were applied – adjacent stimulation – skip 0, skip 4 and skip 15 (opposite stimulation) with stimulation current of 5mA. Inverse models for each stimulation pattern and electrode size model was created with the appropriate NF (and regularization hyperparameter) by choosing a value around the L region in the L – curve [69].

3. Results

The influence of the noise figure on the reconstructed images was tested by evaluating the reconstruction with the help of the GREIT's figures of merit. Additionally, an algorithm designed to detect aortic pixels was employed and its results evaluated for 20 different noise figure reconstructions. In a second simulation, 10 different electrode sizes were tested to see which one produced better reconstructions for three different stimulation patterns. The reconstructions were again evaluated with the FOM defined by GREIT.

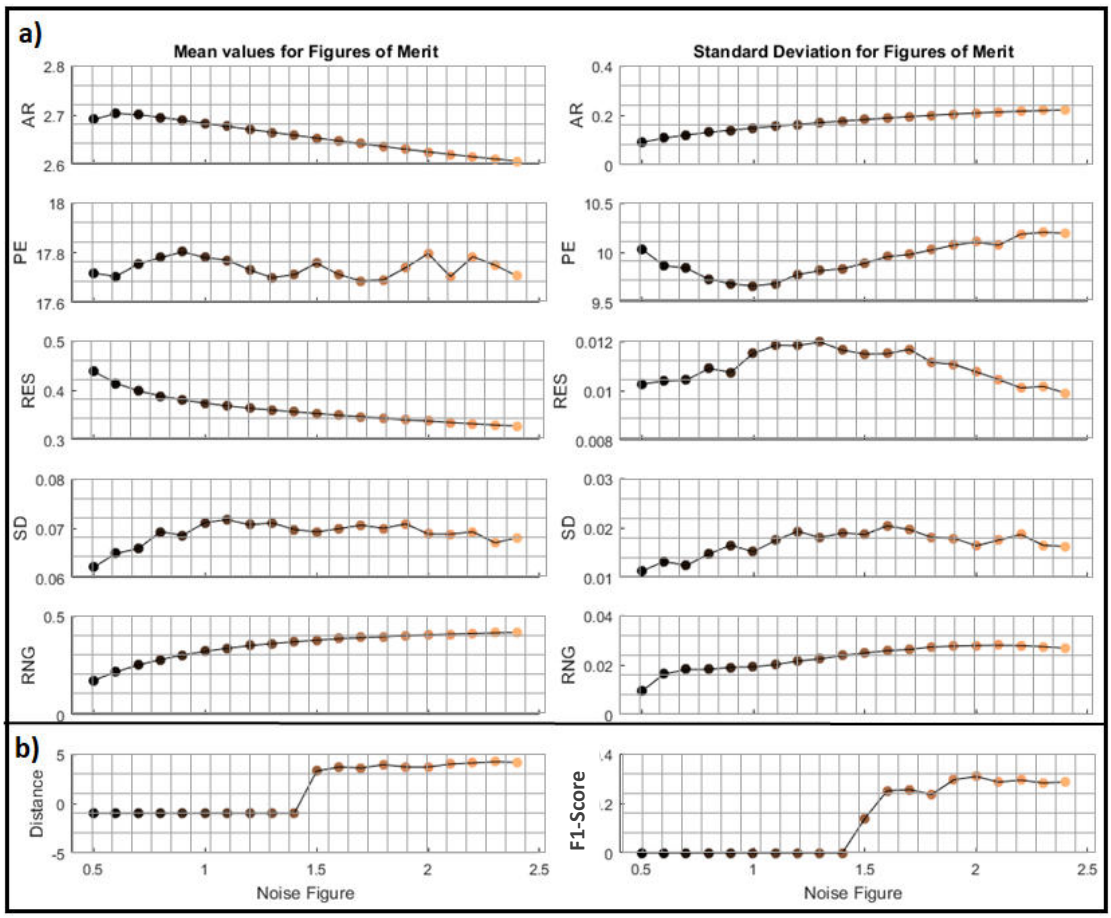

Figure 17. Summary of the noise figure tests results. a) mean values and standard deviation of figures of merit b) distance from the central pixel of the detected aortic region to the center of the CT contour and F2-scores. The results are color coded black to orange corresponding to NF.

3.1. Noise figure tests

The results of the noise figure tests could not highlight a single noise figure that performed best for the different FOM (Figure 17a). The AR showed almost linear behavior, where its standard deviation increased with increasing noise figure. Here the desired behavior is spatially uniform distribution of amplitude response which is most true for the low noise figure values (Figure 17) at σ_{AR}=0.1. The RNG also shows very similar behavior, where both standard deviation and mean value increase with increasing noise figure, thus suggesting that lower noise figures produce better images with RNG=0.18. The mean value for RES decreases monotonically for increasing noise figure and reaches 0.32% or 6.4mm. All other curves showed highly non-linear behavior with a number of local minima and maxima. The RES was most uniformly distributed for NF=2.4. The standard deviation and mean value of SD showed very similar performance. Both have their global minimum for NF=0.5 at SD=6.4% and σ_{SD}=1%, but for NF>1, the higher NF perform better, especially NF=2.3 and NF=2. The PE was the

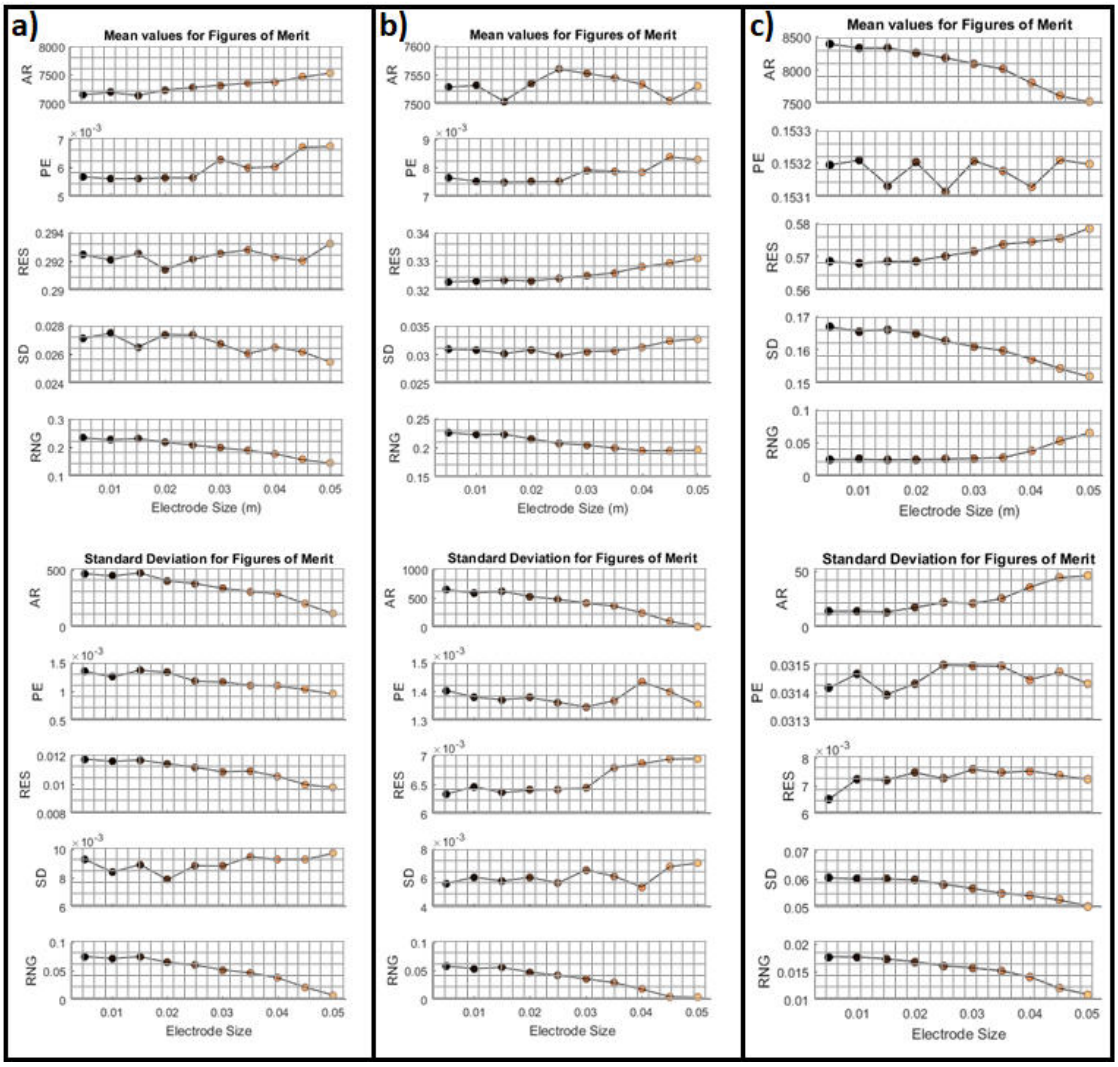

Figure 18. Summary of the electrode size tests results. Mean values and standard deviation of figures of merit for a) skip0 b) skip4 and c) skip15. The results are color coded black to orange corresponding to electrode size.

lowest for NF=1.6 and most uniform for NF=1, but both standard deviation and mean value had a local minimum that performed well at NF=2.1. To sum up, it seems like both low NF= 0.5-0.9 and high NF=1.9-2.4 performed well regarding AR and RNG, and PE, RES and SD respectively. In between, there were some noise figures that performed exceptionally well in one figure of merit, but failed to deliver in others (for example, NF=1.6 for PE).

3.2. Aortic search algorithm

The aortic search algorithm was able to discriminate aortic regions for NF>1.4. The minimum distance was achieved for both NF=1.5 and NF=1.7, but overall all NF>1.4 performed well finding an almost identical distance of between 3.2 and 4.2 pixels. The F1-score was at its global maximum at NF=2 and

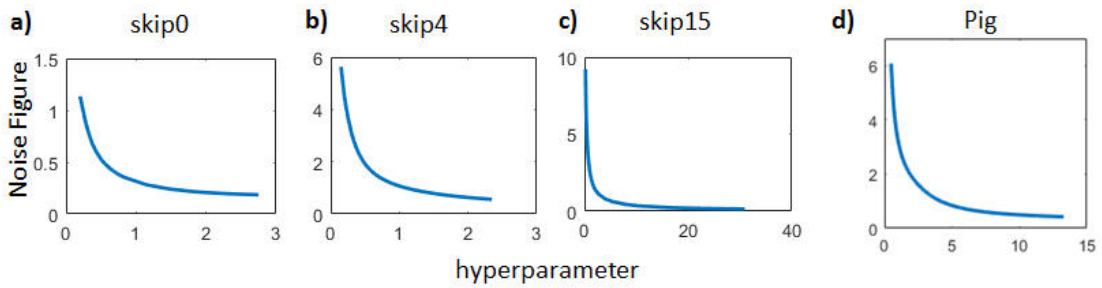

Figure 19. L-curves of the electrode size simulation setup for different stimulation patterns a) skip0 b) skip4 c) skip15 and d) for the reconstruction model of one representative pig

reached $F1$=0.3. For all NF<1.5, the aortic region could not be identified at the constant threshold of th=0.05. Intermediate results and masks of the aortic search algorithm can be seen in Figure 15. The second row of images shows areas with high power at cardiac frequency which would sign for structures and phenomena that are modulated by cardiac activity. The other images in the sets show the mask that was computed with the aortic search algorithm for lungs (top row), heart (second to bottom row), and aorta (bottom row). The masks of the lungs and the aorta are also compared with their contours that were segmented from the CT scans. The tidal volume image is produced by only two breathing cycles, but closer inspection of the PSD shows that for higher noise figure, the lung ROI produced by tidal volume and additionally by PSD are almost identical, while for lower NF they differ much more. With increasing noise figure, the lungs started to separate from a structure that was overshadowing the aorta and thus making it invisible for the algorithm. For NF>1.8 the overshadowing structure was separated completely, which resulted in a noticeable bump in the F1-score. With increasing NF, the lungs also started moving more ventrally, partly because they were separating from the overshadowing structure. The edges of the structures that were visible in the PSD image became sharper with increasing NF. The heart ROI did not change much with the NF compared to aortic ROI and lung ROI.

3.3. Influence of the electrode size

The influence of the size of the electrodes on the reconstructed image was simulated and evaluated based on the figures of merit for three different stimulation patterns, which will be presented separately.

Adjacent stimulation – skip0

The amplitude response was most uniform for the biggest electrodes – r=0.05 (Figure 18 a)). Similarly, all other figures of merit, except SD, showed most uniform behavior for r=0.05. The ringing and shape deformation was also the least pronounced for the biggest electrode size. The best resolution, least position error and most uniformly distributed SD was achieved for electrode size r=0.02. Overall the largest electrode size seems like the best choice for adjacent stimulation.

45° stimulation – skip4

Here the largest electrode size again exhibited the most uniform amplitude response, position error, ringing and also least amount of ringing. However, the best resolution was achieved with the smallest electrodes, while both PE and SD was lowest for r=0.015 followed by r=0.025. r=0.015 and 0.025 took 2nd and 3rd place in SD and PE uniformity and r=0.015 was also second in RES uniformity, just after the smallest electrode size. To sum up, it is harder to pick a single best electrode for this stimulation pattern, compared to adjacent stimulation, but still, overall the largest electrode size performed the best.

Opposite stimulation – skip15

In the opposite stimulation pattern, the smallest electrode size showed the most uniform AR and RES, and 2nd most uniform PE. It also showed the best resolution and least ringing. The PE curves were highly non-linear in both mean value and standard deviation, where mean value showed 5 local minima. The largest electrodes showed the least SD and most uniform SD and RNG. Overall, the smallest electrodes produced the best images in contrast to the other two stimulation patterns tested.

Overall adjacent stimulation and 45° stimulation showed very similar results for most FOM, but the 45° stimulation noticeably outperformed the adjacent stimulation in RES and SD consistency. Overall the results from the opposite stimulation were worst compared to the other alternatives, but it achieved very good scores in RNG both mean and standard deviation and also mean SD.

4. Discussion

In this chapter, the influence of the noise figure reconstruction parameter on the image quality was measured in simulation and in-vivo. The results showed that the optimal noise figure for the measurement setup is NF=1.8. Also in simulation, the effect of the electrode size was measured for different stimulation patterns, where the largest electrode size with r=0.05m outperformed the others based on FOM.

The effect of increasing the resolution of the reconstruction by increasing the NF is visible in Figure 15. For NF>1.8 the lung can already be resolved from another unknown structure overshadowing the aorta, possibly the diaphragm, and they do not appear as a single blob. This also enables the differentiation of the aorta which is located very close to the lungs. For lower resolution, the two structures (or rather three) will be smeared together. This effect was not surprising, because by increasing the noise figure the ration of SNR of the voltage signal to SNR of the image will be increased, thus effectively reducing noise in the image domain.

The region associated with the lungs moved more ventrally with increasing NF (Figure 15). However, in another work accepted for publishing in the 19th International Conference on Biomedical

Applications of Electrical Impedance Tomography, we found out that the center of ventilation moves dorsally with increasing NF. This dissonance in the findings can be explained by the fact, that only the biggest structure was associated with the lung region of interest in the tidal volume image. Consequently, it is possible that parts of the image that belongs to the lung region are excluded. Furthermore, for the calculation of the center of ventilation every pixel is weighted in with its intensity, while the goal of this analysis was to select one connected pixel region showing the highest intensity.

The results of the NF tests were further validated with an L-curve approach (Figure 19d), which is a method where the regularization hyperparameter is plotted versus the respective NF and the resulting curve usually has the form of the letter L or $y = \frac{1}{a*x}$. This heuristic approach selects the best NF by minimizing its distance from the 'knee' of the L-curve and 1.5<NF<1.9 was shown to be right at the 'knee'. However, one key limitation of the NF approach is that different measurement setups – different stimulation patterns, different measurement patterns, different boundary shapes – will not perform similarly under the same noise figure [69].

Among all FOM the PE showed the highest coefficient of variation reaching values of 0.57 for NF=0.5 (figure 17). The PE measures the distance between the center of gravity of the reconstructed image and the real position of the center of the training target. Meanwhile, the aortic search algorithm detected pixels, the center of which was no more than 4.2px away from the center of the aorta segmented from the CT images. One possible explanation could be that the PE is randomly distributed and when a number of spherical inhomogeneities are reconstructed, the resulting cluster is the same due to the randomness of the distribution of the position error.

The results of the electrode size test were surprising at first because it was thought that the larger electrodes would irradiate broader regions and that would result in more shape deformation, lower resolution and higher position error (the lower resolution part turned out to be true). However, if the image of the potential line distribution is imagined (Chapter I Figure 9), it can be seen that smaller electrodes would miss on some of the information. Some change in potential lines distribution would not even be sensed if there is no sensor at the boundary to measure the change. Also, the position and shape of the conductivity change would be harder to predict accurately, because the sensors would not be probing often enough in the space domain. Thus, from these results, it can be concluded, that if the number of electrodes is given, the larger electrodes would outperform the smaller ones and thus they should be preferred in future studies if the choice is on the table. However, the figures of merit behavior show more non-linear behavior when the input parameter is the size of the electrodes compared to the NF, therefore always choosing the biggest electrode might not be universally correct.

A serious drawback of this investigation is that the figures of merit give information about the quality of the reconstruction of a small spherical inhomogeneity. In reality, more complex shaped features would be of interest, especially in the domain of medical application. There was recent proposal to

move away from the spherical inhomogeneity in the training process and use medically relevant structures instead [75], therefore this method should be used in future work. However, the aortic search algorithm confirmed the results of the figures of merit tests for the hyperparameter selection investigation. Unfortunately, no real data was available for the electrode size investigation. As shown the hyperparameter has the power to heavily influence the results of an EIT reconstruction. For its selection, the noise figure method was used, however, Braun et al. [76] lately have shown that this method is not robust when it comes to comparing different systems. Consequently, the influence of the current findings is somewhat reduced.

III. Aorta detection with EIT and non-invasive blood pressure measurement

1. Motivation

As pointed out in chapter I, developing a non-invasive, cheap, continuous and reliable method for monitoring hemodynamic parameters such as stroke volume, BP or PWV at a key and hardly accessible cardiovascular landmarks such as the aorta, could be of great benefit in the clinical practice of cardiovascular diseases. Such system could greatly increase the diagnostics and monitoring power in intensive care units, by introducing beat by beat measurements of hemodynamic parameters and thus improve the outcome of patients. Furthermore, costs of hospitalization could sink and more importantly, contradictory practices such as catheterization would be replaced by this non-invasive method. [77].

EIT seems to fulfill non-invasiveness because at the frequencies of the technology of around 150kHz and at the electric current levels of around 5mA, there are no harmful effects on the human body [78]. In 2010 Adler et al. called adjacent stimulation harmful, but they did not mean it literally[5] [79]. EIT can also be categorized as cheap, with the price of modern devices of around 5500,- EUR [80], negligible compared to the price of advanced blood pressure monitors. With a sampling rate of 50Hz, beat by beat monitoring of hemodynamic parameters should be possible, but when accurate measures of PTT are needed, it is still not proven that EIT is up to the challenge. Reliability is another issue. As shown in the previous chapter, EIT image reconstruction is a complicated process, subject to a lot of different input parameters and measurement settings that have the potential to heavily influence the result of the reconstruction.

Detection of aortic pixels in EIT images is the first crucial step towards non-invasive monitoring of central hemodynamics. One way to easily detect those pixels is through injecting of a contrast bolus. It was first shown by Sola [34] and later by Thürk et al. [81] and Wodack et al [70], that the aortic pixel can reliably be detected by injecting a saline bolus and searching for pixels that exhibit a prominent change in conductivity. Injecting a solution into the human body is an invasive procedure, therefore an autonomous detection of aortic pixels without the use of contrast is of paramount importance in order to transfer the technology into the clinical praxis. However, the contrast solution and the pixels detected by that method serves a very important task of providing a ground truth for validation of algorithms

[5] Adjacent stimulation is one of the popular choices of stimulation pattern among commercial EIT devices. See Chapter I, Section 2.2. Table 1. In their paper, Adler et al. suggested that adjacent stimulation is not the best choice for stimulation pattern, because phenomena of interest usually lie deep within the body, while adjacent stimulation is most sensitive to superficial regions, thus reducing the diagnostic power of EIT. See Chapter I Section 2.3.1.

designed to detect the aortic region of interest. This type of ground truth has the advantage over more traditional types – a CT contours of the aorta, for example – because the detection happens within the scope of the same technology, while CT equipment is bulky and might require transportation and relocation of the patient in addition to making the measurements from the different modalities at separate times instances.

In 2010, Josep Solà et al. showed for the first time the feasibility of EIT as a means for central blood pressure monitoring [34]. They developed an algorithm that localizes the descending thoracic aorta based on ECG triggered pulse arrival time (PAT) and validated its location through injection of contrast saline solution. The PAT, which is a surrogate parameter for blood pressure under certain conditions, calculated on those functional EIT pixels showed high correlation with mean aortic blood pressure (-0.967 ($P<10^{-5}$)). The study, however, was carried out on a single animal and there has not been any continuation on the subject in the scientific literature, to the best knowledge of the author of this work.

PWV is closely tied to PAT through Eq. (30) and is considered the gold standard methodology for determining arterial stiffness [82].

$$PWV = \frac{d}{PAT} \tag{30}$$

Where d is the arterial distance from the heart to the measurement site. Moreover, in central elastic arteries such as the aorta, PWV has been shown to strongly correlate with arterial blood pressure. Since arterial stiffness changes occur over long periods of time, PWV is a suitable parameter for interim blood pressure monitoring.

The aim of this experiment was to find out, whether changes in PWV and PAT measured with EIT correlate with blood pressure changes and to confirm the findings of Solà et al.

2. Methods

2.1. Study protocol

Animal data

The pigs that were used in this work, were part of a larger project including 31 anesthetized and mechanically ventilated animals. The animal study protocol was approved by an ethics commission (approval no. 70/11). The animals were ventilated in pressure-controlled mode with a positive end-expiratory pressure of 5 cmH_2O (Zeus®; Drägermedical, Lübeck, Germany) and for anesthesia were continuously infused with fentanyl (10µg/kg/h) and were receiving an end-expiratory inhalation of 2.5% sevoflurane. The EIT (Pioneer Set by Swisstom AG, Landquart, Switzerland) signal was recorded with

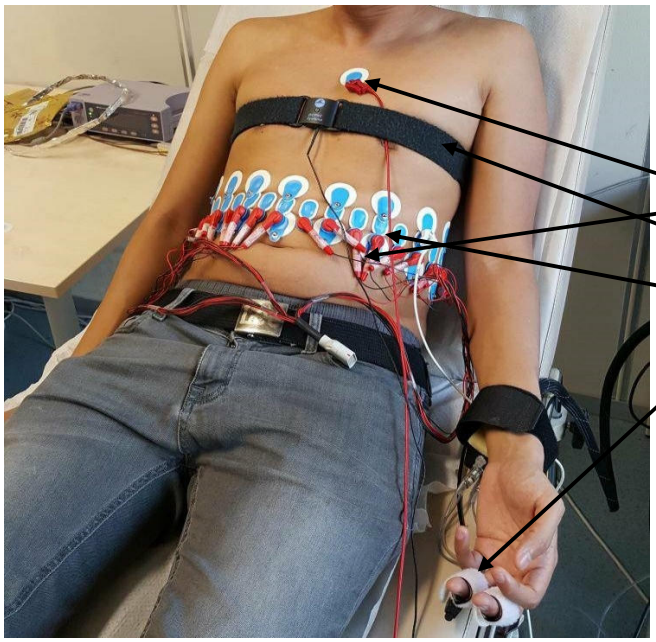

Figure 20. Measurement setup for the aortic detection and non-invasive blood pressure measurement experiment. The measured signals included:

- **Electrocardiogram**
- **Respiration belt**
- **Electrical Impedance Tomography (1x32 electrodes & 2x16 electrodes)**
- **Non-invasive blood pressure**

a custom belt with 32 electrodes and a sampling rate of 36 frames/s. Three belts recording EIT were placed at various heights around the thorax – between ribs: 9 and 10-low, 7 and 8 – middle, and 5 and 6 – high. At the beginning of the study protocol, a 10 ml saline bolus of 20% NaCl was injected into the aortic arch in order to increase conductivity in the aorta. EIT data was recorded for two minutes of respiration and 30s of apnea for each belt location. After the EIT data was collected, CT scans were performed for each animal.

Human data

The EIT signal and supporting signals were measured on 5 healthy male subjects age 25-27 in Fowler's position (Figure 20). The EIT measurement device (Pioneer Set by Swisstom AG, Landquart, Switzerland) used 32 individual electrodes (Ag/AgCl disposable ECG gel electrodes) located in a transverse plane around 5cm above the umbilicus. The stimulation current had an amplitude of 3 mA, 150 kHz frequency and was injected in a rotating sequence between pairs of electrodes with a gap of four idle electrodes between injecting ones. Voltage measurements from injecting, their immediate neighbors and idle electrodes were ignored, adding up to a total of eight non-sensing electrodes per stimulation. The EIT sampling rate was 50.8626 Hz. The respiration signal was measured with the help of a motion sensor. For the electrocardiogram, three electrodes (Ag/AgCl disposable ECG gel electrodes) in custom derivation around the heart were used and connected to the BIOPAC device and the blood pressure was measured with a Portapres (Finapres Medical Systems B.V., Enschede, The Netherlands) blood pressure device with hydrostatic compensation. The last channel was used for synchronization of both devices, recording EIT measurement and the supporting physiological data, respectively. All supporting signals were passed to an MP36U-W (BIOPAC Systems, Inc., Goleta, California, USA) general purpose measurement device.

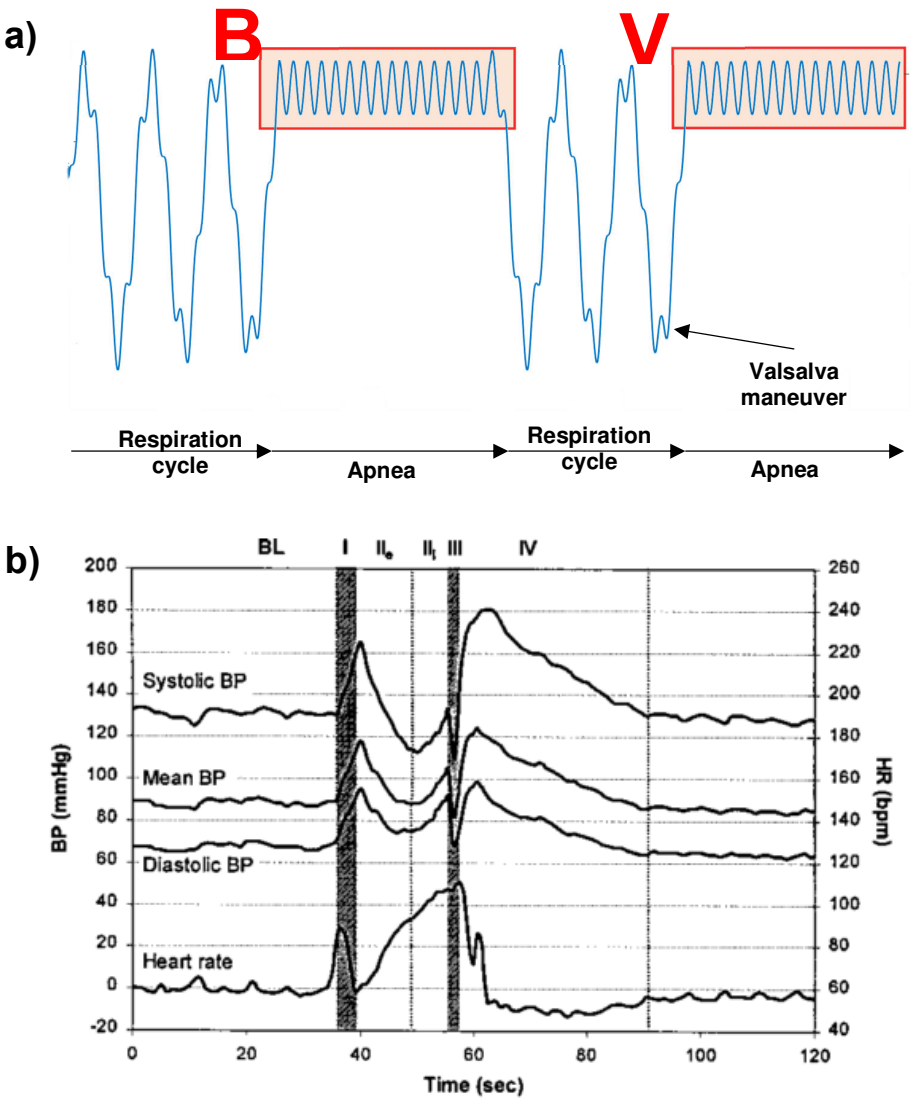

Figure 21. a) Schematic drawing of the measurement protocol. Both baseline (B) and Valsalva (V) measurement start with a few respiration cycles followed by apnea. b) time course of the blood pressure and heart rate during Valsalva maneuver. Adopted from [83]

The dataset for each subject included a baseline and Valsalva measurements, except subject 1 who was part of the pilot experiment (Figure 21a). First, for the baseline measurement, the subjects were asked to cease breathing in expiration for as long as they could. After some reasonable recovery time (dependent on the subjects preference, no less than 1 min), the subjects were asked to perform a Valsalva maneuver and cease breathing in expiration for as long as they could immediately after, for the second measurement dataset. The goal of the Valsalva maneuver is to temporary induce a change in blood pressure trough artificially closing one's airways during attempted expiration. Datasets from subject 1 do not include measurements after Valsalva maneuver.

During the Valsalva maneuver, the intrathoracic pressure raises due to the forced exhalation attempt with closed airways [83]. The first noticeable effect is the rise in blood pressure (Figure 21b I) due to

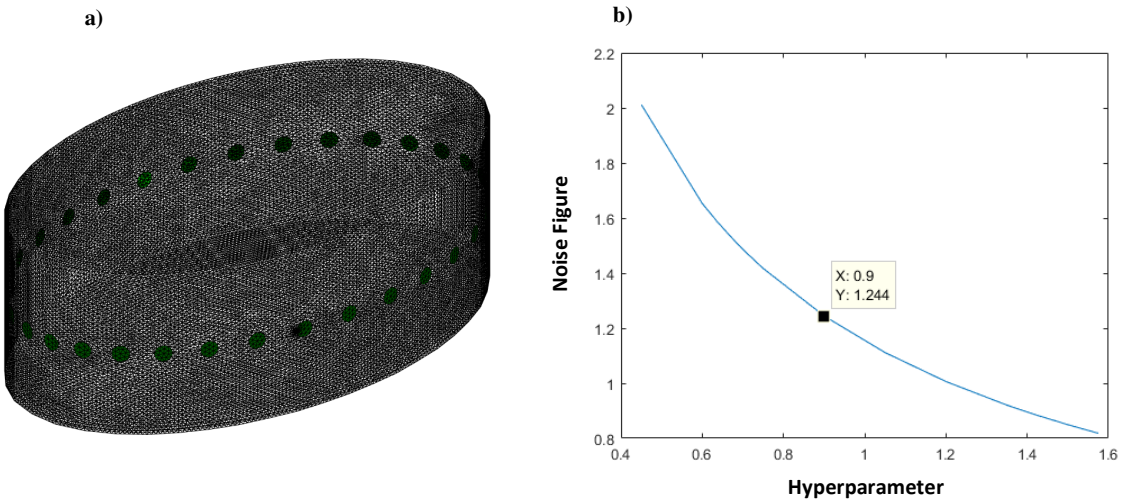

Figure 22. a) FEM with elliptic geometry and electrodes (green circles) b) L-curve for the system with elliptic geometry and skip4 stimulation pattern

blood being forced out of the pulmonary circulation into the left atrium, thus increasing stroke volume. However, after a few seconds, the venous blood volume returned to the right atrium decreases, because of the increased intrathoracic pressure during the maneuver. Consequently, the stoke volume of the heart decreases and thus blood pressure decreases as well (Figure 20b II). As a reaction to the reduced stroke volume, the blood vessels constrict and a rise in blood pressure is observed (Figure 20b III). This compensatory effect of constricting the vessels persist for around 30s after the end of the Valsalva maneuver and induces the rise of blood pressure which we will be trying to detect with EIT trough PAT measurement.

All participants in the experiment have been informed about potential dangers and have signed a declaration of consent.

Table 2. Summary of participants in the in-vivo experiment

Subject No	Height (cm)	Weight (kg)	Age (years)
1	185	72	26
2	177	66	25
3	195	90	26
4	177	80	27
5	187	75	27

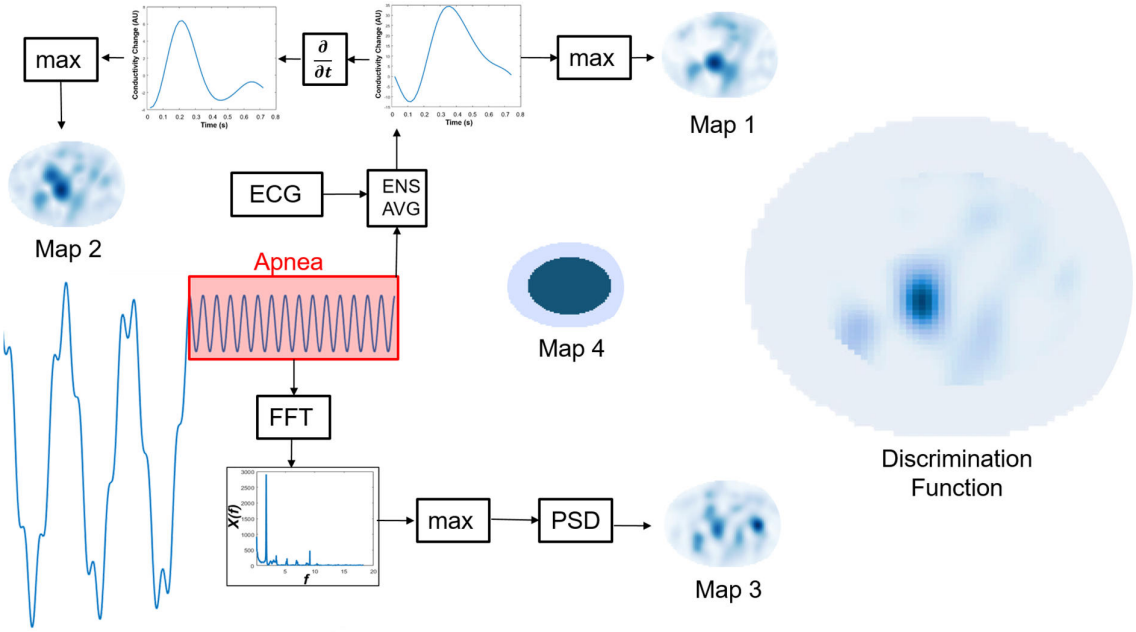

Figure 23. The discrimination function is a map that holds a value for each pixel. It is the product if the multiplication of four other maps shown in the image.

2.2. Image reconstruction

The first step in solving the ill-conditioned non-linear inverse problem of EIT is to build a finite element model (FEM), which is then used to solve the forward problem in order to acquire the Jacobian matrix of the system. To this end, a generic FEM (Figure 22a) was built with the help of MATLAB, the EIDORS framework and NETGEN [73]. A simple elliptic geometry was chosen with a ratio of the main axes of 1.6446:1, corresponding to the mean ratio of lateral to the posterior-anteroposterior radius in males [84].

Next, the inverse model was built that is used for image reconstruction. The GREIT reconstruction algorithm [61] was set up to reconstruct images on a 64x64 pixels rectangular grid. The training of the algorithm was performed by placing 1000 uniformly distributed targets with a radius of 2% of the longer axis of the ellipse. The weighting radius was set to 0.2 and the noise performance of the algorithm was controlled by a noise figure criterion set to 1.2 based on the L-curve of the system (Figure 22b).

The animal FEM (figure 14a) was build based on the segmented contours of the thorax from the CT images that were available. The inverse model was build based on the considerations from the previous chapter, the reader is referred there for more information on the FEM and inverse animal models.

The raw EIT voltage signal and the supporting signals were then cut in order to align them with the instances of synchronization. The reference point around which the non-linear system was linearized for reconstruction was chosen as the time series of the mean measured voltage from all sensing

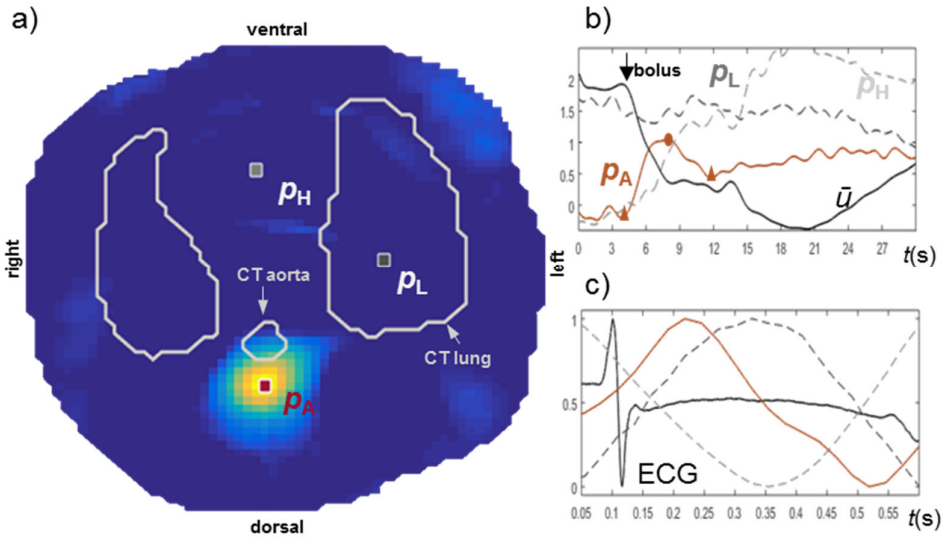

Figure 24. a) the map created by the peak prominence method with anatomical contours form CT and selected pixels of interest. b) time course of selected signals p_A – aortic pixel, p_L –lung pixel, p_H- heart pixel and $\bar{u}$- averaged EIT signal c) averaged cardiac components and ECG. Adopted from [81]

electrodes.

2.3. Signal processing and discrimination function

Initially, the respiration signal was analyzed to detect the apnea region (Figure 21) and all other signals were cut according to the start and end time instance of apnea. Because there was no respiration signal for the animal data, the apnea region was detected by analyzing the EIT signal. Consequently, the time series of conductivity change of each pixel was filtered with a finite impulse response 'brick wall' bandpass filter of 200th order with cutoff frequencies tuned at 0.5 Hz and 6 Hz, in order to get rid of sensor drift when present and high-frequency noise. R-peaks in ECG signals were detected and the mean cardiac frequency calculated, which was then used to compute a power spectral density map of the system through Welch`s method in the range of 75% to 150% of the cardiac frequency.

$$E_s(f) = \int_{0.75f_c}^{1.5f_c} |X(f)^2|\, df \tag{31}$$

This map represents regions that are subjected to cardiac activity and is later used as a part of a discrimination function that localizes the aorta.

The detected R-peaks served as trigger events, representing the genesis of the blood pressure wave. Pre-ejection period is ignored because it is assumed to be fairly constant between heart cycles and the goal of the experiment was to detect blood pressure changes, not absolute values of PWV. The time series of each pixel in the reconstructed image was then cut into segments representing periods between consecutive R-peaks. For pixels that are part of perfused regions, those segments would represent the arrival of the blood pressure pulse. Consequently, ensemble average [85] technique was applied

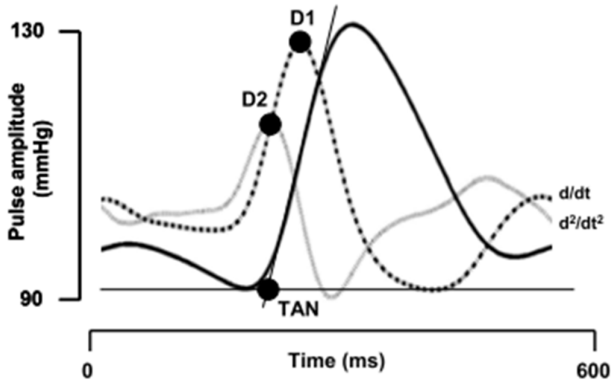

Figure 25. PAT detection. Tangent line fit in the point of maximum change of the blood pressure wave. The intersection of the tangent line with the line of minimum value of the pressure wave is considered the FOOT of the wave. Adopted from [18]

resulting in one representative blood pressure pulse for each pixel. Ensemble averaging is expected to improve the signal to noise ratio of blood pressure wave by a factor of $\sqrt{N}$ for averaging of N pulses [21] and enable PAT calculation for the otherwise noisy EIT signal (Figure 27a&b).

Finally, the discrimination function (Figure 23) that localizes the aorta was comprised of three individual matrices holding a characterizing value for each image pixel. First, as already mentioned the power spectral density map that represents cardiac activity was used. The second function, holds the value of the maximum of the ensemble averaged blood pressure wave for each pixel, while the last one holds the value of the maximum of the first derivative of the ensemble averaged blood pressure wave. Additionally, an annulus shaped region of edge pixels was penalized, because as discussed in Chapter I EIT is most sensitive in those superficial regions and often artifacts occur at the edges of the image. A threshold criterion was applied to the discrimination function discarding all pixels that hold a value below 50% of the maximum.

2.4. Peak prominence detection for validation of aortic region

In order to validate the aortic region detected by the discrimination function, a peak prominence method was used. This method was applied to the animal data because it requires the injection of a saline-contrast solution which was part of the animal study protocol. The peak prominence method creates a map (Figure 24a) similar to the ones comprising the discrimination function, but the information coded in each pixel represents a local maximum in conductivity change relative to its neighboring minima – a prominence. To this end, the signal of each pixel is band pass filtered (200^{th} order, finite impulse response, cut-off 0.05Hz and 0.5Hz) and then a single most prominent peak is detected in a manually selected time window (Figure 24b).

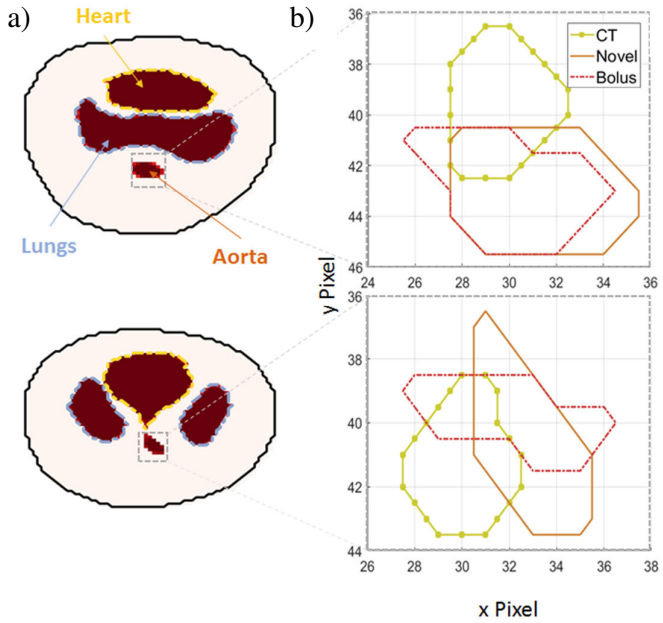

c)

	Animal 1	Animal 2
F-1 Score CT	0.2414	0.25
F-1 Score Bolus	0.8125	0.5128
Distance CT (pixels)	1.84	1.2
Distance Bolus (pixels)	0	0.45

Figure 26. Validation of the aortic search algorithm. a) Detected cardiovascular structures for the two pigs analyzed b) aortic contours detected with three different methods: discrimination function, CT and peak prominence method c) F1-score validation metrics

2.5. PAT detection

Finally, the PAT for all pixels were calculated by using the maximum of the slope of the blood pressure pulse for each pixel and fitting a tangent line at this point (Figure 25). The intersection of the tangent line with the line of the minimum value of the pressure wave is considered the foot of the pressure wave [86].

The PWV was calculated through eq. 27, where the distance between the heart and the measurement site was acquired based on a linear model that estimates the length of the aorta between the subclavian and renal arteries in males as a function of their height. [87] An additional correction of 2.16% of body height was added to account for the distance between heart and subclavian artery and renal artery and the measuring plane which was just above the level of the umbilicus.

$$d = -26.253 + 1.529 \cdot height \tag{32}$$

3. Results

3.1. Discrimination function and validation

Aortic pixels in EIT images were detected with the help of a discrimination function in human and animal data. The constituent maps of the discrimination function are presented in Figure 23 for a human subject. Different maps highlight different regions, but their combinations successfully detected the

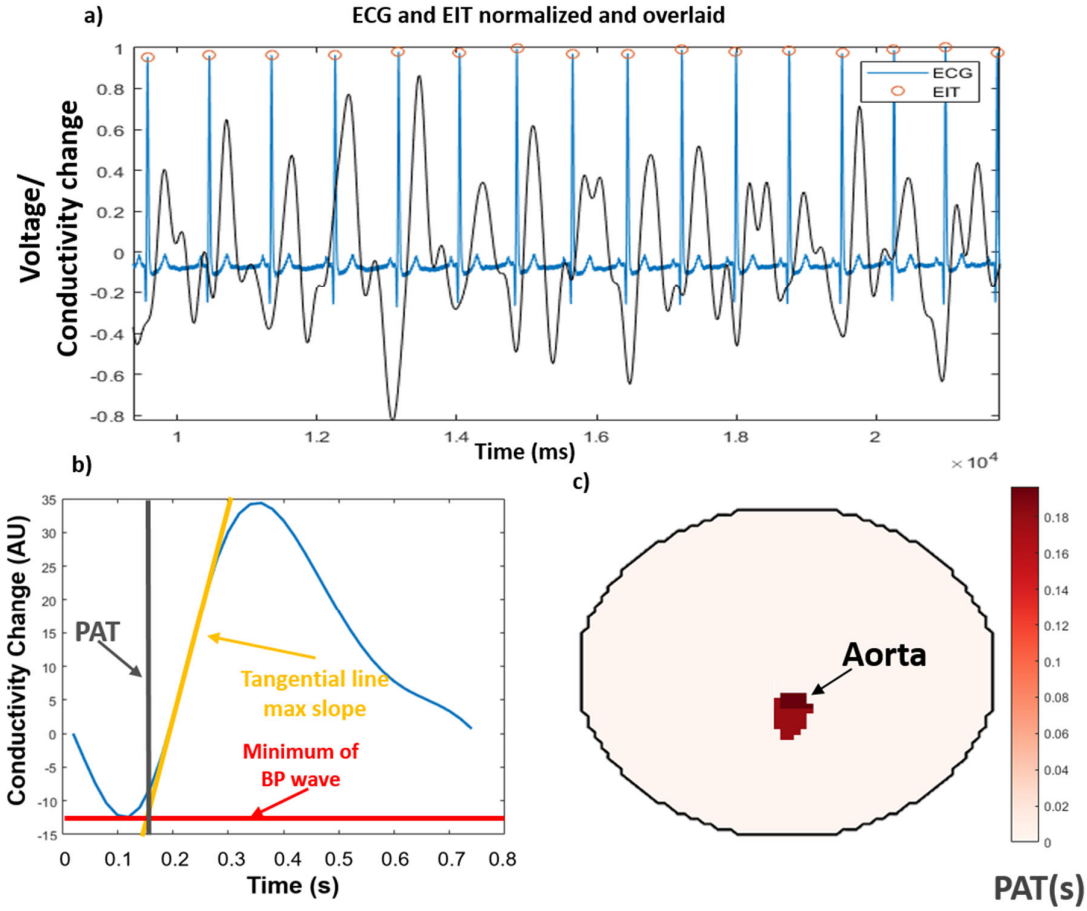

Figure 27. Effects of ensemble averaging a) Arbitrary part of the ECG and EIT signals overlaid for subject 2, first measurement of the protocol. b) Averaged wave of the aortic region over all heart cycles during the apnea period with tangent line and detected foot of the wave for subject 2, first measurement of the protocol. b) Functional aortic pixels detected by the discrimination function and color coding for PAT for subject 2, first measurement of the protocol.

aortic region in human and animal subjects. It can be seen that the maps of both maximum slope and maximum value have their maximum around the detected aortic region, but the map of maximum value also has another strong neighboring region. The PSD map has its maximum on the right of the image (anatomical left), but the aortic region also shows high power spectral density at cardiac frequencies.

The validation of the aortic region detected by the discrimination function happened on basis of CT scans and injection of contrast solution within the animal data. Figure 26b shows the contours of the detected regions with the three different methods. A significant overlap can be seen between the different modalities - F1-score between CT and EIT 0.2414 and 0.25 (Figure 26c) and even better overlap when validating within the same modality - EIT – Bolus, and discrimination function F1-score 0.8125 and 0.5128.

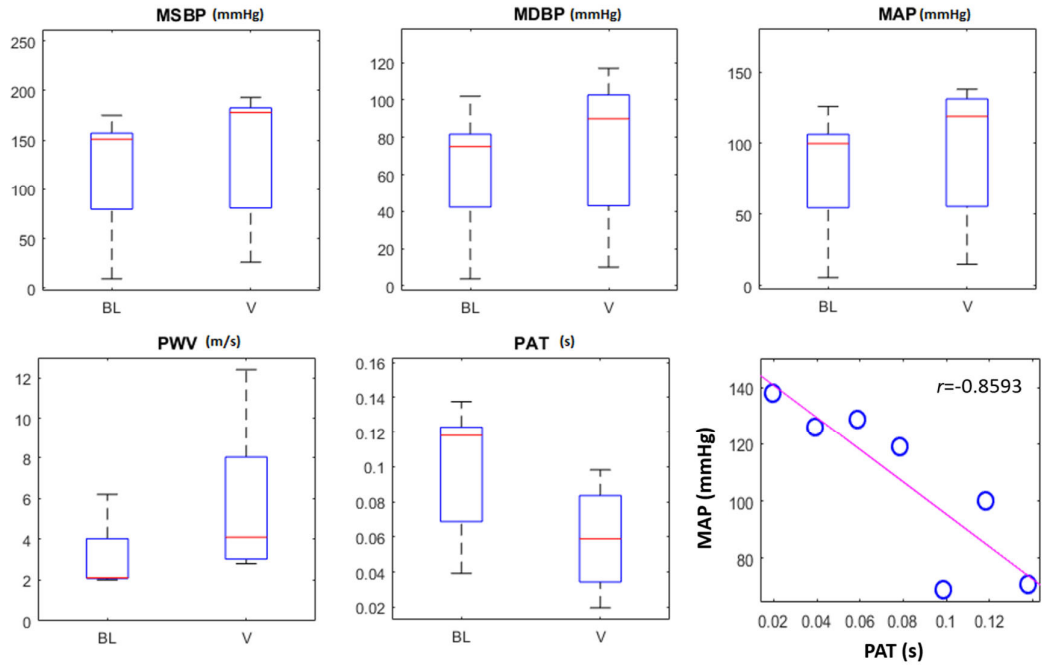

Figure 28. Boxplots summarizing the results of the non-invasive blood pressure measurement. BL stands for the baseline measurement, V stands for the measurement after Valsalva maneuver. All MSBP, MDBP, MAP and PWV increased during the Valsalva measurement, while PAT decreased. A correlation coefficient of r=-0.8593 is measured between MAP and PAT.

3.2. Ensemble average

A time window of normalized EIT and ECG signals are shown in Figure 27. Even though the EIT signal is bandpass filtered to get rid of high-frequency noise, the onset of the pressure wave cannot be easily pinned to a point in time and thus rendering PAT detection impossible. Applying ensemble averaging, however, creates a representative BP wave for each pixel that has much higher SNR compared to each and every single wave between R peaks. The ensemble averaged wave is presented in Figure 27b. Different morphological landmarks of a typical BP wave can be seen, which enabled PAT measurement. In all cases, the calculated PAT for individual pixels across the whole aortic region was rarely uniform (Figure 27c).

3.3. PAT and blood pressure measurement

All subjects exhibited an increase in blood pressure after the Valsalva maneuver (Table 3). Systolic blood pressure increased more than diastolic. Respectively, a decrease in PAT was observed in all subjects as a response of the increased BP in the second measurement. The estimated PWVs were a little bit under the physiological range (4-10 m/s) with the exception of subject 4, who exhibited a PWV of 12.4 m/s for the second measurement. The blood pressure values of subject 5 were extremely low and a closer inspection of the physiological signals showed that there was an equipment malfunction

Table 3. Summary of the results of PAT detection.

Subject	*Measurement*	*PAT (s)*	*d (mm)*	*PWV (m/s)*	*MSBP (mmHg)*	*MD BP (mmHg)*	*MAP (mmHg)*
2	B	0.118	244	2.1	151	75	100
	V	0.059	244	4.1	193	98	129
	V	0.0786	244	3.1	178	90	119
3	B	0.1376	272	2.0	103	55	71
	V	0.0983	272	2.8	99	54	69
4	B	0.0393	244	6.2	175	102	126
	V	0.0197	244	12.4	179	117	138
5	B	0.0786	260	3.3	9.3	3.8	5.63
	V	0.0393	260	6.6	26	10	15

during this measurement. An overall trend was observed between BP and PWV/PAT for all subjects. An increase in BP leads to an increase in PWV or a decrease in PAT. A boxplot summary can be seen in figure 28. A strong negative linear correlation was observed between PAT and MAP (r=-0.8593). Subject 5 was excluded from the evaluation, because of the instrument malfunction and invalid BP values.

4. Discussion

In this chapter, a novel algorithm for autonomous detection of aortic pixels was introduced. The algorithm was validated on animal data versus a ground truth of computed tomography scans and intramodaly versus the aortic region detected by a peak prominence method after injection of saline bolus. The algorithm was then applied on the EIT measurement of 4 healthy volunteers and the time signal of the aortic pixels was analyzed to detect PAT. A high correlation between PAT and MAP was achieved (r=-0.8593).

The pilot measurement with subject 1 included two different protocols. The subject was asked to hold his breath in expiration and then in inspiration for the two protocols respectively. It was found out that the aortic region is more easily visible in expiration and this is the protocol that was used for the other subjects as well. The better sensitivity of EIT to the aortic region in expiration can be explained with the fact, that the reconstruction settings used assumed homogenously distributed background conductivity, which is a good approximation only when the lungs are empty. In inspiration, the air filled lungs have much lower conductivity than the surrounding tissue and violate the assumption. Grychtol and Adler [88] reported how the reconstructed EIT image change when the conductivity of the system deviates from the assumption. If there is ground truth available, in the form of CT scans or saline bolus

that helps to identify structures in EIT images, the respective regions should be weighted in the FEM for best results and most uniform AR.

The EIT measurement requires the application of 32 electrodes that preferably lie on a plane and are equally spaced from each other, which is a time consuming and cumbersome process. Therefore, an attempt to manufacture an EIT belt was made, similar to the one described by Oh et al. [89]. The design included a functional layer comprising 32 Ag/AgCl reusable ECG clip electrodes attached to an elastic tape with Velcro fastening mechanism. A tightening layer was then laid on top of the functional layer comprising of elastic tape and sponge that aimed to seal in the vertebra groove and improve electrode contact. Unfortunately, the contact impedance of the electrodes was too high and the belt could not be used for measurements.

The discrimination function is central to the detection of the aortic pixels in EIT. It can be seen from Figure 23 that the information contained in any of the three maps of the discrimination function would not be sufficient by itself to differentiate aortic pixels by simply applying a threshold criterion. The map representing the maximum of the pressure wave (Figure 23 bottom left) seems to be best suited for that job in the presented case, but that wasn't necessarily true for the other subjects. However, when combined into the discrimination function and by applying the threshold criterion of 50%, the aortic region was detected successfully for all subjects. Unfortunately, it was impossible to acquire a ground truth (CT scans, saline bolus etc.) for verification of the detection without exposing the subjects to additional harmful interventions.

The results of the pulse arrival time calculation (Table 3.) proved the expected outcome of the experiment. All subjects exhibited a change in PATs during the second measurement, which was conducted instantaneously after Valsalva maneuver intended to induce blood pressure change. The EIT derived PAT offers a unique advantage over state of the art PAT methods because it monitors impedance related pulses in the aorta while the existing methods are either invasive or use peripheral PAT as a surrogate for aortic PAT. However, PAT detection happens in multiples of the sampling period, therefore for shorter distances a huge change in PWV can be observed. 50Hz corresponds to 20ms temporal resolution, with the speed of the pressure wave of 5m/s the phase difference of a pulse measured at sites with a 10cm difference would not be detectable.

In chapter I, it was shown how the vertical sensitivity of EIT could affect the BP measurement (Figure 12). For PWV of $\boldsymbol{v} = 8\ m/s$ an pressure drop of $\Delta p = 15\ mmHg$ in the sensitivity region of EIT was estimated. Interestingly, for lower speeds and trough equation 21, the wavelength of the BP wave would decrease and consequently, the pressure drop across the sensitivity region would increase, thus making PAT harder to detect in patients with low vessel stiffness. Fortunately, the reverse effect would be observed for patients with high arterial and more often than not, they are the ones that would benefit the most from non-invasive and continuous monitoring of their BP.

The PAT and consequently PWV measurements of subject 4 stood out compared to the other subjects. This might be due to the fact that his body mass index was higher compared to the other participants and therefore had a larger abdominal diameter, which would increase the vertical sensitivity of EIT and lead to earlier detection of the pressure wave. Additionally, the results of subject 4 might be explained by the fact that he was the only tobacco smoker among the participants. Tobacco smoking has been shown to increase arterial stiffness and BP [90].

The need of ensemble averaging to increase SNR is also not discouraging. Given an averaged EIT sequence over 20 cardiac cycles, the PAT and consequently blood pressure could be measured every 20-30 s, without the need of inflating cuffs Although BP and PAT have a complicated non-linear elastic relationship, the dependency of the BP on the PAT has been shown to be adequately sufficient in order to exploit PAT for non-invasive BP measurements [21]. . In addition, the blood pressure measurement through the use of inflation of brachial cuffs may not yield accurate results, due to the stress associated with the measurement itself, especially during sleep. The EIT technology is not associated with any known sensations and might prove itself as the best choice for hemodynamic parameters monitoring in the future.

The results of the experiment prove the feasibility of EIT as a tool for monitoring of central blood pressure. Aortic functional pixels were successfully identified from a sequence of EIT images over several cardiac cycles. However, the results from the human subjects could not be validated due to lack of an alternative method for detection of aortic pixels. Nevertheless, the ensemble averaged wave coming from those functional pixels closely resembles the form of a blood pressure wave measured with state of the art devices, where even the dicrotic notch is clearly visible (Figure 27b).

A conference paper presenting the detection and validation of the aortic region on the animal data with the aortic search algorithm was submitted to the 19th International Conference on Biomedical Applications of Electrical Impedance Tomography and it was later accepted.

IV. 3 Dimensional Electrical Impedance Tomography

1. Motivation

Electrical Impedance Tomography is an imaging modality that reconstructs the impedance distribution within an object by injecting a high-frequency electrical current and measuring surface voltages. EIT is most commonly used to reconstruct 2D transverse slices of an object corresponding to the plane in which the electrodes are attached, but due to the diffusive nature of the electric current, the reconstructed image inherently carries information about the conductivities in a lens-shaped region above and below the plane (Figure 29). This lens-shaped region spans above and below the electrode plane up to a distance of ½ the diameter of the body under investigation [31]. Additionally, the off-plane sensitivity of 2D EIT depends on factors such as stimulation pattern, the contrast of underlying conductivities and geometry [91]. The projections of off plane conductivity changes on the imaging plane thus make the images very hard to interpret, especially in the deep regions where most physiological phenomena of interest happen and where the effect of off plane projections are the most pronounced.

The limitation of 2D EIT are well known, but still, it is the most commonly used modality in the scientific literature. Part of the reason for this circumstance is because historically speaking, it was computationally too expensive to reconstruct 3D images [92] and now the community sticks with it because it is well researched and it is shown to work for lung imaging. Another factor is the fact that most available EIT devices are designed for single plane measurement and don't allow for simple reconfiguration further impedes the transition to 3D EIT.

However, recently there have been efforts from different groups in the direction of 3D reconstruction. In 2016 Grychtol et al. published a paper on 3D EIT image reconstruction with GREIT [27], which extended the EIDORS library and proposed a unified approach for linearized reconstruction. Also in 2016 Wagenaar and Adler [26]wrote on the different stimulation patterns and electrode placements for two electrode planes. They used simulations, phantom measurements, and in-vivo lung imaging to determine the best measurement setup for 3D lung EIT, which was also the topic of Wagenaar's master thesis [93]. A new type of EIT focusing was proposed by Grychtol et al. in 2017, where the signal collected from two planes of electrodes is reconstructed on a single plane, resulting in conventional 2D EIT images, which has the advantage that already available algorithms can be used for the analysis of the images, but also brings the advantages of 3D EIT by limiting the projection of off-plane contrasts. A miniaturized 3D EIT system for tissue engineering was developed by Ahn et al. [94], which was one of the earliest attempts on 3D reconstruction using GREIT and the EIDORS framework. However, there are still a lot of unknowns regarding, reconstruction parameters, stimulation patterns and electrode

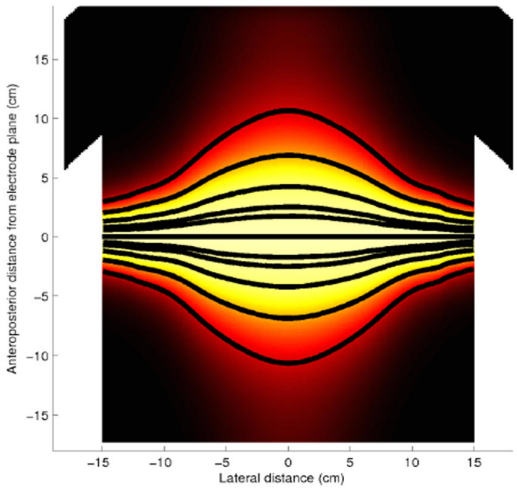

Figure 29. The vertical sensitivity of EIT. 2D EIT is sensitive to a lens shaped region ½ of the diameter of the body under investigation above and below the plane. Adopted from [34]

placements for monitoring the hemodynamics with EIT.

The aim of this experiment was to build a phantom tank and to attempt 3D EIT reconstruction of objects of varying sizes and conductivity in a first step and then extend to the reconstruction of physiological data and study the behavior of the cardiac EIT signal.

2. Methods

2.1. Water tank

A water tank with a cylindrical geometry was built in order to enable phantom measurements, comprising a plastic cylindrical tank and two rows of electrodes with 4cm vertical separation (Figure 30a). The plastic tank has a height of 70cm and 36cm diameter. For the electrodes, 64 stainless steel M4x16mm screws were used and arranged in two rings of 32 electrodes.

2.2. Phantom tank measurements

The phantom tank measurement datasets were recorded with the Swisstom Pioneer Set on the circular phantom tank with two rows of 16 equispaced electrodes. Seven sets of measurements were recorded with two different experimental conditions. First, adjacent stimulation with no gap between injecting electrodes was used and a conductivity of the tank solution of around $\sigma = 0.49\ \mathrm{S\ m^{-1}}$. The stimulation current had an amplitude of 3 mA, at 150 kHz. Voltage measurements from injecting, their immediate neighbors and idle electrodes were ignored. The EIT sampling rate was 30.5176 Hz. The electrodes were wired in a square pattern (Figure 30c) described by Grychtol et al. [27]. For the second setup,

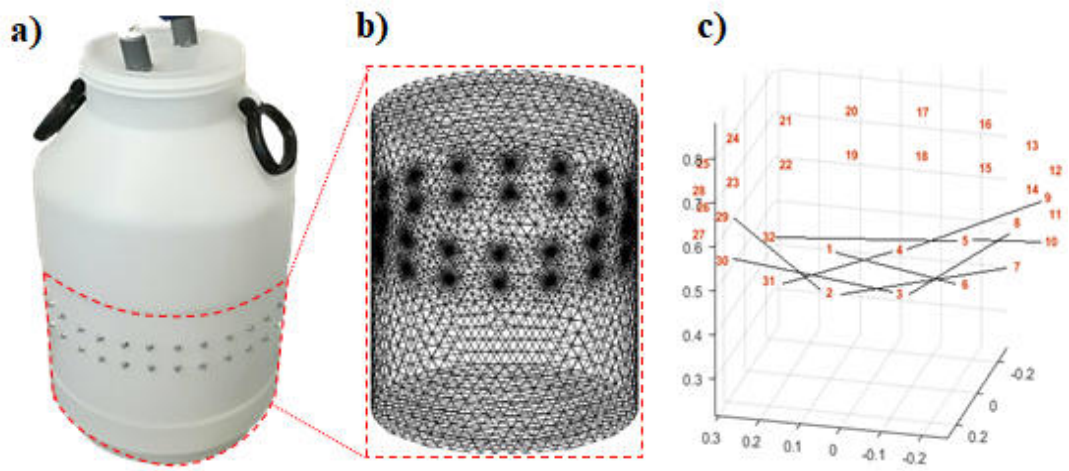

Figure 30. a) The phantom tank with two planes of 32 equispaced electrodes enabling both 3D and 2D EIT. b) The FEM of the phantom tank for 3D reconstruction c) Wiring of the electrodes of the 3D model. The two electrode rows are depicted with the wiring corresponding to square stimulation pattern. The black lines reflect the current injection pattern, whit a gap of 4 electrodes between injecting electrodes

the conductivity of the salt solution in the tank was increased to around $\sigma = 1.95\ \mathrm{S\ m^{-1}}$and the stimulation pattern was changed so the current was injected in a rotating sequence between pairs of electrodes with a gap of four idle electrodes between injecting ones (skip4). The water level in the tank reached 35 cm.

In the first experimental conditions ($\sigma = 0.49\ \mathrm{S\ m^{-1}}$, adjacent stimulation), the goal was to recreate the conductivity of the human abdominal cavity. To that end, the conductivities of various tissues present in the abdominal cavity were acquired from a database [108] and their area percentage estimated from a CT image of the human abdomen (Table 4). The estimated mean abdominal cavity conductivity of $\sigma = 0.49\ \mathrm{S\ m^{-1}}$ was recreated by dissolving sodium chloride salt in the water tank. The amount of salt needed to achieve that conductivity can be computed through the formula for molar conductivity.

$$\Lambda_o = \frac{\sigma}{c} \tag{33}$$

$$\rho = \frac{\sigma * M}{\Lambda_0} \tag{34}$$

Where Λ_o ($\Lambda_{0\,\mathrm{NaCl}} = 126.9\ S\ \mathrm{cm^2\ mol^{-1}}$) is the molar conductivity of salt, an intrinsic material property, c is the molar concentration of the salt solution, M ($M_{\mathrm{NaCl}} = 58.44\ \mathrm{g\ mol^{-1}}$) is the molar mass, ρ is the mass concentration.

Figure 31. The test objects used for the experiment. a) Empty glass soda bottle with diameter of 7cm b) Plastic tube with diameter of 2cm c) Metal file

The salt mass concentration that produced the desired conductivity value turned out to be $\rho = 2.25\ \mathrm{g\,l^{-1}}$ and the total amount of salt in the 35l tank was 79g. For the second experimental conditions, the mass concentration was increased to $\rho = 9\ \mathrm{g\,l^{-1}}$ resulting in a conductivity of the salt solution of $\sigma = 1.95\ \mathrm{S\,m^{-1}}$

The test objects (phantoms) included an empty soda bottle (7cm diameter), a plastic tube (2cm diameter) and a metal file (Figure 31), thus representing different geometries and conductivities. First, the soda bottle was immersed vertically in the center of the tank, followed by the hand of the experimenter and subsequently taken out in order to test the vertical sensitivity of the measurement system. Next, the soda bottle and the tube were immersed vertically and parallel to each other in order to test how different geometries with the same conductivity will be reconstructed. In the third measurement protocol, the plastic tube was first inserted vertically in the water tank and then its position was changed from the center to one side of the tank close to the electrodes and again to the other side through the middle thus testing the horizontal sensitivity of the measurement setup. Last, the plastic tube and the metal file were immersed vertically and in parallel in order to test how objects with similar geometry and different conductivity would be reconstructed.

Table 4. List of organ and tissue types in a cross-section of the human abdomen with area percentage and conductivity value [108]

Organ/Tissue	**Area percentage**	**Conductivity**
Liver	20	0.095369
Kidney	15	0.18038
Colon	20	0.25112
Duodenum	5	0.53804
Pancreas	10	0.53993
Muscle	20	0.37265
Fat	10	0.024513

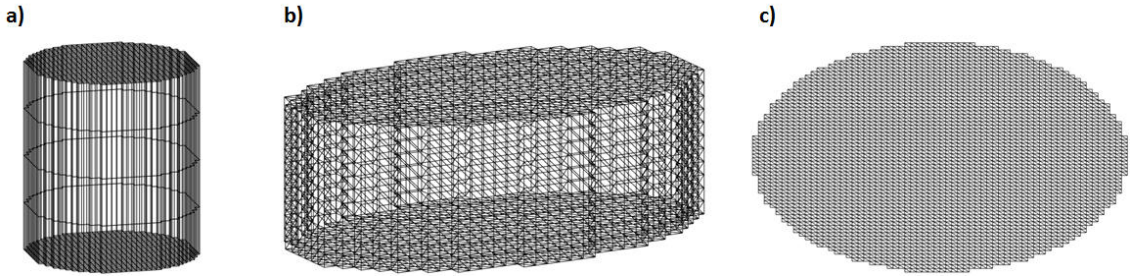

Figure 32. Three different types of inverse models based on the training process and geometry **a)** inverse model based on a 5 equispaced 2D transverse slices and cylindrical geometry **b)** inverse model based on voxels and elliptical cylinder geometry **c)** inverse model consisting of a single plane located vertically in the middle between the electrode planes

2.3. Physiological Data

The physiological data were recorded as a part of the measurement protocol described in the previous chapter. Two sets of 16 electrodes (Figure 20) were located in transverse planes 3cm and 5cm above the umbilicus. The wiring of the electrodes reflected a square pattern with skip4 stimulation. The rest of the measurement settings were kept as described in the last chapter and the experimental protocol was also the same, including baseline and Valsalva measurement.

2.4. Inverse models

For the investigation of the 3D image reconstruction, three different types of inverse models were built. The first type of inverse model specifies several reconstruction planes (5 in the present case see Figure 32a) and trains the model to reliably reconstruct conductivities on those planes. The conductivity between planes is kept constant in the 3D images. The reconstruction parameters used to train the GREIT algorithm were set to *wr*=0.2, *nf*=0.5, *ts*=0.02. The noise figure value was chosen based on the L-curve criterion. This model was used for 3D image reconstruction of the phantom data measurements.

The second type creates a voxel model (Figure 32b) and each voxel receives two training targets in the training process, such that a conductivity change can be reconstructed for each voxel. The reconstruction parameters used to train the GREIT algorithm were set to *wr*=0.2, *nf*=30, *ts*=0.02. The noise figure value was chosen based on the L-curve criterion. This model type was used for reconstruction of both physiological and phantom data.

Additionally, the physiological data was reconstructed with the help of a single plane inverse model (Figure 32c) in order to focus the image and remove projection of vertical contrast from the plane of interest as suggested by Grychtol et al. [95] and allow comparison with the conventional 2D image reconstruction method described previously. The noise figure was selected based on the L-curve criterion to be *nf*=4. The other GREIT reconstruction parameters were set to *wr*=0.2 and *ts*=0.02.

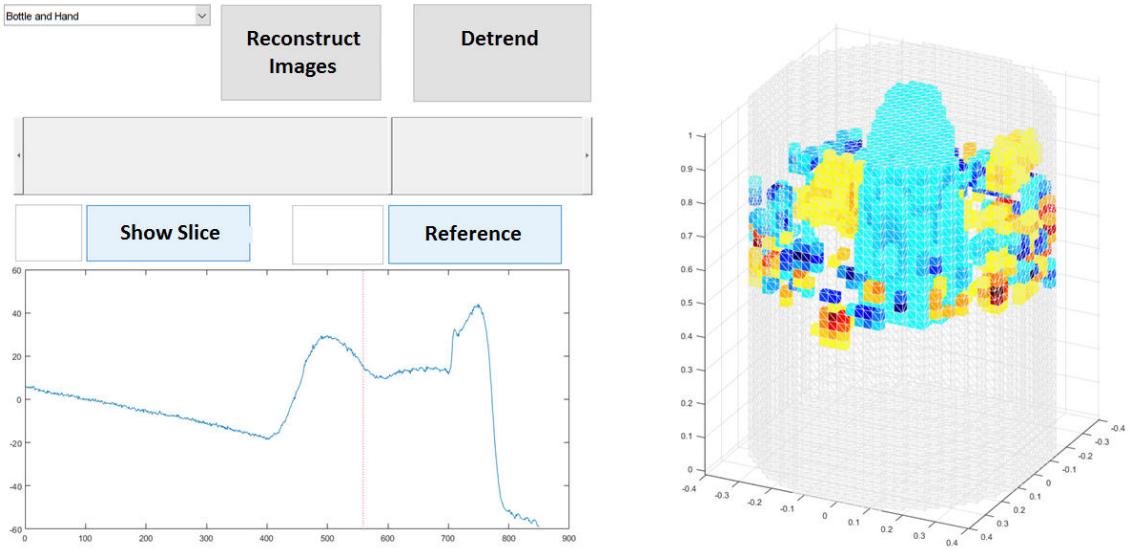

Figure 33. User interface created to simplify image browsing. Buttons with different functionality are visible A drop-down menu that allows for loading of different datasets; Reconstruction button; Detrend button that removes linear drift from a raw data; A slider that allows for browsing of different EIT frames; Show slice button that reconstructs the data on a single transversal slice; Reference button that enables choice of different baseline for reconstruction; A plot of the raw voltage signal with functionality to jump to a EIT frame with a mouse click; A window showing the 3D visualization of the reconstruction – right.

2.5. 3D reconstruction of phantom measurements

The data sets were filtered with a finite impulse response high pass filter with a cutoff frequency of 0.1 Hz to get rid of a surprising drift in the measurements. Difference image slices were calculated versus a baseline voltage vector representing empty tank, at 5 planes and without any further processing. Additional images were reconstructed with the voxel model of the water tank, again versus the baseline voltage signal, in order to compare both types of reconstruction.

2.6. User Interface

To simplify the visualization of images at different time instances, a user interface (figure 33) was developed with the following functionalities.

- A drop-down list of the different EIT measurement datasets available for loading
- A de-trend button that removes linear measurement drift from the loaded dataset
- A reconstruct button that reconstructs 3D images
- A slider that enabled frame by frame exploration of reconstructed images
- A Baseline button that allowed for the reconstruction of image versus a different baseline than the pre-set one

- Show slice button that enabled visualization of 2D slices from the 3D images
- A 3D image visualization window
- A plot of the mean voltage signal and a line indicating the displayed 3D frame

2.7. 3D images of the human abdomen

The physiological data was analyzed by creating functional EIT (fEIT) images (figure 34). This approach is useful in that it creates a single 3D image which reflects a physiological feature over a set of EIT frames. Two separate types of fEIT images were created reflecting cardiac activity and respiration. For the cardiac image, the apnea period was detected and the raw voltage data were band-pass filtered with a finite impulse response filter of 200^{th} order with cut-off frequencies of 0.5Hz and 6Hz followed by an ECG triggered ensemble averaging thus producing one voltage curve representing cardiac activity (Figure 34). The minimum and maximum point corresponding to the offset of the BP wave and its highest point respectively were detected and the average voltage data at those points used to create a difference EIT image. For visualization of the cardiac fEIT image, a threshold criterion of *th=0.5* was used to set all voxels below 50% of the maximum to zero.

For the respiration fEIT image, a tidal volume image was created. Three similar points each of inspiration and expiration were detected and a difference EIT image reconstructed with the inverse voxel model. For easier visualization, positive and negative conductivity change were images were created separately. The negative change image showed all voxels which exhibited conductivity change less than 20% of the minimum change across the whole volume and the positive image showed voxels that exhibited at least 20% of the maximum conductivity change.

2.8. Focusing EIT on a plane

For the focusing of EIT, the single plane inverse model was used and the voltage data from the two measuring planes was reconstructed, resulting in 2D EIT image frames. Since the format of the data is equivalent to the conventional 2D EIT, it was possible to apply the aortic search algorithm described in the last chapter.

3. Results

3.1. Phantom tank measurements

Images from the first experimental conditions ($\sigma = 0.49\ \mathrm{S\,m^{-1}}$, adjacent stimulation) could not be reconstructed. The voltage signal showed very low variability and was dominated by noise.

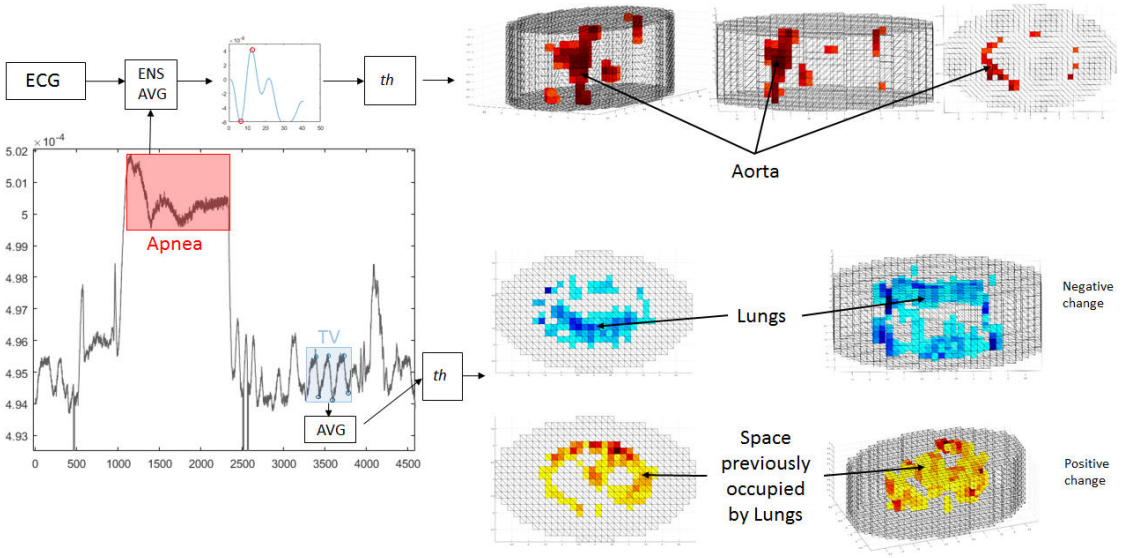

Figure 34. Schematic representation of the computation of the fEIT images. The cardiac fEIT is computed from the apnea period with the help of ECG triggered ensemble average and a threshold criterion. Dark red corresponds to higher conductivity change. The respiration fEIT image is created by detecting three frames of inspiration and expiration each, averaging them, subtracting them and finally application of a threshold criterion that separates positive from negative conductivity changes.

After increasing the conductivity of the solution and changing the stimulation pattern to skip4, the SNR of the voltage signal increased and enabled reconstruction of 3D images.

For the first measurement, the empty soda bottle was immersed in the water solution together with the hand of the experimenter. Noticeable conductivity changes can be seen in the time series of the mean signal (Figure 35 top). The voltage signal peaks after frame 3 and then it starts decreasing again, reaching a minimum around frame 4 which corresponds to fully immersed bottle. The qualitative difference between hand and bottle, however, is hard to spot in the images (frame 4 and frame 5).

Next, the bottle and the tube were immersed in the water solution in parallel (Figure 36). The tube is not visible in the reconstructed images although it should have the same conductivity as the bottle. The bottle being the bigger object overshadows the relatively small tube. In frame 5 the objects are taken away from the measurement plane, but the reconstructed image shows a conductivity change of an even higher transversal area compared to frames 3 and 4. In frame 6 the objects are fully removed from the water and the 3D image shows no structures. Frame 2 is calculated at the onset of the immersion of the objects. The voltage signal shows a slight decrease in that point similar to the decrease before frame 5 when the objects are removed from the tank.

Qualitatively the best images (Figure 37) were produced by the objects with opposite conductivities with respect to the background conductivity of the water solution. Here a good contrast between the two objects can be seen. It has to be noted that their reconstructed size is a lot larger than their real size.

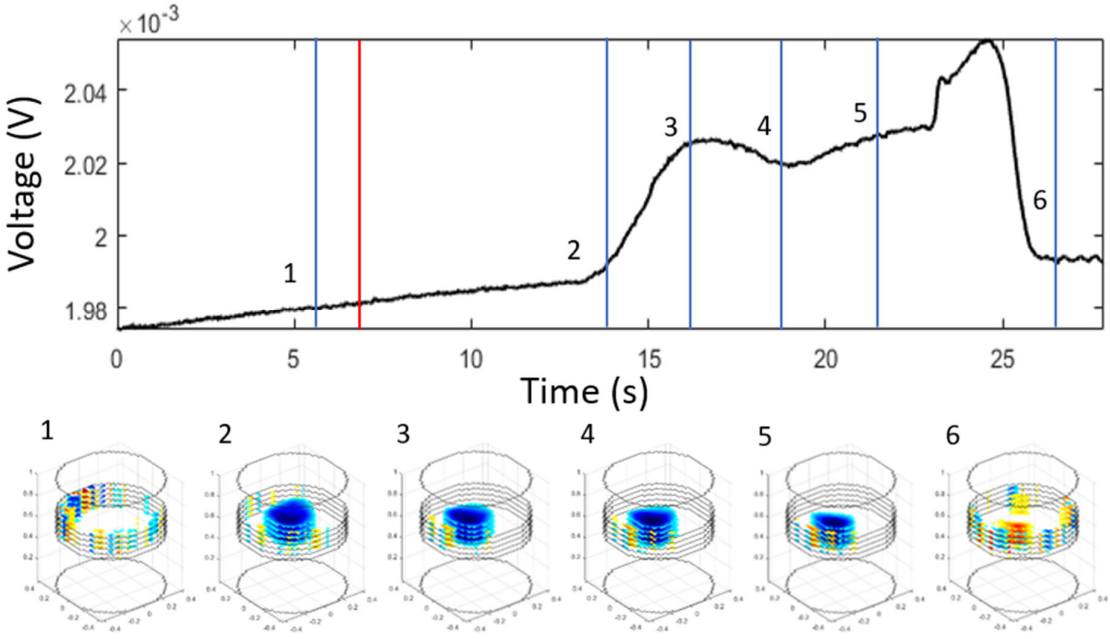

Figure 35. The empty soda bottle immersed vertically followed by the hand of the experimenter. Reconstructed 3D images corresponding to time instances shown in the upper plot. Red line shows the time instance of the reference image used for reconstruction. Negative to positive conductivity changes are color coded from dark blue to dark red.

The diameter of the tube is 2cm and the file has a width of 2.5cm and thickness of 0.5cm. The difference in contrast as a function of vertical position is especially noticeable for the metal file. The metal file having an approximate conductivity of $\sigma = 7 * 10^6\ \mathrm{S\,m^{-1}}$ [109], has a much higher conductivity than the background $\sigma = 1.95\ \mathrm{S\,m^{-1}}$ and therefore is reconstructed as a positive change while the plastic tube ($\sigma = 5 * 10^6\ \mathrm{S\,m^{-15}}$) [96] will be reconstructed as a negative conductivity change. A good contrast can be seen between images when the objects are immersed at different depths. In frame 2 the objects are above the center of the measurement volume and the absolute reconstructed conductivity change is lower compared to the next frame where they are centered in the measurement volume. In frame 4 the objects are immersed to the bottom of the tank. Here the amplitude change in conductivity is even more pronounced. The area occupied by the file in frame 3 is now occupied by the hand of the experimenter, thus the lower conductivity. However, one would expect the hand to have a negative conductivity change. The horizontal sensitivity of the system was tested by immersing the plastic tube in the water solution and then moving it around in the water tank. It can be seen that the resolution of the system is far superior when the object is closer to the electrodes (Figure 38 frames 4, 6 and 7) as opposed to being in the middle of the tank (frames 3 and 5). An interesting trail - like artifact can be seen in frame 6. Images at the same time instances were reconstructed also with the voxel model. The position of the object was reconstructed very similarly with the two models. However, the voxel model seems to reconstruct the object with a higher resolution in the transverse plane.

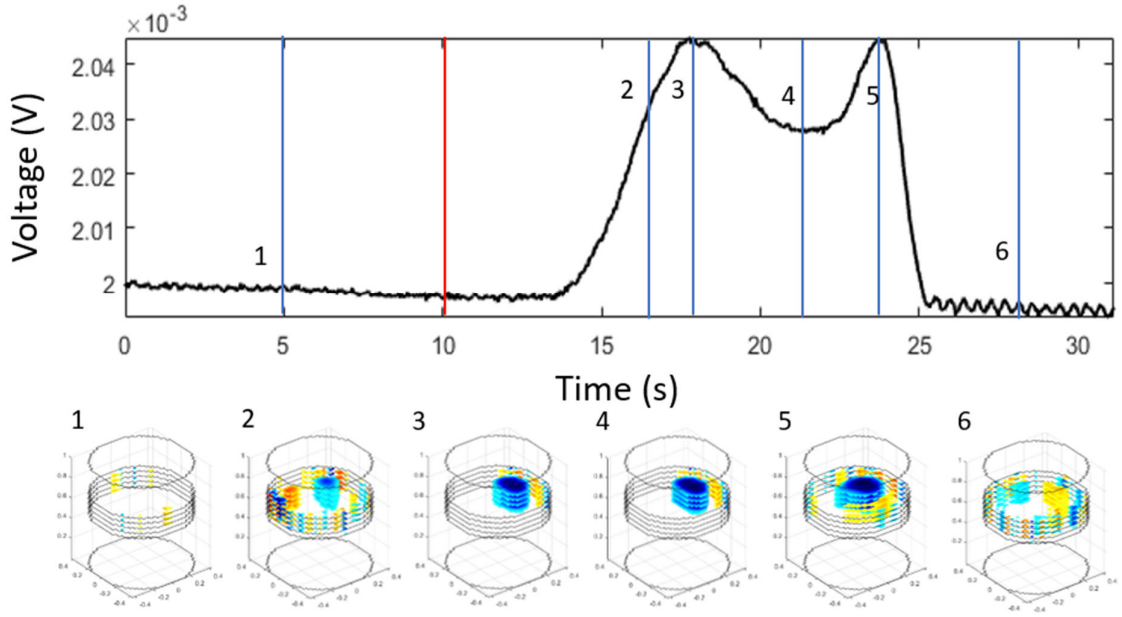

Figure 36. The empty soda bottle and the plastic tube immersed vertically in parallel. Reconstructed 3D images corresponding to time instances shown in the upper plot. Red line shows the time instance of the reference image used for reconstruction. Negative to positive conductivity changes are color coded from dark blue to dark red.

This effect is especially pronounced in frame 7 where a long thin non-conductive object can be seen, compared to the banana-shaped object reconstructed with the 5 planes inverse model (Figure 38). The voxel model also produced wider images in the middle of the tank, similar to the planes model.

3.2. Physiological data

Three-dimensional fEIT images were created for the physiological data as measured by two planes of 16 electrodes. A cardiac image was created representing a difference EIT image between the frames of maximum and minimum of an ECG triggered ensemble averaged voltage signal (Figure 34). After applying the threshold criterion a long and thin aorta-like structure can be seen in the 3D images. The respiration fEIT images are decomposed in positive and negative change. The positive change image always showed two holes in the middle encircled by voxels that increased their conductivity from inspiration to expiration (Figure 34). The dorsal upper part of the image was always occupied by voxels exhibiting negative conductivity change.

The discrimination function described in the previous chapter was able to isolate a region associated with the aorta (Figure 39a) and determine the PAT of the BP wave. In the 2D focused image, the PAT was constant throughout the whole aortic region, in contrast to the conventional 2D .where often more than one PAT was assigned to the aorta. The ensemble averaged wave, however, was more distorted and showed less improvement of SNR (Figure 39b).

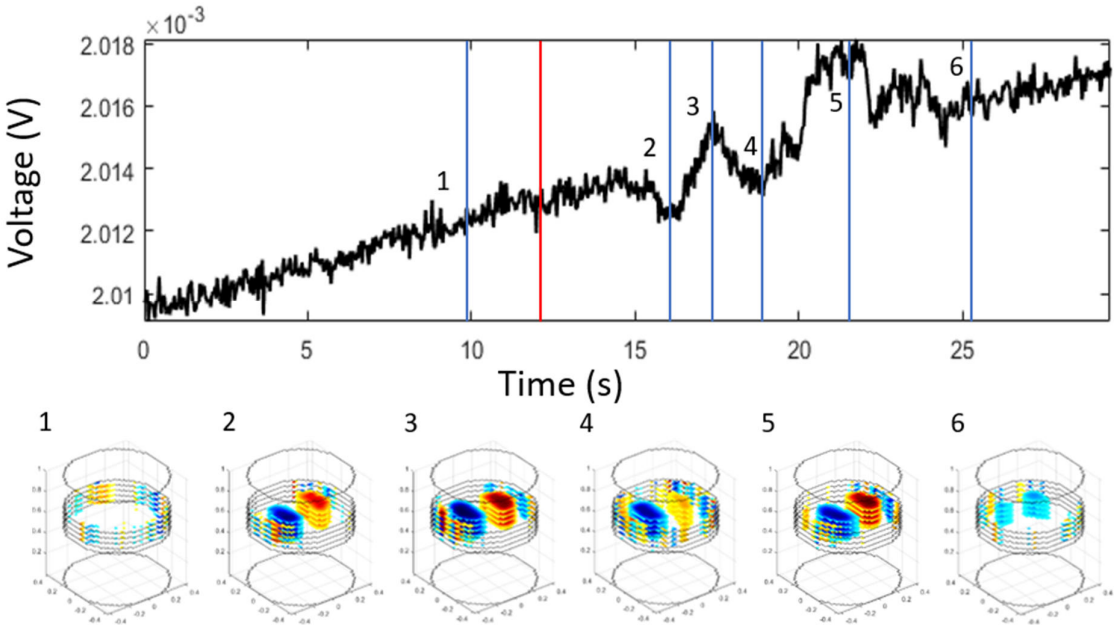

Figure 37. The plastic tube and the metallic file immersed vertically in parallel. Reconstructed 3D images corresponding to time instances shown in the upper plot. Red line shows the time instance of the reference image used for reconstruction. Negative to positive conductivity changes are color coded from dark blue to dark red.

4. Discussion

The purpose of this chapter was to attempt 3D EIT reconstruction and study the vertical and horizontal sensitivity of EIT with the help of a water tank and different phantom objects of different size and conductivity. 3D images of the phantom objects immersed in a water tank were reconstructed with different reconstruction strategies. Functional 3D EIT images of physiological data were created with an inverse voxel model and additionally, EIT images focused on one plane from two measuring planes were reconstructed and compared to conventional 2D reconstruction. The results of the experiments showed some very interesting results that confirmed theoretical and experimental findings.

4.1. Water tank experiments

For the first experimental conditions ($\sigma = 0.49$ S m^{-1}, adjacent stimulation), the recorded signals had very low amplitudes due to the low sensitivity of the system in the center of the tank when driven by adjacent stimulation with no gap between stimulation electrodes[97],[98],[99] and possibly due to the

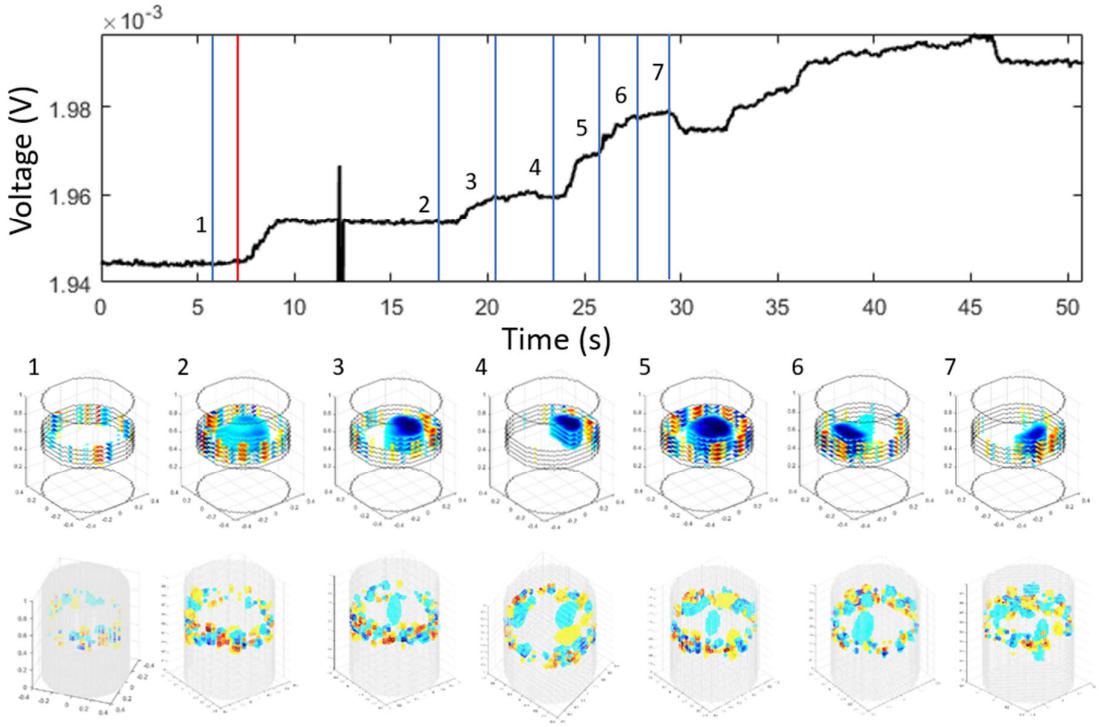

Figure 38. The plastic tube immersed in the water tank and moved around the tank. Reconstructed 3D images corresponding to time instances shown in the upper plot. Red line shows the time instance of the reference image used for reconstruction. Negative to positive conductivity changes are color coded from dark blue to dark red.

relatively low conductivity of the solution. The change of stimulation pattern to skip4 for the second experimental condition improved the signal quality as expected. Additionally, it is very likely that the increase of conductivity of the salt solution also had an effect on the signal strength, because with more salt concentration there are more charge carriers available for the current flow.

The positional dependence of the reconstruction of the same object as a function of the distance from the electrodes is illustrated in Figure 38. In time instance '5', the 2cm diameter tube is projected on a much larger region compared to time instances '4', '6' or '7', where the tube is close to the electrodes. This shows the higher sensitivity of EIT to superficial regions and also illustrates the effects of position dependability of the GREIT reconstruction algorithm. It can be seen that the resolution is lower in the middle of the system, while shape deformation seems lower close the electrodes, where the plastic tube is reconstructed as a banana-shaped object. The voxel model images seem to have higher resolution, possibly due to the fact that the model was trained with a higher number of training targets (2 per voxel). Additionally, the voxel model images don't show such high shape deformation close to the electrodes, on the contrary frame '7' is the frame where the plastic tube is reconstructed with the highest accuracy regarding its shape.

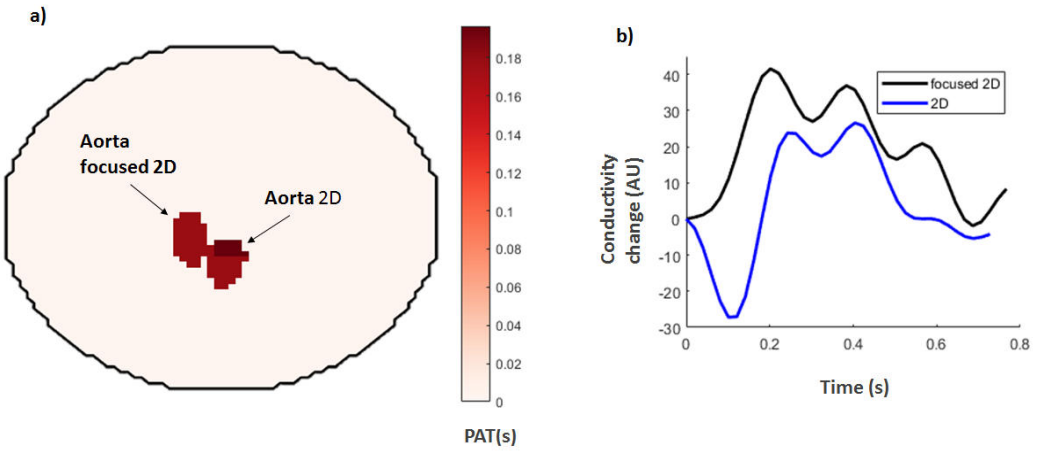

Figure 39. Results of the aortic search algorithm in a) for subject 2 from the 2D and 2D focused EIT datasets of the baseline measurement. b) Ensamble averaged aortic BP wave for 2D and focused 2D EIT datasets for subject 2 baseline measurement

It wasn't possible to locate a time instance where the conductivity change in the images (from air to tissue) is substantial in the experiment where the bottle and the hand were immersed in the water tank (Figure 35). The local minimum in the voltage measurement around frame 4, however, is most likely a result of the hand of the experimenter occupying the measured volume instead of the less conductive soda bottle. Theoretically, a nonconductive object should be shown in the lower parts of the tank while a little more conductive in the upper parts. At around 0.37 S m^{-1} the muscle conductivity is still lower than the conductivity of the salt solution used of 1.95 S m^{-1} and it should be visible as a negative change in conductivity (blue). This experiment has to be repeated more carefully and it can show us the sensitivity of the system in the vertical direction.

In the reconstructed images of the parallel immersion of the plastic tube and the soda bottle (Figure 36), the plastic tube cannot be seen. Although both objects should have the same conductivity because they are filled with air, the bigger object – the bottle overshadows the tube. Similar results were achieved by Ahn et al. [94], but for simulations and conductive objects with different sizes. It is possible that the overshoot (ringing) around the bottle has a similar amplitude as the amplitude of the plastic tube and therefore the two signals cancel each other.

It can be concluded, that the reconstruction algorithm still projects some vertical contrasts, even though 2 rows of electrodes are used. The resolution of the system in *z*-direction was poor and the instances where the objects entered the measurement volume could not be detected. There was an improvement in position error and resolution observed when moving the targets toward the electrodes compared to the more deep regions. Both *z* – and *xy* - resolution can be increased by employing another stimulation pattern. As seen in the thesis of Wagenaar [93], the planar stimulation pattern performs best in *xy* - direction and the non-uniformity of resolution and shape deformation are less pronounced compared to

the square pattern, while zigzag pattern has the best resolving power in *z*-direction. However, the square stimulation pattern, although not having the best resolution in any one direction, has the most uniformly distributed resolution across all dimensions.

4.2. Physiological data

The positive conductivity change visible in the respiration fEIT images most probably is a result of the relaxation of the diaphragm and retraction of the less conductive lung tissue that is substituted by a more conductive muscle tissue. The shape of the reconstruction very much resembles this hypothetical situation and the inferior concave surface of the lungs (Figure 11b). The image of the negative change supports the hypothesis because it shows high activity in the superior regions where the lungs should be.

The elongated structure that passes through the whole height of the volume in the cardiac fEIT image could be the aorta. If the location of that structure is compared with the results from the 2D focused EIT (Figure 39), it can be seen that they seem to occupy the same region. Similar to the results of the results of the human subject tests in the last chapter, ground truth was not available for validation which is a major drawback of the work.

The detected aortic regions presented in Figure 39 from the 2D and 2D focused EIT do not overlap, although the signals are measured on the same subject with a similar study protocol. It is possible that due to movement between the two datasets the aorta has been displaced, but it is unlikely it has been displaced that much. Most probably, the reconstruction and stimulation settings used to produce the two images have a higher influence on the detected position. First, the goal of 2D focused EIT is to reduce the effects of projection of vertical contrasts on the measurement plane. Therefore, the slight deviations of the aorta from the vertical axis of the body will be less visible in the 2D focused image and this might change its position in the images.

The measure aortic PAT is equal in value for both 2D and focused 2D EIT, but for the focused case the PAT across the whole region is constant. When the sensitivity of the system is more vertically confined as is in focused 2D EIT, this effect is expected, because there is less projection of off-plane conductivities.

The ensemble averaged aortic BP waveforms from the two modalities show similar amplitude and form, as well as the same PAT. However, the BP wave produced with the 2D focused EIT is more distorted and shows more variability with one additional peak. When stimulating the system with two rows of electrodes, the stimulation pattern possibilities are a lot more compared to only a single electrode plane. With the square stimulation pattern used (figure 30c) the current flow alternates between pure transversal stimulation (e.g. Electrodes 2-7 or 4-9) and stimulation between electrodes in different planes (e.g. Electrodes 1-6 or 3-8) that also includes vertical current flow thus increasing the vertical

information collected. However, by collecting more vertical information about the conductivities, the transversal information is reduced. That essentially results in reduced sampling rate from around 50 transversal frames per second to 25 pure transversal frames and 25 mixed vertical and transversal frames, thus reducing the SNR of the BP wave.

The analysis provided in this chapter is based mostly on qualitative observations about 3D EIT reconstruction. There is little literature available on this particular type of problem and therefore little is known about the best stimulation patterns, electrode configuration, reconstruction models and reconstruction parameters. This first effort in the direction of 3D EIT provided a lot of intuition about mechanisms behind the problem. In a future work, a more quantitative analysis of different types of inverse models has to be done. Additionally, the phantom objects used for the measurements have to be placed more precisely with a known position and should be vertically confined in order to allow for quantification of the results. The objects should not be held by hand during the measurement and the hand should not enter the measurement volume. In the thesis of Waldmann [100], an automated test robot was used to insert the objects with a known position and they were vertically confined by attaching them to a thin string that has no effect on the image.

Overall, 3D EIT image reconstruction seems to overcome the disadvantages of conventional 2D EIT. However, there are several questions that still need answering: What are the best stimulation patterns for 3D EIT signal acquisition? What is the optimal electrode placement? What reconstruction parameters should be used? Which type of inverse model is most appropriate for 3D reconstruction and visualization of hemodynamics in human subjects?

V. Conclusion

The aim of this thesis was to adopt a comprehensive approach to the problem of non-invasive BP measurement with EIT. Therefore the work was structured in three parts setting three important objectives.

First, since the EIT reconstruction problem is a non-linear ill-posed ill-conditioned inverse problem, the choice of the reconstruction algorithm, as well as its parameters, would influence the reconstructed image greatly. Therefore, the first objective was to determine a set of reconstruction parameters and measurement setups that would be the most suitable for the application of EIT to non-invasive BP measurement.

The second part of the work is dedicated to the signal processing part of the reconstructed EIT images. A sophisticated aortic search algorithm was developed and validated and the signal coming from the aortic pixels was analyzed for detection of PAT with state of the art method. The results of the PAT measurement were correlated with the MAP measured with a standard blood pressure measurement device in order to determine if non-invasive central BP measurement is possible with EIT. This was the second objective of the thesis.

The third and final objective was to explore 3D reconstruction of EIT images, first from phantom measurements in the water tank and then on physiological data.

In order to approach the EIT imaging of hemodynamics systematically, first, the best reconstruction parameters for the GREIT reconstruction algorithm were selected in a series of simulations. Particularly, the influence of the noise figure on the reconstructed images was investigated by simulating conductivity changes in the aortic area and assessing the reconstruction quality based on the FOM. The noise figure controls the noise performance of the reconstruction algorithm and influences the amount of regularization. The noise figure tests included reconstruction of in-vivo data with inverse models with noise figure parameter ranging from NF=0.5…2.4. The ability of an aortic search algorithm to detect the aortic pixels was assessed as a function of the noise figure. Additionally, 30 measurement setups with a different combination of electrodes size and stimulation pattern were simulated and their performance assessed based on the quality of the reconstructed images in the aortic area with the help of the FOM.

The results of the different simulations provided an important insight for the non-invasive BP measurement with EIT. First, the FOM analysis on the influence of the noise figure on the reconstruction of pixels in the aortic region showed that generally higher noise figures perform better. Specifically, NF=1.9…2.1 showed the best compromise between the different FOM. The aortic search was also the most successful for NF=2 with F-1 score and distance between the detected region and the aortic region segmented from CT images of 0.3 and 3.2 pixels respectively.

The FOM as a function of electrodes size behaved inversely for adjacent stimulation and opposite stimulation, while the 45° stimulation a mixture of both. The best performing electrodes for adjacent stimulation were the ones with the largest radius r=0.05m while for opposite stimulation were the ones with the smallest radius r=0.005. For 45° stimulation again the largest electrode size performed best.

The higher noise figures performed better, for all tests. By increasing the SNR of the image, the resolution increased and smaller structures became easier to detect. However, the noise figure is not a versatile noise performance metric, because it is specifically determined for each measurement setup. Consequently, the results of this experiment were useful for the analysis of the animal data, but not for the human subject experiments.

In general, the results of the electrode size simulations show several useful trends. With increasing the distance between the stimulating electrodes the all PE, RES, and SD get worse, but AR and RNG get better. This of confirms the theory that opposite stimulation would be more sensitive to the central regions (AR is higher), but since less information overall is acquired the other FOM perform worse. Also, bigger electrodes are better in general, because they have a larger sensing area, thus probe more potential lines.

The third chapter of this thesis is devoted to achieving the second objective – non-invasive BP measurement with EIT. EIT signal from the abdominal area of five human subjects was acquired together with ECG and BP signals among others. The EIT voltage signals were used to reconstruct images of the abdominal conductivity changes of the subjects. A sophisticated aortic search algorithm was developed, that exploited ECG triggered ensemble averaging and frequency features to detect aortic pixels. Once the aortic pixels were detected, the PAT of the BP wave was measured. Finally, the PAT and MAP were tested for linear correlation.

The aortic search algorithm was validated on animal data with intramodal (F1-score 0.8124) and intermodal (F1-score 0.2414) ground truth available and a high F1-score was achieved. The aortic region was subsequently successfully detected in all human subjects. The MAP measured with a standard BP device and the PAT measured with EIT showed a strong inverse correlation (r=-0.8593).

The experiment showed the ability of EIT to detect deep small structures such as the aorta. The strong correlation between the PAT measured with EIT and the MAP suggests that EIT could be used for non-invasive BP measurement in a clinical setting. Due to the off-plane sensitivity of EIT, the accuracy of the BP measurement is a function of the stiffness of the vessels. Patients with higher vessel stiffness would exhibit longer BP waves and the pressure drop in the EIT sensitivity region will be more constant.

In order to reduce the effect of off-plane sensitivity, 3D EIT measurement is utilized. The third objective of this work was to explore 3D image reconstruction from phantom data and physiological measurements with different inverse models. To that end, a water tank with two rows of electrodes was

build and objects with various sizes and conductivities were immersed into the water solution. The measured signals were reconstructed with inverse voxel model and with an inverse model with several transversal planes specified. For easier visualization of the results, a user interface was developed. The physiological data was reconstructed with an inverse voxel model for 3D visualization and also an EIT focusing technique was applied, that creates 2D images from 3D data.

In the reconstructed 3D images the plastic tube with 2cm diameter could not be reliably reconstructed when it was positioned in the center of the tank. The metal file showed the best vertical sensitivity because it had the highest conductivity difference with respect to the water solution. The images from focused EIT were analyzed with the aortic search algorithm and the aorta was successfully detected. The PAT was constant across the whole aortic region in contrast to the 2D, which suggest lack of off-plane projections.

Future Work

The work done in this thesis suggests that EIT could potentially be used as a non-invasive continuous alternative for central BP measurements. However, before the technology is adopted as a clinical use, there are areas that require additional development. Future work on this topic could include:

1. The best reconstruction parameters for central BP measurements with EIT have to be more systematically determined. In this work, we looked at the noise figure. However, there are numerous ways to tune the GREIT reconstruction algorithm and they all have to be tested. A work similar to the one done by Thürk et al. [66] for lung imaging, can be and should be done for imaging of hemodynamic parameters with EIT.
2. A larger study on human subjects that measures the central BP with EIT and compares it with standardized clinical BP measurement. There is data available on 40 human patients and the first results were promising.
3. The 3D image reconstruction should be investigated in more detail and reconstruction algorithm should be developed that are tailored for the exact application. More precisely, different stimulation patterns and electrode placements have to be systematically tested in order to select the ones that perform best for hemodynamic imaging with EIT.

Appendix

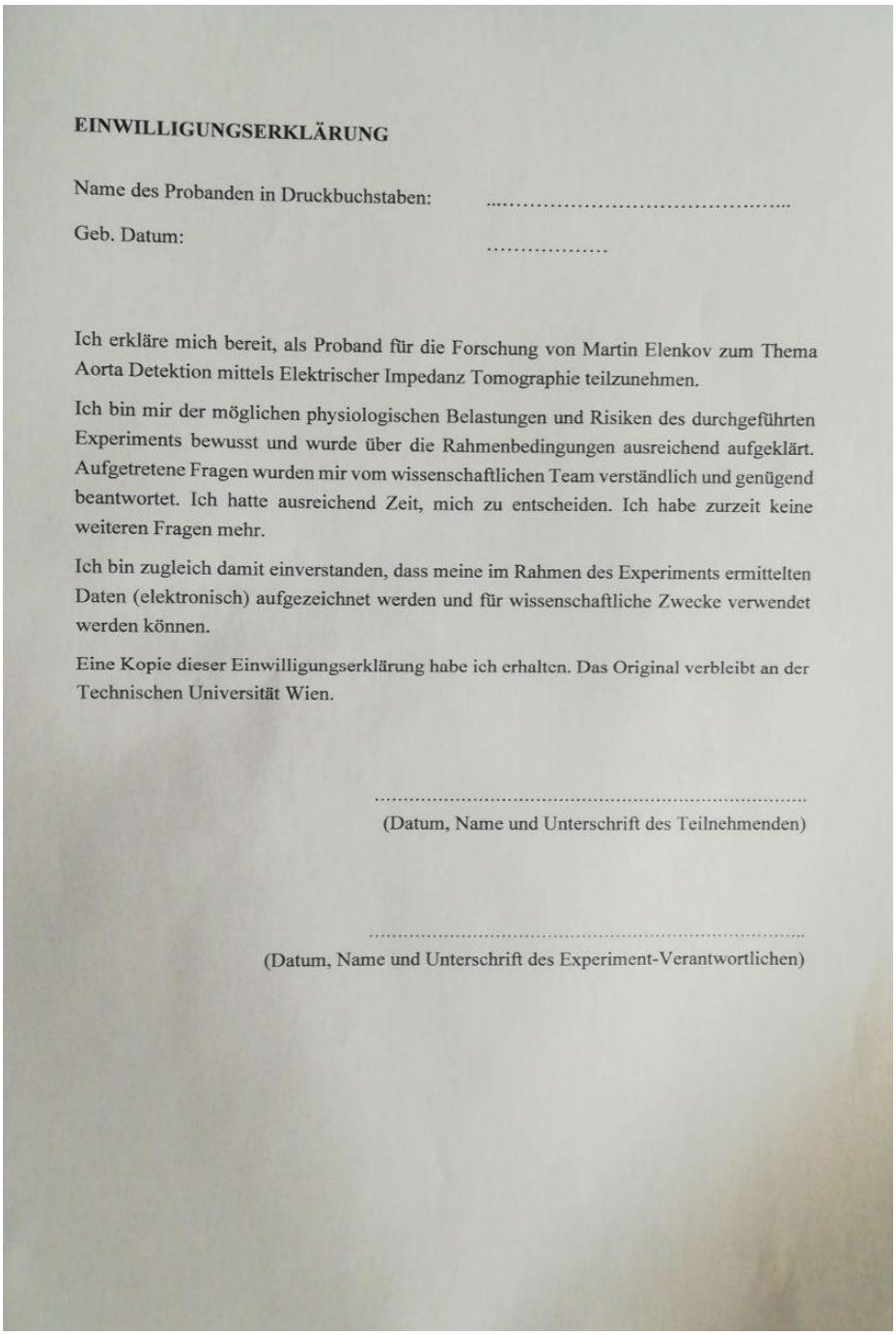

EINWILLIGUNGSERKLÄRUNG

Name des Probanden in Druckbuchstaben: .....

Geb. Datum: .....

Ich erkläre mich bereit, als Proband für die Forschung von Martin Elenkov zum Thema Aorta Detektion mittels Elektrischer Impedanz Tomographie teilzunehmen.

Ich bin mir der möglichen physiologischen Belastungen und Risiken des durchgeführten Experiments bewusst und wurde über die Rahmenbedingungen ausreichend aufgeklärt. Aufgetretene Fragen wurden mir vom wissenschaftlichen Team verständlich und genügend beantwortet. Ich hatte ausreichend Zeit, mich zu entscheiden. Ich habe zurzeit keine weiteren Fragen mehr.

Ich bin zugleich damit einverstanden, dass meine im Rahmen des Experiments ermittelten Daten (elektronisch) aufgezeichnet werden und für wissenschaftliche Zwecke verwendet werden können.

Eine Kopie dieser Einwilligungserklärung habe ich erhalten. Das Original verbleibt an der Technischen Universität Wien.

.....

(Datum, Name und Unterschrift des Teilnehmenden)

.....

(Datum, Name und Unterschrift des Experiment-Verantwortlichen)

References

[1] R. Lozano *et al.*, “Global and regional mortality from 235 causes of death for 20 age groups in 1990 and 2010: A systematic analysis for the Global Burden of Disease Study 2010,” *Lancet*, vol. 380, no. 9859, pp. 2095–2128, 2012.

[2] World Organization. World Heart Federation. World Stroke Organization, “Global Atlas on Cardiovascular disease prevention and control,” *Glob. atlas Cardiovasc. Dis. Prev. Control.*, 2011.

[3] G. F. Mitchell, “Arterial stiffness and wave reflection: Biomarkers of cardiovascular risk,” *Artery Res.*, vol. 3, no. 2, pp. 56–64, 2009.

[4] R. Asmar, *Arterial Stiffness and Pulse Wave Velocity. Clinical applications*. 1999.

[5] T. G. Pickering *et al.*, “Recommendations for blood pressure measurement in humans and experimental animals: Part 1: Blood pressure measurement in humans - A statement for professionals from the Subcommittee of Professional and Public Education of the American Heart Association Co,” *Circulation*, vol. 111, no. 5, pp. 697–716, 2005.

[6] M. Riachy, E. Riachy, G. Sleilaty, G. Dabar, A. Yazigi, and K. G., “Reliability and survival of arterial catheters: optimal dynamic response,” *Ann. Fr. Anesth. Reanim.*, vol. 11, no. 276, pp. 889–97, 1996.

[7] A. F. Connors Jr. *et al.*, “The effectiveness of right heart catheterization in the initial care of critically ill patients,” *Jama*, vol. 276, no. 11, pp. 889–897, 1996.

[8] V. D. Mayr *et al.*, “Causes of death and determinants of outcome in critically ill patients,” *Crit. Care*, vol. 10, no. 6, pp. 1–13, 2006.

[9] K. Lakhal, S. Ehrmann, and T. Boulain, “Non-invasive blood pressure monitoring in the critically ill: time to abandon the intra-arterial catheter?,” *Chest*, no. November, 2017.

[10] R. J. Levick, *An Introduction to Cardiovascular Physiology 5E*, vol. i. 2009.

[11] E. Kaniusas, *Biomedical Signals and Sensors I*. 2008.

[12] P. Boutouyrie, P. Lacolley, X. Girerd, L. Beck, M. Safar, and S. Laurent, “Sympathetic activation decreases medium-sized arterial compliance in humans.,” *Am. J. Physiol.*, 1994.

[13] T. Jafar *et al.*, “Progression of chronic kidney disease: the role of blood pressure control, proteinuria, and angiotensin-converting enzyme inhibition: a patient-level meta-analysis.,” *Ann. Intern. Med.*, 2003.

[14] M. Sokolovsky, “Endothelin receptor subtypes and their role in transmembrane signaling

mechanisms.," *Pharmacol. Ther.*, 1995.

[15] M. Faber and G. Oller-Hou, "The human Aorta. V. Collagen and elastin in the normal and hypertensive aorta.," *Acta Pathol Microbiol Scand*, 1952.

[16] P. Salvi, *Pulse Waves: How Vascular Hemodynamics Affects Blood Pressure*. .

[17] S. Laurent *et al.*, "Aortic stiffness is an independent predictor of fatal stroke in essential hypertension," *Stroke*, vol. 34, no. 5, pp. 1203–1206, 2003.

[18] L. H. G. Henskens *et al.*, "Increased aortic pulse wave velocity is associated with silent cerebral small-vessel disease in hypertensive patients," *Hypertension*, vol. 52, no. 6, pp. 1120–1126, 2008.

[19] P. Fesler, M. Safar, G. du Cailar, J. Ribstein, and A. Mimran, "Pulse pressure is an independent determinant of renal function decline during treatment of essential hypertension.," *J. Hypertens.*, 2007.

[20] M. AM, D. LI, and M. HH, "The normal blood pressure range and its clinical implications," *J. Am. Med. Assoc.*, vol. 143, no. 17, pp. 1464–1470, Aug. 1950.

[21] J. Solà, S. F. Rimoldi, and Y. Allemann, "Ambulatory monitoring of the cardiovascular system: the role of Pulse Wave Velocity," *InTech*, vol. 01.2010, 2010.

[22] M. Butlin, "Structural and functional effects on large artery stiffness : an in-vivo experimental investigation Structural and functional effects on large artery stiffness : an in-vivo experimental investigation," *Thesis*, 2007.

[23] M. Rajzer, W. Wojciechowska, M. Klocek, I. Palka, M. Brzozowska-Kiszka, and K. Kawecka-Jaszcz, "Comparison of aortic pulse wave velocity measured by three techniques: Complior, SphygmoCor and Arteriograph.," *J. Hypertens.*, 2008.

[24] N. Westerhof, Nicolaas, Stergiopulos and M. I. M. Noble, *Snapshots of Hemodynamics*. 2010.

[25] Marko Vauhkonen, *Electrical impedance tomography and prior information*. 1997.

[26] J. Wagenaar and A. Adler, "Electrical impedance tomography in 3D using two electrode planes: Characterization and evaluation," *Physiol. Meas.*, vol. 37, no. 6, pp. 922–937, 2016.

[27] B. Grychtol, B. Müller, and A. Adler, "3D EIT image reconstruction with GREIT," *Physiol. Meas.*, vol. 37, no. 6, pp. 785–800, 2016.

[28] S. Pulletz *et al.*, "Comparison of different methods to define regions of interest for evaluation of regional lung ventilation by EIT.," *Physiol. Meas.*, vol. 27, no. 5, pp. S115–S127, 2006.

[29] S. Zlochiver *et al.*, “A portable bio-impedance system for monitoring lung resistivity,” vol. 29, pp. 93–100, 2007.

[30] D. Ferrario, B. Grychtol, A. Adler, J. Sola, S. H. Bohm, and M. Bodenstein, “Toward morphological thoracic EIT: Major signal sources correspond to respective organ locations in CT,” *IEEE Trans. Biomed. Eng.*, vol. 59, no. 11 PART1, pp. 3000–3008, 2012.

[31] I. Frerichs *et al.*, “Chest electrical impedance tomography examination, data analysis, terminology, clinical use and recommendations: consensus statement of the TRanslational EIT developmeNt stuDy group.,” *Thorax*, p. thoraxjnl-2016-208357, 2016.

[32] M. Proença, “Non-invasive hemodynamic monitoring by electrical impedance tomography PAR,” vol. 7444, 2017.

[33] F. Braun *et al.*, “Influence of heart motion on cardiac output estimation by means of electrical impedance tomography : a case study.”

[34] J. Solà, A. Adler, A. Santos, G. Tusman, F. Sua, and S. H. Bohm, “Non-invasive monitoring of central blood pressure by electrical impedance tomography : first experimental evidence,” *Med. Biol. Eng. Comput.*, vol. 49, pp. 409–415, 2011.

[35] L. Gladden, *Process Tomography: Principles, techniques and applications*. 1997.

[36] A. Samouëlian, I. Cousin, A. Tabbagh, A. Bruand, and G. Richard, “Electrical resistivity survey in soil science: A review,” *Soil Tillage Res.*, vol. 83, no. 2, pp. 173–193, 2005.

[37] B. Grychtol, G. Elke, P. Meybohm, N. Weiler, I. Frerichs, and A. Adler, “Functional validation and comparison framework for EIT lung imaging,” *PLoS One*, vol. 9, no. 8, 2014.

[38] M. Allaud, Louis; Martin, *Schlumberger: The history of a technique*. 1977.

[39] R. P. Henderson and J. G. Webster, “An impedance camera for spatially specific measurements of the thorax.,” *IEEE Trans. Biomed. Eng.*, vol. 25, no. 3, pp. 250–254, 1978.

[40] D. S. Holder, “Electrical Impedance Tomography: Methods, History and Applications,” *CRC Press*, p. 456, 2004.

[41] T. Tidswell, A. Gibson, R. H. Bayford, and D. S. Holder, “Three-Dimensional Electrical Impedance Tomography of Human Brain Activity,” *Neuroimage*, vol. 13, no. 2, pp. 283–294, 2001.

[42] A. P. Bagshaw *et al.*, “Electrical impedance tomography of human brain function using reconstruction algorithms based on the finite element method,” *Neuroimage*, vol. 20, no. 2, pp. 752–764, 2003.

[43] R. J. Halter, A. Hartov, and K. D. Paulsen, “A broadband high-frequency electrical impedance tomography system for breast imaging,” *IEEE Trans. Biomed. Eng.*, vol. 55, no. 2, pp. 650–659, 2008.

[44] Y. Zou and Z. Guo, “A review of electrical impedance techniques for breast cancer detection,” *Med. Eng. Phys.*, vol. 25, no. 2, pp. 79–90, 2003.

[45] A. Keshtkar, Z. Salehnia, A. Keshtkar, and B. Shokouhi, “Bladder cancer detection using electrical impedance technique (Tabriz Mark 1),” *Patholog. Res. Int.*, vol. 2012, no. 1967, 2012.

[46] S. Leonhardt *et al.*, “Electric impedance tomography for monitoring volume and size of the urinary bladder,” *Biomed. Tech.*, vol. 56, no. 6, pp. 301–307, 2011.

[47] M. Proença *et al.*, “Aortic blood pressure measured via EIT : investigation of different measurement settings.”

[48] Q. S. Zhu, C. N. McLeod, C. W. Denyer, F. J. Lidgey, and W. R. B. Lionheart, “Development of a real-time adaptive current tomograph,” *Physiol. Meas.*, vol. 15, no. 2A, 1994.

[49] G. J. Saulnier, A. S. Ross, and N. Liu, “A high-precision voltage source for EIT,” *Physiol. Meas.*, vol. 27, no. 5, 2006.

[50] T. I. Oh, H. Wi, D. Y. Kim, P. J. Yoo, and E. J. Woo, “A fully parallel multi-frequency EIT system with flexible electrode configuration: KHU Mark2,” *Physiol. Meas.*, vol. 32, no. 7, pp. 835–849, 2011.

[51] D. S. Holder, “ELECTRICAL IMPEDANCE Edited by,” 2005.

[52] A. Adler, B. Grychtol, and R. Bayford, “Why is EIT so hard, and what are we doing about it?,” *Physiol. Meas.*, vol. 36, no. 6, pp. 1067–1073, 2015.

[53] R. Kohn and M. Vogelius, “Determining conductivity by boundary measurements,” *Commun. Pure Appl. Math.*, vol. 37, no. 3, pp. 289–298, 1984.

[54] H. Pfützner, *Angewandte Biophysik*, 1st ed. Springer, 2002.

[55] P. Nopp, N. D. Harris, T. X. Zhao, and B. H. Brown, “Model for the dielectric properties of human lung tissue against frequency and air content,” *Med. Biol. Eng. Comput.*, vol. 35, no. 6, pp. 695–702, 1997.

[56] A. D. Seagar, “Probing With Low Frequency Electric Currents,” *Electr. Eng.*, vol. PhD, 1983.

[57] J. Hadamard, “Sur les problèmes aux dérivées partielles et leur signification physique.,” *Princet. Univ. Bull.*, 1902.

[58] J. M. Khor, A. Tizzard, A. Demosthenous, and R. Bayford, “Wearable sensors for patient-specific boundary shape estimation to improve the forward model for electrical impedance tomography (EIT) of neonatal lung function,” *Physiol. Meas.*, vol. 35, no. 6, pp. 1149–1161, 2014.

[59] D. C. Barber, B. H. Brown, and N. J. Avis, “Image Reconstruction in Electrical Impedance Tomography Using Filtered Back - Projection,” *Proc. Annu. Int. Conf. IEEE Eng. Med. Biol. Soc.*, pp. 1691–1692, 1992.

[60] T. J. Yorkey, J. G. Webster, and W. J. Tompkins, “Comparing Reconstruction Algorithms for Electrical Impedance Tomography,” *IEEE Trans. Biomed. Eng.*, vol. BME-34, no. 11, pp. 843–852, 1987.

[61] A. Adler *et al.*, “GREIT: A unified approach to 2D linear EIT reconstruction of lung images,” *Physiol. Meas.*, vol. 30, no. 6, 2009.

[62] M. Proença *et al.*, “Understanding the Genesis of Cardiac Signals in Electrical Impedance Tomography,” *Proc. Int. Conf. Bio-inspired Syst. Signal Process.*, pp. 27–34, 2014.

[63] E. D. Trutman and R. S. Newbower, “A Practical Analysis of the Electrical Conductivity of Blood,” *IEEE Trans. Biomed. Eng.*, vol. BME-30, no. 3, pp. 141–154, 1983.

[64] A. E. Hoetink, T. J. C. Faes, K. R. Visser, and R. M. Heethaar, “On the flow dependency of the electrical conductivity of blood,” *IEEE Trans. Biomed. Eng.*, vol. 51, no. 7, pp. 1251–1261, 2004.

[65] F. M. L. and J. P. and S. Bagno, “The Electrical Conductance Properties of Blood in Motion,” *Phys. Med. Biol.*, vol. 7, no. 2, p. 177, 1962.

[66] F. Thürk, A. D. Waldmann, K. H. Wodack, C. J. Trepte, and D. Reuter, “Evaluation of reconstruction parameters of electrical impedance tomography on aorta detection during saline bolus injection,” vol. 2, no. 1, pp. 511–514, 2016.

[67] S. Maisch *et al.*, “Heart-lung interactions measured by electrical impedance tomography.,” *Crit. Care Med.*, 2011.

[68] T. Dai *et al.*, “My IOPscience GREIT : a unified approach to 2D linear EIT reconstruction of lung images.”

[69] F. Braun, M. Proenca, J. Sola, J.-P. Thiran, and A. Adler, “A Versatile Noise Performance Metric for Electrical Impedance Tomography Algorithms,” *IEEE Trans. Biomed. Eng.*, vol. 64, no. 10, pp. 1–1, 2017.

[70] Wodack, Karin H *et al.*, “Detection of thoracic vascular structures by electrical impedance

tomography : a systematic assessment of prominence peak analysis of impedance changes Detection of thoracic vascular structures by electrical impedance tomography : a systematic assessment."

[71] P. A. Yushkevich *et al.*, "User-guided 3D active contour segmentation of anatomical structures: Significantly improved efficiency and reliability," *Neuroimage*, vol. 31, no. 3, pp. 1116–1128, 2006.

[72] J. Schöberl, "An advancing front 2D/3D-mesh generator based on abstract rules," *Comput. Vis. Sci.*, vol. 1, no. 1, pp. 41–52, 1997.

[73] B. Grychtol, W. R. B. Lionheart, M. Bodenstein, G. K. Wolf, and A. Adler, "Impact of Model Shape Mismatch on Reconstruction Quality in Electrical Impedance Tomography," vol. 31, no. 9, pp. 1754–1760, 2012.

[74] A. Adler and R. Guardo, "Electrical impedance tomography: Regularized imaging and contrast detection," *IEEE Trans. Med. Imaging*, vol. 15, no. 2, pp. 170–179, 1996.

[75] C. H. Antink, R. Pikkemaat, J. Malmivuo, and S. Leonhardt, "A shape-based quality evaluation and reconstruction method for electrical impedance tomography," *Physiol. Meas.*, vol. 36, no. 6, pp. 1161–1177, 2015.

[76] F. Braun, M. Proenca, J. Sola, J. P. Thiran, and A. Adler, "A Versatile Noise Performance Metric for Electrical Impedance Tomography Algorithms," *IEEE Trans. Biomed. Eng.*, vol. 64, no. 10, pp. 2321–2330, 2017.

[77] M. Koreny, E. Riedmüller, M. Nikfardjam, P. Siostrzonek, and M. Müllner, "Arterial Puncture Closing Devices Compared with Standard Manual Compression after Cardiac Catheterization: Systematic Review and Meta-analysis," *J. Am. Med. Assoc.*, vol. 291, no. 3, pp. 350–357, 2004.

[78] A. S. Paola Vecchia, Rüdiger Matthes, Gunde Ziegelberger, James Lin, Richard Saunders, "Exposure to high frequency electromagnetic fields, biological effects and health consequences (100kHz-300GHz)," 2009.

[79] A. Adler, P. O. Gaggero, and Y. Maimaitijiang, "Adjacent stimulation and measurement patterns considered harmful," *Physiol. Meas.*, vol. 32, no. 7, pp. 731–744, 2011.

[80] O. Innovation, "EIT Pioneer Set," no. June, 2017.

[81] F. Thuerk *et al.*, "HYPERTONIC SALINE INJECTION TO DETECT AORTA IN PORCINE EIT," vol. 4, p. 2011, 2011.

[82] S. Laurent *et al.*, "Expert consensus document on arterial stiffness: Methodological issues and

clinical applications," *Eur. Heart J.*, vol. 27, no. 21, pp. 2588–2605, 2006.

[83] W. SINGER, T. L. OPFER-GEHRKING, B. R. MCPHEE, M. J. HILZ, and P. A. LOW, "Influence of posture on the Valsalva manoeuvre," *Clin. Sci.*, vol. 100, no. 4, pp. 433–440, 2001.

[84] F. Bellemare, A. Jeanneret, and J. Couture, "Sex Differences in Thoracic Dimensions Franc," vol. 168, pp. 305–312, 2003.

[85] B. E. Hurwitz, L.-Y. Shyu, S. P. Reddy, N. Schneiderman, and J. H. Nagel, "Coherent Ensamble Averaging Techniques for Impedance Cardiography," pp. 228–235, 1990.

[86] Y. C. Chiu, P. Arand, Sanjeev G. Shroff, and John D Carroll, "Determination of pulse wave velocities with computerized algorithms," *Am. Heart J.*, 1991.

[87] T. Igari, "The length of the aorta from the subclavian artery to the renal artery based on computed tomographic measurements in Japanese adults," *J. Artif. Organs*, vol. 9, no. 4, pp. 267–270, 2006.

[88] B. Grychtol and A. Adler, "Choice of reconstructed tissue properties affects interpretation of lung EIT images," *Physiol. Meas.*, vol. 35, no. 6, pp. 1035–1050, 2014.

[89] T. I. Oh, T. E. Kim, S. Yoon, and K. J. Kim, "Flexible electrode belt for EIT using nanofiber web dry electrodes."

[90] R. J. Doonan, A. Hausvater, C. Scallan, D. P. Mikhailidis, L. Pilote, and S. S. Daskalopoulou, "The effect of smoking on arterial stiffness," *Hypertens. Res.*, vol. 33, no. 5, pp. 398–410, 2010.

[91] A. Adler, I. Frerichs, and B. Grychtol, "The off-plane sensitivity of EIT," vol. 0, p. 2006, 2006.

[92] W. R. B. Lionheart, "EIT reconstruction algorithms: Pitfalls, challenges and recent developments," *Physiol. Meas.*, vol. 25, no. 1, pp. 125–142, 2004.

[93] J. Wagenaar and J. Wagenaar, "Electrical Impedance Tomography in 3D : characterization and evaluation by Master of Applied Science," 2015.

[94] S. Ahn, H. Wi, T. I. Oh, A. L. McEwan, S. C. Jun, and E. J. Woo, "Continuous nondestructive monitoring method using the reconstructed three-dimensional conductivity images via GREIT for tissue engineering," *J. Appl. Math.*, vol. 2014, 2014.

[95] B. Grychtol *et al.*, "Focusing EIT reconstructions using two electrode planes," vol. 32, p. 2017, 2017.

[96] S. D. Pawar, P. Murugavel, and D. M. Lal, “Effect of relative humidity and sea level pressure on electrical conductivity of air over Indian Ocean,” *J. Geophys. Res. Atmos.*, vol. 114, no. 2, pp. 1–8, 2009.

[97] J. Wagenaar *et al.*, “3D EIT image reconstruction with GREIT.”

[98] J. Wagenaar and A. Adler, “Electrical Impedance Tomography in 3D using two electrode planes : characterization and evaluation.”

[99] A. Adler *et al.*, “Adjacent stimulation and measurement patterns considered harmful.”

[100] A. D. Waldmann, “Master of Science Thesis Automated Tests for Electrical Impedance Tomography by,” *Master Thesis*, no. November, 2012.

[101] B. Flow, *Blood Flow in Arteries*. .

[102] http://humananatomylesson.com/circulatory-system-blood-flow-diagram/circulatory-system-blood-flow-diagram-how-does-blood-flow-through-the-hear opened on 15.12.2017

[103] https://upload.wikimedia.org/wikipedia/commons/thumb/9/9a/Wiggers_Diagram.png/480px-Wiggers_Diagram.png opened on 15.01.2018

[104] http://eidors3d.sourceforge.net/tutorial/netgen/extrusion/thoraxmdl.shtml opened on 16.12.2017

[105] http://antranik.org/the-respiratory-system/ opened on 17.12.2017

[106] https://humananatomyly.com/anatomy-diaphragm-muscle/anatomy-diaphragm-muscle-diaphragm-muscle-anatomy-anatomy-organ/ opened on 17.12.2017

[107] http://humananatomychart.us/category/human-body/page/40/ opened on 21.01.2018

[108] http://niremf.ifac.cnr.it/tissprop/ opened on 25.08.2017

[109]http://www.matweb.com/search/DataSheet.aspx?MatGUID=025d4a04c2c640c9b0eaaef28318d761&ckck=1 opened on 24.03.2018

Hiermit erkläre ich, dass die vorliegende Arbeit gemäß dem Code of Conduct – Regeln zur Sicherung guter wissenschaftlicher Praxis (in der aktuellen Fassung des jeweiligen Mitteilungsblattes der TU Wien), insbesondere ohne unzulässige Hilfe Dritter und ohne Benutzung anderer als der angegebenen Hilfsmittel, angefertigt wurde. Die aus anderen Quellen direkt oder indirekt übernommenen Daten und Konzepte sind unter Angabe der Quelle gekennzeichnet. Die Arbeit wurde bisher weder im In– noch im Ausland in gleicher oder in ähnlicher Form in anderen Prüfungsverfahren vorgelegt.

Wien, 16.04.2018

_____, Martin Elenkov